

Appendix C

Wellbore and Groundwater Temperature Distribution in Eastern Snake River Plain; Implications for Groundwater Flow and Geothermal Potential, Idaho

1 Wellbore and Groundwater Temperature Distribution in Eastern Snake River Plain;
2 Implications for Groundwater Flow and Geothermal Potential, Idaho.

3 Travis L. McLing,^{1,2,*} Richard P. Smith,³ Robert W. Smith,⁴ David D. Blackwell,⁵ Robert C.
4 Roback,⁶ and Andrus J. Sondrup¹
5

6 ¹Idaho National Laboratory, P.O. Box 1625, Idaho Falls, ID, 83415-2107, U.S.A

7 ²The Center for Advanced Energy Studies, 995 University Blvd, Idaho Falls, ID, 83401, U.S.A.

8 ³Smith Geologic and Photographic Services, LLC, Nathrop, CO, 81236, U.S.A

9 ⁴University of Idaho, Moscow, ID, 83844, U.S.A

10 ⁵Department of Geological Sciences, Southern Methodist University, Dallas, TX, 75275-0395,
11 U.S.A

12 ⁶Earth and Environmental Sciences Division, Los Alamos National Laboratory, Los Alamos,
13 NM, 87545, U.S.A

14 *Corresponding author: Travis L. McLing travis.mcling@inl.gov; 012085267269;
15 fax 012085260875

16 **ABSTRACT**

17 The Eastern Snake River Plain (ESRP) aquifer, beneath the ESRP in Idaho, United States of
18 America, is one of the most productive, and heavily-used aquifers in the United States. The
19 Idaho National Laboratory (INL) Site is located on the ESRP. Past waste disposal operations at
20 the INL Site have led to localized contamination of the ESRP aquifer, and the current waste
21 inventory in the vadose zone above the aquifer at the INL Site poses a potential future threat to
22 the aquifer. Additionally, due to past volcanic activity, the ESRP has been the exploration target
23 for geothermal development, but the presence of the vast cold-water aquifer largely prevents
24 direct characterization of this potential. For these reasons, a thorough characterization of the
25 ESRP aquifer is necessary. Previous studies have relied on hydraulic and geochemical data, and
26 focused primarily on the uppermost productive part of the aquifer. This study presents, for the
27 first time, groundwater temperature data from more than 200 shallow wells and nine deep wells
28 in and around the ESRP, which were evaluated to trace aquifer flow patterns in the uppermost
29 part of the aquifer and elucidate the vertical structure of the upper and lower aquifer,
30 respectively. These data provide firm constraints that the ESRP contains two aquifers, an upper
31 productive aquifer and a deep, tight thermal aquifer. This study defines the thickness of the upper
32 productive aquifer and the nature of the boundary between the two-aquifer systems. The data
33 also demonstrate that aquifer temperature distribution, combined with other data sources, is a
34 useful tool to confirm, or reveal, characteristics of an aquifer that cannot be defined by other
35 methods.

36 At the water table in the ESRP aquifer beneath the ESRP, groundwater temperatures range from
37 $<6^{\circ}\text{C}$ to $>18^{\circ}\text{C}$ even though ground-surface temperatures do not vary significantly. The coldest
38 areas of the aquifer correspond to zones of recharge, primarily from snowmelt in drainages
39 around the plain and from the Yellowstone Plateau. Zones of high recharge occur where the
40 South Fork of the Snake River enters the plain near Rexburg, Idaho, and along the northern
41 margin of the plain from the Medicine Lodge Basin (Centennial Range). Anomalously, warm
42 zones in the aquifer probably correspond to areas of slow groundwater movement and/or areas
43 where geothermal input from depth is pronounced and overwhelms the cold water system. Warm
44 zones occur in the western, north central, and southeastern areas of the INL Site and in an area
45 just north of Juniper Buttes near the northeastern margin of the plain. In all four areas,
46 temperatures at the water table reach $\geq 18^{\circ}\text{C}$.

47 Vertical temperature profiles from more than 200 shallow wells and nine deep wells in and
48 around the ESRP show that the warm zones in the ESRP aquifer are the tops of heated
49 groundwater plumes that are related to less-permeable, slower-flowing regions of the aquifer and
50 are the result of increased conductive heating or possibly direct geothermal input into the aquifer.
51 The heated groundwater plumes are not a result of the infiltrated or warmer irrigation water. In
52 addition, temperature profiles in the nine deep wells show inflection points from a nearly
53 isothermal regime where groundwater flow controls temperature to steep regional conductive
54 gradients where there is little lateral movement of groundwater. Examination of drill cores
55 reveals that these temperature inflection points correspond to the inception of hydrothermal
56 alteration and mineralization of basalts, which seals permeability and forms the base of the upper
57 productive (transmissive) aquifer.

58 Based on temperature inflection points, ESRP aquifer thickness in the area of the INL Site ranges
59 from <100 m to approximately 400 m, increasing in thickness to >800 m in a deep exploratory

60 well approximately 42 km southwest of the INL Site. Deep “channels” of cold groundwater
61 characterize the thickest portions of the aquifer with very sharp inflection in well temperature
62 profiles where the regional thermal conductive gradients mark the base of the upper productive
63 aquifer. Two of the warmest zones correspond to areas where the aquifer is very thin and
64 geothermal water is closer to the surface.

65 **Keywords:** Eastern Snake River Plain, thermal groundwater tracer, groundwater flow,
66 temperature distribution.

67 1. INTRODUCTION

68 Beneath the Eastern Snake River (ESRP) in Idaho, United States of America, is the
69 highly-productive and aerially-extensive ESRP aquifer ($27,900 \text{ km}^2$; Figure 1; Whitehead 1986).
70 Because of its association with tectonic and thermal features of the Yellowstone hot spot track,
71 the ESRP and its margins are recognized as the location for potential (and actual) geothermal
72 resources. It was highlighted as one of six high-grade enhanced geothermal system regions
73 within the United States (U.S.), with 75% of the $37,500\text{-km}^2$ area demonstrating temperatures
74 $>200^\circ\text{C}$ at a depth of 4 km (MIT 2006). In 1991, the ESRP aquifer was designated as a Sole
75 Source Aquifer under Section 1424 of the Safe Drinking Water Act (EPA 1999). The Sole
76 Source designation recognizes that the aquifer serves as the principal source for drinking water
77 for the region and that there is no reasonably available alternative source should the aquifer
78 become contaminated. For the most part, the aquifer contains pristine, uncontaminated
79 groundwater. However, past waste disposal practices of the U.S. Department of Energy at the
80 Idaho National Laboratory (INL) Site have locally contaminated the aquifer with low levels of
81 organic solvents and radionuclides (DeSimone et al. 2014). Contamination also exists in the
82 vadose zone above the aquifer at the INL Site, and these shallow sources pose a potential
83 continuing threat to groundwater quality. In addition, poor agriculture and sewage disposal
84 practices have resulted in elevated nitrate concentration in some areas of the aquifer
85 (Neeley 2005).

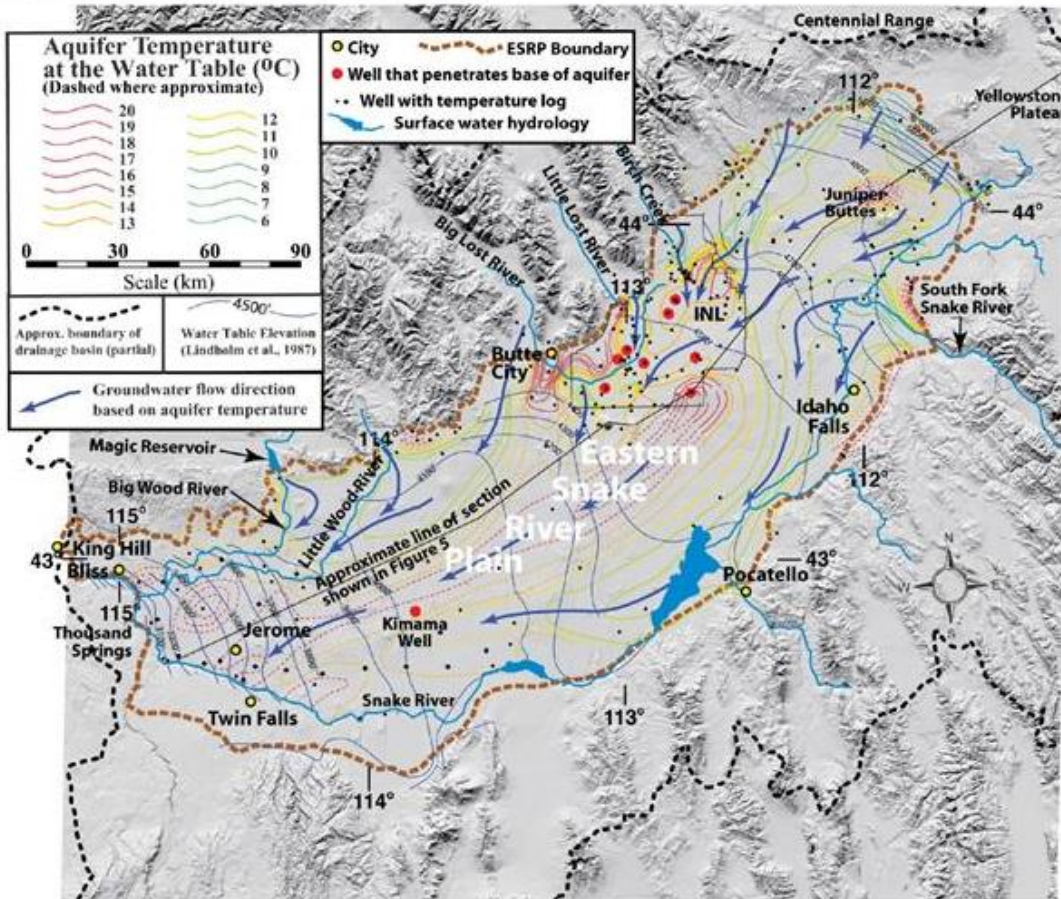
86 Effectively managing and protecting the regionally-important ESRP groundwater resource
87 requires a detailed understanding of the nature and characteristics of the shallow sole source
88 aquifer and the much deeper heat sources. This study uses observed horizontal and vertical
89 groundwater temperature observations to infer the thickness of the aquifer. This approach is
90 integrated with previously-published isotopic studies (Johnson et al. 2000; Lou et al. 2000;
91 Roback et al. 2001) to infer large-scale aquifer flow features and assess the relationship of the
92 aquifer to deep heat sources.

93 2. BACKGROUND

94 2.1. Hydrogeology

95 The ESRP is an arcuate structural depression 50 to 100 km wide by 300 km long and
96 encompasses approximately $27,900 \text{ km}^2$ of southeastern Idaho. The plain rises from
97 approximately 1,000 m above mean sea level in the west to $>1,500 \text{ m}$ in the east. It is bounded
98 on the north and south by mountains rising $>2,500 \text{ m}$ above the plain. The mountain ranges are
99 composed of deformed Paleozoic and Mesozoic sedimentary rocks and silicic volcanics. The
100 sedimentary rocks have been uplifted relative to the plain by northwesterly trending faults

101 associated with the Basin and Range Province (Kuntz et al. 1992), through which the plain cuts a
102 northeast-trending swath (Pierce and Morgan 2009).



103
104 Figure 1. Map of study area showing topography, major geographic features, water table
105 elevation contours (Lindholm et al. 1987), and partial boundary of drainage basin for the Eastern
106 Snake River Plain aquifer (the drainage basin extends farther east, into the Yellowstone area and
107 farther south into Utah). Control for the contours of aquifer temperature comes from temperature
108 logs of many wells (black dots). Temperatures of wells in and near the Idaho National
109 Laboratory Site were acquired during logging campaigns from 1990 through 2001. Temperatures
110 of wells outside the Idaho National Laboratory Site were reported by Bartholomay et al. (1997)
111 and Brott et al. (1981). Flow directions (green arrows) were interpreted from both water table
112 elevations and zones of continuous warm or cool groundwater in the aquifer. Idaho National
113 Laboratory Site is indicated by "INL."

114 Quaternary basaltic eruptive centers and associated flows cover >95% of the topography of the
115 ESRP. Locally, a thin layer of fluvial sediments and loess covers these basalt flows, primarily
116 along the Snake River and where drainages feed onto the plain. Individual basalt flows of
117 relatively small volume were extruded primarily from northwest-trending fracture systems or
118 numerous small monogenetic shield volcanoes (Pierce and Morgan 1992). At depth, the basalts

119 are inter-layered with a variety of sediment, including carbonate, fluvial sands and gravels,
120 carbonate-rich eolian silt, lacustrine deposits, and minor reworked silicic tuffs (Bartholomay et
121 al. 1997). Below approximately 1 km in depth, welded rhyolite tuff and tuffaceous sediments
122 dominate the plain (Pierce and Morgan 1992). Recent (~2KA) volcanic activity on the ESRP has
123 resulted in a very-high geothermal gradient (Blackwell 1989) as manifested by numerous thermal
124 springs around the periphery of the plain.

125 The first significant study of the ESRP aquifer system was conducted in the 1930s (Stearns 1936;
126 Stearns et al. 1938). The aquifer is recharged by underflow and runoff from high mountains that
127 surround the plain. The most prominent sources of recharge water to the aquifer are the
128 Yellowstone Plateau at the northeast margin of the ESRP, Centennial Range north of the plain,
129 and Basin and Range mountain ranges northwest and southeast of the plain (Figure 1).
130 Infiltration of irrigation water, derived primarily from surface water sources, is also a locally
131 important source of aquifer recharge water primarily along the eastern margin of the plain.
132 Regional groundwater flow is generally southwestward in the aquifer, down the length of the
133 plain from the Yellowstone Plateau to its discharge along the Snake River west of Twin Falls,
134 Idaho (Figure 1). Because of low temperatures (<20°C), the short residence times of groundwater
135 in the host rock (generally estimated to be less than a few hundred years), and the relative
136 insolubility of the host rock, the cool upper productive aquifer is relatively inert geochemically.
137 Thus, the geochemical and isotopic signature of the recharge terrains is preserved in the
138 groundwater tens of kilometers into the aquifer (Roback et al. 2001). Groundwater moves
139 through the host rocks of the plain in interflow rubble zones between lava flows, fractures within
140 basalt flows, and coarse-grained clastic interbeds at flow rates of up to 1 km/yr⁻¹ in places
141 (Fisher and Tinning 2011). Groundwater flow in the aquifer is impeded by thick, relatively
142 unfractured interior zones of lava flows; zones of fine-grained clastic interbeds; and perhaps
143 vertical, northwest-trending basalt feeder dikes in volcanic rift zones (see for example, Kuntz et
144 al. 2002). These geologically heterogeneities lead to differences in saturated hydraulic
145 conductivity of several orders of magnitude (Welhan and Reed 1997), which render delineation
146 of groundwater flow patterns difficult. Although it has been long recognized that the aquifer is
147 highly heterogeneous, past investigators have used the assumption of an equivalent porous
148 medium in their modeling efforts (Robertson et al. 1974; Lewis and Goldstein 1982; Goode and
149 Konikow 1990).

150 This assumption is based on the reasoning that a sufficiently large volume of the ESRP aquifer
151 will exhibit the same behavior as a smaller volume of a porous medium aquifer (Robertson et al.
152 1974; Robertson 1976; Garabedian 1986). However, previous investigations of groundwater
153 chemistry and isotope content (Johnson et al. 2000; Lou et al. 2000; Roback et al. 2001; McLing
154 et al. 2002) suggest that equivalent porous medium treatment does not adequately describe the
155 flow complexities arising from the large-scale heterogeneities in transmissivity or the observed
156 interaction of cold water recharge with high crustal heat.

157 The objective of this study is to demonstrate that horizontal and vertical temperature distribution,
158 combined with other data sources, are useful tools for revealing the groundwater flow pattern
159 and determining the depth to which convective groundwater flow controls temperature.

160 2.2. Groundwater Temperature

161 Early conceptual models used to model groundwater flow in the ESRP aquifer assumed uniform
162 aquifer thickness (see for example, Robertson 1976 and Garabedian 1986). This assumption was

163 supported by data from groundwater production wells that were drilled no deeper than the depth
164 necessary to produce adequate water flow (up to hundreds of m³/s). However, because of the
165 importance of understanding the geothermal potential and delineating the extent of aquifer
166 contamination associated with the U.S. Department of Energy's activities, temperature data from
167 the nine deep wells (eight drilled on the INL Site and one off the INL Site) provide valuable
168 insight into the three-dimensional character of the aquifer.

169 Water recharging the ESRP aquifer from the Yellowstone Plateau and mountain valleys
170 surrounding the ESRP is mostly snowmelt from high elevation and therefore cold (6 to 9°C). As
171 groundwater flows to the southwest, the water table generally deepens and flowing aquifer water
172 intercepts the crustal heat flow of approximately 110 mW m⁻² (among the highest in North
173 America; Blackwell and Steele 1992) from below. The aquifer water gradually warms until its
174 temperature is approximately 11 to 12°C at the location of the INL Site and approximately 16°C
175 at its discharge in the Thousand Springs area (Figure 1). The southwestward warming of
176 groundwater (Blackwell 1989) is complicated by flow of cold recharge water toward the plain
177 from the high mountains along its northwest margin and from the infiltration of diverted Snake
178 River irrigation water along its southeastern margin (Figure 1). As a result, local thermal profiles
179 vary drastically, and are strongly influenced by permeability distribution. In addition, there are
180 zones of deeper, warmer groundwater recharge from the high-temperature areas (>16°C) on the
181 margins of the plain (for example, the Butte City, Idaho, area [Figure 1]), especially in places
182 where major side streams carrying cold groundwater are absent. The interplay of crustal heat and
183 cold flowing groundwater make aquifer temperature analysis a particularly applicable
184 methodology for investigating aquifer geometry and flow dynamics (Brott et al. 1981).

185 **2.3. Well Temperature Profiles**

186 The contribution of deep thermal groundwater to the upper productive aquifer was first
187 hypothesized nearly 40 years ago, based on geological arguments (Robertson et al. 1974). Mann
188 (1986) inferred from well INEL-1 that up to 19 million cubic meters of thermal groundwater
189 might be upwelling into the effective aquifer beneath the INL Site. Wood and Low (1986)
190 determined that, based on ¹⁴C and δ²H, groundwater in the deep thermal system may be more
191 than 17,000 years old and may have been recharged during a colder climatic time. McLing et al.
192 (2002) identified a distinct chemical signature for groundwater that has its source in the well-
193 equilibrated deep geothermal system, suggesting that deep Na-K-HCO₃ groundwaters are
194 distinct from the groundwater of the upper aquifer system. The chemical influence of this deep
195 upwelling groundwater is well preserved in the chemical signature of the upper aquifer. McLing
196 et al. (2002) also postulated based on the limited data that the deep Na-K-HCO₃ groundwaters
197 are widespread across the ESRP indicating that a regional geothermal system is present, albeit
198 suppressed by the upper productive aquifer.

199 Since the early 1960s, more than 200 shallow wells in and around the ESRP have had vertical
200 temperature profiles logged. U.S. Geological Survey (USGS) personnel working at what was
201 then the National Reactor Testing Station (now INL) performed the earliest temperature logging
202 (Olmsted 1962). Since the 1970s, several temperature-logging studies have been conducted in
203 the plain (Brott et al. 1981; Ziagos and Blackwell 1986; Blackwell 1989; Blackwell 1990;
204 Blackwell et al. 1992; Williams and DeAngelo 2008). The goals of these studies were to
205 (1) determine crustal heat flow beneath the ESRP aquifer, (2) determine the nature of the
206 transition from the upper productive aquifer to the convection-dominated deep geothermal

207 system, (3) determine the temperature distribution in the aquifer water itself (Blackwell and
208 Steele 1992), and (4) evaluate the geothermal potential beneath the aquifer. However, because
209 most of the logged wells were drilled to monitor water levels and collect water samples, they
210 generally extend only a few meters below the water table and provide only limited information
211 on sub-aquifer geothermal characteristics. In addition to the monitoring wells, a number of deep
212 wells were drilled that penetrate the base of the aquifer. Nine of these deep wells have high-
213 quality temperature logs and are used in this study to provide information on position of the
214 upper productive aquifer's base and three-dimensional distribution of temperature throughout the
215 aquifer. The nine deep wells are identified as INEL-1, Site 14, CH2-2A, CH-1, C1A, WO-2,
216 ANL-1, M-ETR, and Kimama.

217 Prior to the availability of drill core, water chemistry, and temperature data from deep boreholes
218 on the ESRP, there was not an accurate method for determining the position of the effective base
219 of the upper productive aquifer. Because little was known regarding the deep subsurface, an
220 early approach was to assume that Tertiary lava flows and sediments that lie beneath the
221 Quaternary lava flows and sediments of the plain were so old that they were altered and
222 relatively impermeable, thus defining the base for the aquifer (Robertson et al. 1974; Robertson
223 1976; Garabedian 1986). Whitehead (1986) used electrical resistivity surveys to define the
224 thickness of the Quaternary section, and thus the thickness of the aquifer. Anderson and Bowers
225 (1995) and Anderson et al. (1997) argued that the effective base of the aquifer coincides with the
226 top of "a thick widespread layer of clay, silt, sand, and altered basalt that is older than about
227 1.8 million years and equivalent in age to the Glenns Ferry Formation." Drilling of well INEL-1,
228 through the base of the productive aquifer showed that, at least locally, the position of the aquifer
229 base is related the inception of secondary mineralization, which seals conductive structure in the
230 aquifer host rock (Mann 1986). Mann (1986) noted that in well INEL-1, where the water table is
231 approximately 120 m below land surface, temperature, groundwater chemistry, and permeability
232 changed dramatically in the borehole approximately 250 m below land surface. Aquifer
233 properties (i.e., temperature, chemistry, and permeability) above the 250-m transition were
234 consistent with the regional aquifer system; however, below 250 m, temperatures were higher,
235 groundwater chemistry was more sodium and potassium rich, and matrix permeability was
236 dramatically reduced and head increased (Mann 1986). The implication of well INEL-1
237 observations regarding change in aquifer properties with depth was not realized until Morse and
238 McCurry (2002) and McLing et al. (2002) conducted studies. Using available core and water
239 samples, these studies suggested that the characteristics of the entire ESRP aquifer system are the
240 same as observed in well INEL-1. Based on changes in groundwater chemistry with depth,
241 McLing et al. (2002) concluded the aquifer was actually composed of two systems, a shallow,
242 cold, highly-transmissive aquifer with fast-moving groundwater and a deep, warm, more
243 stagnant aquifer system. This conclusion is supported by the measured 35,000-year age for deep
244 groundwater from well INEL-1 (Mann 1986). Morse and McCurry (2002) observed in the drill
245 core collected from deep boreholes that the inception of hydrothermal alteration and secondary
246 mineralization of basalts coincides with the transition from Ca-Mg-HCO₃ to N-K-HCO₃ type
247 groundwater reported by McLing et al. (2002). The occurrence of mineral alteration results in
248 decreased permeability allowing the conductive thermal gradient to control temperature in the
249 deeper aquifer system.

250 **3. METHODS**

251 Geothermal heat and borehole temperature logs have a long history of use for defining aquifer
252 flow direction and quantifying aquifer hydraulic parameters (Bredehoeft and Papadopoulos 1965;
253 Ge 1998; Burns et al. 2011; Saar 2011; Burns et al. 2015). In most of these applications, the
254 aquifers that were studied have a large variability in horizontal and vertical permeability or are
255 regionally confined. Burns et al. (2011) had some success using aquifer temperature to model
256 regional aquifer behavior in the confined Columbia Plateau aquifer. Saar (2011) showed that
257 using geothermal heat in an aquifer combined with multiple diverse data sets makes a powerful
258 tool to elucidate large-scale groundwater flow. Also, well temperature profiles have been used in
259 computational models to identify fracture flow zones within an aquifer system (Shemin 1997;
260 Ge 1998; Ingebritsen 1992). Heat flow in the ESRP averages 110 mW m^{-2} (Blackwell 1989) but
261 is not uniformly distributed. Heat flow is highest along the margins of the plain (80 to
262 $100 \text{ mW/m}^2\text{-s}$) and lowest along the central plain (approximately $30 \text{ mW/m}^2\text{-s}$). The low heat
263 flow values in this region are largely based on shallow wells, which are strongly influenced by
264 the presence of a huge fast-flowing aquifer system in the ESRP. When heat flow is measured in
265 deep wells that penetrate below the base of the aquifer, the values are more consistent with the
266 regional heat flow of $110 \text{ mW/m}^2\text{-s}$ (Blackwell 1989). However, even for the deepest boreholes
267 drilled into the plain, there is significant variability in heat flow depending on location. For
268 example, heat flow measured in well INEL-1 is up to 110 mW m^{-2} while heat flow in well CH-1,
269 15 km to the southeast, is 65 mW m^{-2} .

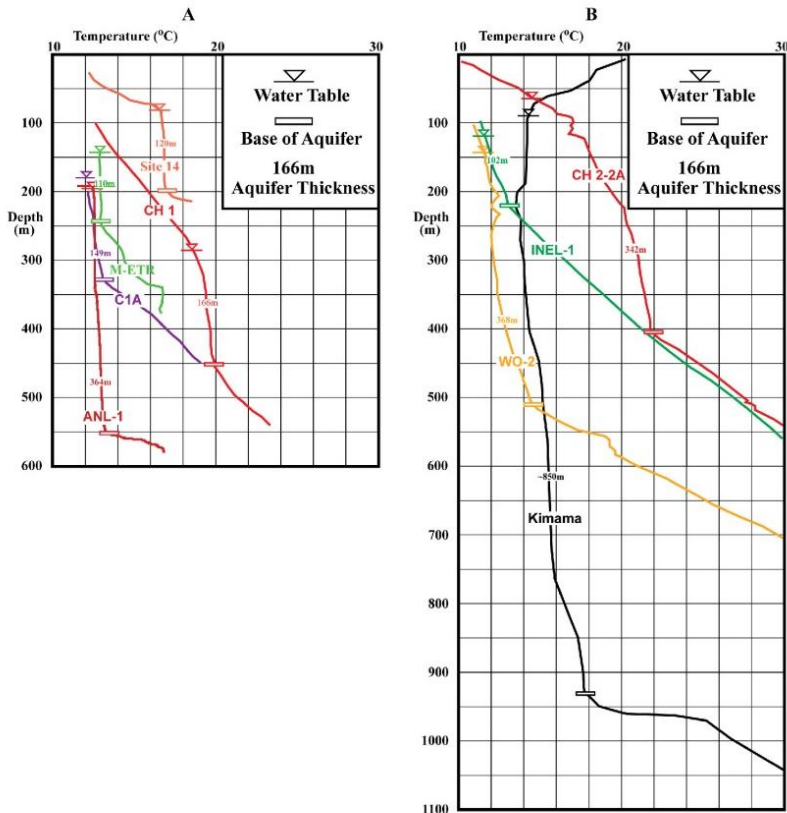
270 Although thousands of wells have been drilled into the ESRP aquifer for contaminant
271 monitoring, domestic water supply, and agriculture production, these wells provide very little
272 information regarding the vertical character of the aquifer. Fortunately, over the past 40 years,
273 there have been a number of deep wells drilled that penetrate through the upper productive
274 aquifer. Nine of these deep wells that have had multiple high-quality temperature profiles
275 collected are used in this study. The most recent well drilled was the Kimama well. The Kimama
276 well was drilled in 2010 as part of Project Hotspot, which drilled a series of deep boreholes in
277 southern Idaho (Shervais et al. 2013). The 1,912-m-deep Kimama well was drilled 42 km
278 southwest of the INL Site (Figure 1). Although the Kimama well was decommissioned due to
279 Idaho State permitting requirements not long after drilling, the data collected from the well
280 (Twining and Bartholomay 2011; Shervais et al. 2013) have proven invaluable. Data from the
281 Kimama well allow for extending the three-dimensional aquifer model well outside of the INL
282 Site. Together, the nine deep wells used in this study represent rare and extremely valuable
283 windows into the vertical character of the aquifer. Unfortunately, the three deepest wells
284 (INEL-1, Kimama, and WO-2) are no longer available for study. For these three deepest wells,
285 this study relies on existing data that were collected by the USGS in the past, in some cases
286 (wells INEL-1 and WO-2), more than 30 years ago (Mann 1986; Blackwell 1990).

287 This study summarizes borehole temperature data from more than 200 shallow monitoring wells
288 and nine deep wells of sufficient depth to penetrate to the conductive heat flow regime beneath
289 the ESRP aquifer. The USGS collected and recorded data from many of the deepest INL wells.
290 Thermal data from several of these wells have been collected for several decades and show that
291 aquifer temperatures and borehole temperature profiles have remained remarkably stable over
292 time. It has been recognized that available hydraulic head data may lack the resolution to fully
293 characterize groundwater flow in regional aquifers such as the ESRP (Blackwell and Priest 1996;
294 Anderson 2005). Therefore, it is important that other studies and sources of data be used to refine

295 conclusions drawn from the water-table elevation measurements alone. Synthesis of multiple
296 sources of data such as temperature, chemistry, hydraulic head, and environmental isotopes can
297 offer a better understanding of flow characteristics than any single data source considered in
298 isolation.

299 **4. TEMPERATURE PROFILES IN DEEP WELLS IMPLICATIONS FOR AQUIFER**
300 **GEOMETRY**

301 The ESRP aquifer geologic characteristics provide a unique opportunity to use temperature logs
302 in numerous wells distributed over 27,900 km² to define the dynamics of aquifer flow in an
303 exceptionally large, free-flowing, aquifer in fractured rock. It is also an ideal system to test the
304 validity of using groundwater temperature combined with chemical data to characterize
305 large-scale aquifer conditions. Temperature profiles from the nine deep wells shown in Figure 2
306 show a break in slope from an isothermal gradient in the upper reaches of the boreholes to a
307 deeper, steep conductive gradient in the deeper reaches of the boreholes. This break in slope
308 marks the base of the upper productive aquifer and the transition to the deep, tight geothermal
309 aquifer at depth. Drill core data collected from some of the deep wells show that this break in
310 slope also corresponds to the inception of hydrothermal alteration and secondary mineralization
311 of basalts beneath the upper aquifer (Morse and McCurry 2002). The occurrence of mineral
312 alteration is important because it results in the sealing of conductive structure within the aquifer,
313 and allows conductive heat flow to dominate.



314

315 Figure 2. Temperature profiles for nine deep wells at Idaho National Laboratory Site and in the
316 Eastern Snake River Plain.

317 Temperature profiles for individual wells completed in the ESRP aquifer illustrate the regional
318 and local three-dimensional character of the aquifer temperature. In general, temperature profiles
319 for aquifer wells show a constant temperature gradient in the vadose zone from the land surface
320 to the water table. That gradient usually increases with depth in places where the aquifer
321 temperature is $>16^{\circ}\text{C}$ but can be negative over areas where there is vigorous cold-water recharge
322 (Brott et al. 1981). Below the water table, the profiles are either isothermal or show minimal
323 temperature change with depth (Figure 2). This lack of vertical variation in temperature is
324 interpreted to be the result of fast-flowing groundwater in the highly-transmissive upper aquifer
325 (Anderson 2005). As shown in Figure 2, the bottom of the isothermal section is usually abrupt,
326 and below that depth the gradient increases to reflect the conductive transfer of heat from the
327 deep crust and upper mantle. The nearly constant measured heat flow over large areas of the
328 ESRP (on a kilometric scale) supports the idea of conductive heat flow from great depth
329 (Blackwell and Steele 1992; Blackwell et al. 1992). The abrupt transition from “isothermal” to
330 conductive gradient (temperature inflection point) corresponds to the upper limit of alteration
331 and mineralization of basalts, as evidenced in drill cores for several wells (Morse and McCurry
332 2002). The abrupt transition is also coincident with the change in groundwater chemistry

333 described by McLing et al. (2002). These types of abrupt vertical changes in thermal regime are
334 also seen in other volcanic terrains such as the Cascade Range (Blackwell and Priest 1996).

335 The temperature profiles of the nine deep wells for which quality temperature logs are available
336 (Figure 2) provide important insights regarding geometry and flow dynamics of the ESRP
337 aquifer (Table 1).

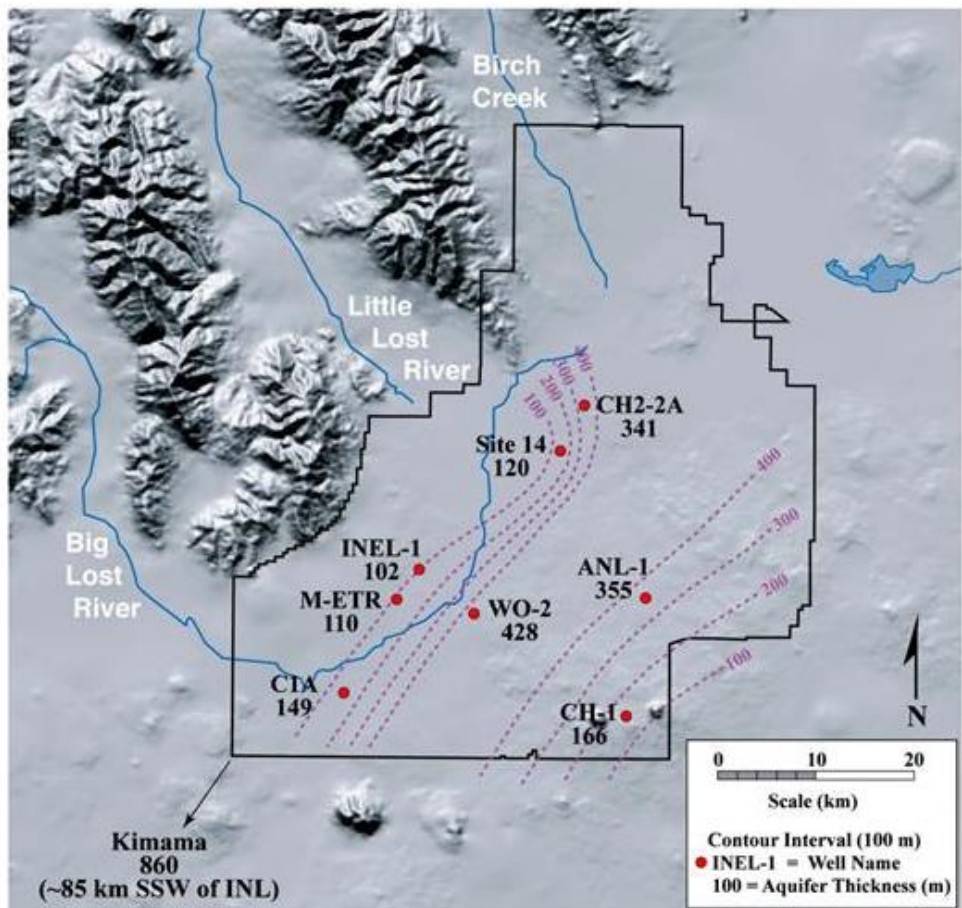
338 Table 1. Aquifer thickness as indicated by characteristics of temperature logs in deep wells at
339 Idaho National Laboratory Site and Eastern Snake River Plain.

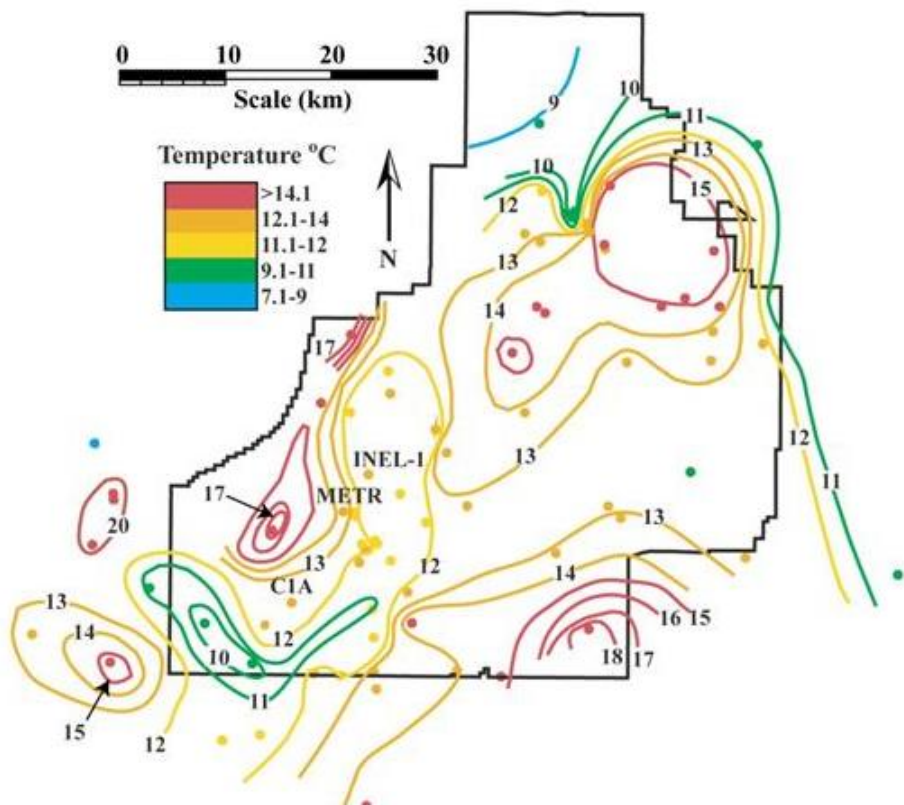
Well Name	Aquifer Thickness (m)	Depth to Aquifer Base (m)	Gradient (°C/km) Deep Aquifer
INEL-1	100	220	44
Site 14	120	200	14
CH2-2A	342	405	60
CH-1	166	450	39
C1A	149	330	49
WO-2	368	510	72
ANL-1	364	550	120
M-ETR	110	245	39
Kimama	>800	>900	75

340
341 First, the depth to the base of the aquifer (the inflection from isothermal to regional conductive
342 gradients) ranges from 100 m to >680 m beneath the water table. The aerial distribution of
343 aquifer thickness contoured from these nine deep well control points shows that a deep,
344 east-to-northeast-trending “channel” crosses the southeastern and south-central portion of the
345 INL Site (Figure 3). Six of the nine deep well logs reveal a water-table temperature of
346 approximately 12 to 13°C, but three of them (i.e., wells INEL-1, C1A, and M-ETR) have aquifer
347 temperatures of approximately 18 to 20°C and define a warm zone in the aquifer (Figure 4).
348 Vertical profiles for these wells show increasing groundwater temperatures with depth to the
349 base of the aquifer. These observations refute the suggestion by Robertson et al. (1974) that
350 warm groundwater rests above colder groundwater due to infiltrating irrigation water or playa
351 lake settings. Rather, temperature profiles in these deep wells show that heat from depth through
352 the upwelling of geothermally heated water entering into the upper productive aquifer is the
353 cause of the warm zones. In these areas, the geothermal flux is so great relative to flow of
354 groundwater that temperatures are affected from the base of the aquifer to the water table.

355

356 Figure 1. Contours of aquifer thickness on Idaho National Laboratory Site based on eight deep
357 wells for which temperature logs are available.





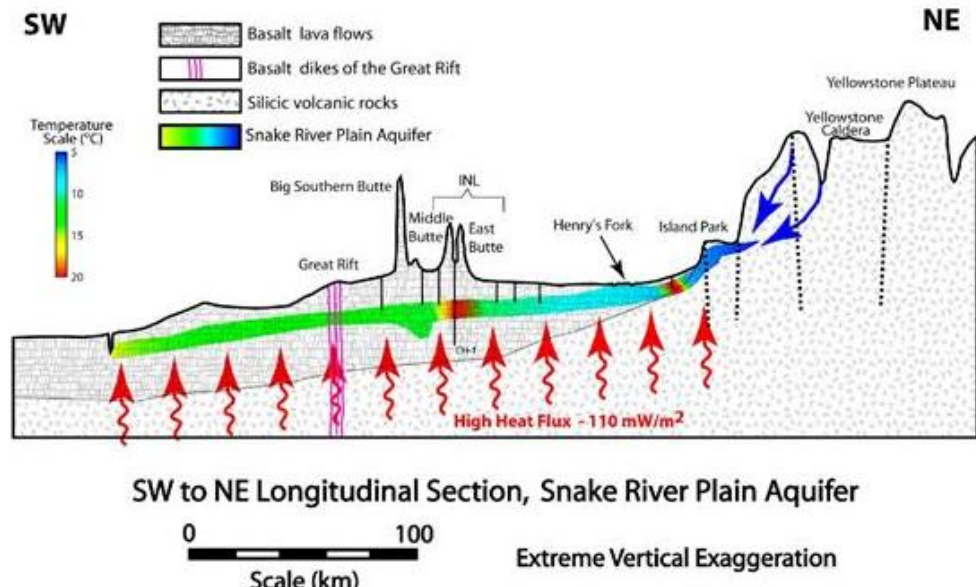
358

359 Figure 2. Aquifer temperature at water table for Eastern Snake River Plain aquifer within and
360 near Idaho National Laboratory Site.

361 5. AQUIFER TEMPERATURE DISTRIBUTION

362 The ESRP aquifer temperature distribution at the water table (Figure 4) was mapped using
363 temperature-logging data from more than 200 shallow wells in the ESRP. Figure 4 shows the
364 temperature of the aquifer is not uniform across the plain, but rather varies as a function of
365 distance from recharge areas, flow velocity, and geothermal upwelling from depth. A
366 longitudinal section of the aquifer, showing the persistent warming of the aquifer from recharge
367 to discharge zones, also was constructed from this information (Figure 5). Because of an
368 extensive groundwater monitoring program at INL, more than half of the deep wells used for this
369 study are located near the INL Site. Many additional wells are distributed across the entire plain
370 (Brott et al. 1981; Ziegos and Blackwell 1986; Bartholomay et al. 1997), especially in the
371 agricultural regions along the Snake River. Background temperatures for the aquifer generally
372 range from approximately 11 to 13°C, in the central part of the aquifer, but are punctuated by
373 several anomalously warm and cool areas (Figure 1). Figure 1 was developed from the

374 integration of data from this study for the area proximal to the INL Site with data from
375 Bartholomay et al. (1997) and Brott et al. (1981) for the larger plain.

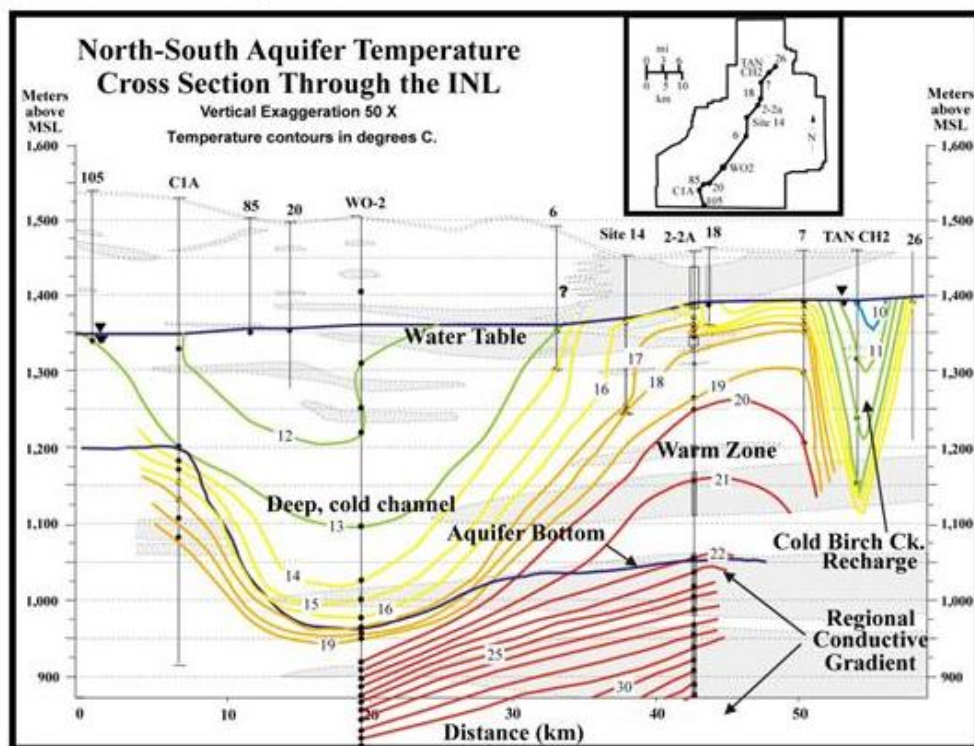


376
377 Figure 5. Simplified and idealized longitudinal section of Eastern Snake River Plain aquifer from
378 its source in the Yellowstone area to its discharge in the Thousand Springs area. Blue arrows
379 indicate recharge to the aquifer from the Yellowstone Plateau. Groundwater flow is generally
380 parallel to the section but there is considerable lateral infiltration from the highlands surrounding
381 the Eastern Snake River Plain. Only the fast-flowing upper productive aquifer is colored to
382 indicate temperature and vertical variation in temperature is assumed to be negligible compared
383 to horizontal temperature variation. The indicated temperature distribution illustrates the overall
384 warming from approximately 5°C in the source areas to approximately 16°C at the discharge area
385 and the effect of two "hotspots," one at Juniper Buttes and one in the southeastern corner of the
386 Idaho National Laboratory Site. Basal heat flux is the average annual heat flux estimated by
387 Blackwell (1989). Approximate line of section is shown in Figure 1.

388 The coldest groundwater in the ESRP aquifer (as low as 6°C) is located south of the Yellowstone
389 Plateau and in areas of recharge by the major drainages along the margins of the ESRP. In
390 contrast when compared to the regional groundwater temperature, there are anomalously warm
391 areas in the aquifer (temperatures reach or exceed approximately 18°C at the water table). These
392 warm zones occur along the margins of the plain, except in areas where the major drainages
393 enter the plain. Additional warm zones within the aquifer itself occur in the northern INL Site; at
394 the southeast corner of the Site; north of Juniper Buttes; and northwest of Jerome, Idaho
395 (Figure 1), which are upgradient of the discharge areas of the aquifer in the Snake River Canyon
396 between Twin Falls and Bliss, Idaho. These warm zones signify places where geothermal heating
397 from depth is sufficient to affect aquifer temperature at the water table, either because of slow
398 groundwater flow in the aquifer, or vigorous input of geothermally-heated water from below the
399 base of the aquifer, or both.

400 **6. VERTICAL AQUIFER TEMPERATURE DISTRIBUTION**

401 Vertical ESRP aquifer temperature distribution in the area where numerous deep wells have been
 402 drilled and logged (i.e., the INL Site area) is shown in the Figure 6 cross section, which shows
 403 the profound differences in aquifer temperature distribution and temperature gradients for
 404 different areas. The south-central area of the INL Site, represented by well ANL-1, is
 405 characterized by a channel of relatively cool groundwater that extends to a depth of
 406 approximately 400 m below the water table, below which a sharp inflection to the regional
 407 conductive gradient (within a depth interval of approximately 100 m) occurs. Data from the
 408 Kimama well provide supporting evidence that this thick channel of cool groundwater is a
 409 regional feature extending well south of the INL Site. In contrast, the north-central area,
 410 represented by wells CH2-2A, Site 14, and USGS-7 (identified as 7 on the map in Figure 6), is
 411 characterized by warm temperatures at the water table (i.e., temperatures up to 16 or 17°C),
 412 gradual warming with depth below the water table, and a less abrupt transition to the regional
 413 conductive gradient. Because this warm zone occurs in an area where sediment interbeds within
 414 the basalt sequence are numerous and thick (Helm-Clark et al. 2004), this study speculates that
 415 transmissivities are lower here than elsewhere in the aquifer and that groundwater flows
 416 sufficiently slow to allow geothermal heat from below to affect aquifer temperature throughout
 417 the entire thickness of the aquifer.



418

419 Figure 6. Detailed north-to-south cross section showing aquifer temperature distribution beneath
 420 Idaho National Laboratory Site. Lightly shaded zones are sediment interbed layers within the
 421 basalt sequence.

422 The warm zone at the southeast corner of the INL Site (Figure 4) requires an alternate
423 explanation. It occurs along the axis of the ESRP, where interbeds are few, but where volcanic
424 source areas with porous near-vent facies are abundant (Hackett and Smith 1992). In this
425 instance, the ESRP aquifer temperatures may reflect longer residence times coupled with the
426 presence of a geothermal circulation system of sufficient size that is able to overwhelm the
427 cooler productive aquifer. The interpretation that this thermal anomaly is caused by the presence
428 of a strong geothermal circulation may imply that this area is a good target for geothermal
429 exploration.

430 **7. HORIZONTAL TEMPERATURE DISTRIBUTION: IMPLICATIONS FOR**
431 **GROUNDWATER FLOW**

432 ESRP aquifer temperature variation along and across the ESRP provides useful information for
433 tracing aquifer flow paths because of the interaction of cold recharge waters (mostly snowmelt)
434 with exceptionally high heat flow (Blackwell 1989; Blackwell et al. 1992) from the crust beneath
435 the ESRP. Cold recharge water derived along the margins of the plain and from surface recharge,
436 and plumes of warm groundwater created by the upwelling of geothermal water, act as
437 long-term, large-scale tracer tests that elucidate the flow regime within the aquifer. The size,
438 shape, and continuity of these cold and warm plumes are influenced by preferential pathways for
439 groundwater flow and provide information about flow directions, relative flow velocities, and
440 lateral dispersivity of the aquifer.

441 In the main recharge area for the eastern portion of the ESRP aquifer, just southwest of the
442 Yellowstone Plateau, the groundwater is rapidly warmed from approximately 6 to 11°C
443 (Figure 6). Except for one warm well near Juniper Buttes and cold recharge from streams north
444 and south of the ESRP, aquifer temperature remains near 11 to 12°C throughout the reach from
445 the Yellowstone Plateau to the INL Site. Significant warming takes place along the eastern
446 boundary of the INL Site, and aquifer temperatures of >13°C prevail throughout much of the
447 INL Site area. Because the density of available temperature logs for wells downgradient of the
448 INL Site is much lower, the aquifer temperature effects of input from some known geothermal
449 areas such as that near Magic Reservoir are not well defined in Figure 6. However, sufficient
450 temperature data exist (e.g., Brott et al. 1981) to document the influence that the regional
451 geothermal heat flow of the plain has on the temperature of water in the aquifer. Groundwater
452 emerging from the aquifer in springs along the Snake River Canyon between Twin Falls and
453 Bliss shows that the aquifer has warmed from approximately 6°C when it was recharged to
454 14.5 to 16°C when it was discharged (Bartholomay et al. 1997; USGS 2004).

455 The areal ESRP aquifer temperature distribution provides information about aquifer flow
456 directions at both the local scale (where well density is sufficient to resolve it) and a regional
457 scale. An example of local-scale flow structure is shown in the north-central part of the INL Site
458 (Figure 4). Here, a narrow plume of cold recharge groundwater penetrates the large warm zone
459 in the central INL Site. This narrow cold plume is not just a surface feature, where cold recharge
460 water is riding on top of the regional aquifer. Rather, this cold channel penetrates to a significant
461 depth into the subsurface as shown in Figure 7. This cold channel results from aquifer recharge
462 water that flows along strong preferential pathways (probably fracture zones) aligned with the
463 regional stress field (Welhan and Reed 1997). This water flows with sufficient velocity to
464 counter the effects of geothermal heat from below. Support for this interpretation comes from
465 multiple sources including tracer tests in which injected tracers break through to distant

466 observation wells long before breaking through to nearer wells that are not within the preferential
467 pathway indicated by the temperature data (Arnett 2002). Likewise, the contamination plume
468 from the Test Area North injection well located proximal to deep well CH2 has the same overall
469 shape and direction as the narrow cold plume (INEEL 2003). The addition of the Kimama well
470 data in 2011 (Twining and Bartholomay 2011) may support the existence of a thick, cold
471 preferential channel for groundwater flow along the central axis of the ESRP, as the well is on
472 strike with the cold, thick aquifer channel at the INL Site and has an aquifer thickness of >855 m.
473 However, given the paucity of data and the distance between Test Area North area and the
474 Kimama well, this speculation should be considered tenuous at best.

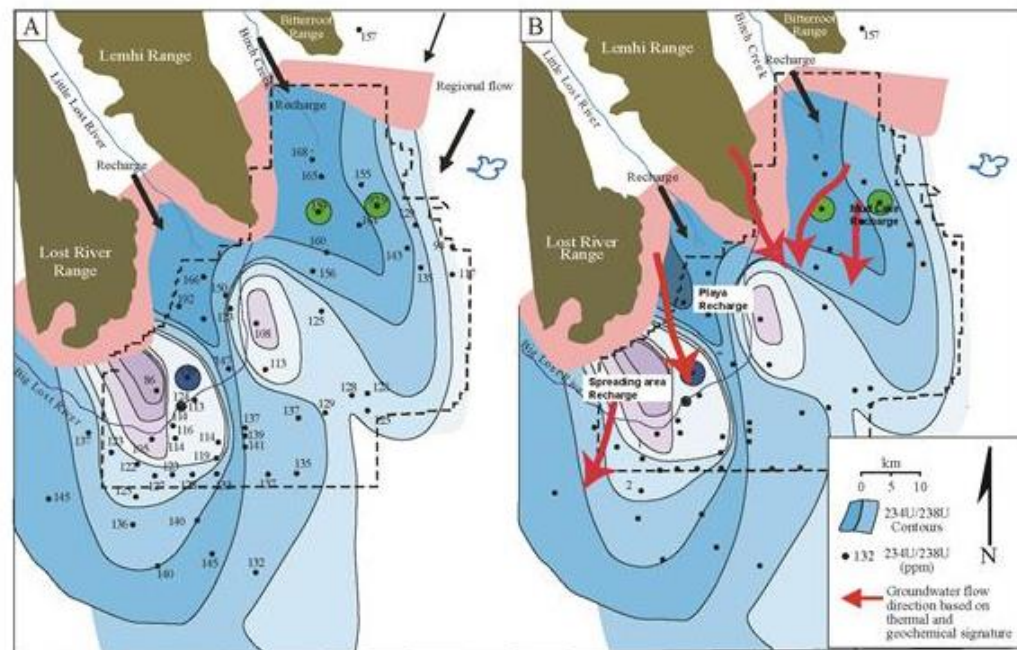
475 A zone of relatively cool groundwater with temperatures of 10 to 11°C occurs in the
476 southwestern corner of the INL Site (Figures 4 and 6) and is located in a region of the INL Site
477 where water from the Big Lost River is diverted for flood control purposes into large infiltration
478 basins in high precipitation years. This water infiltrates rapidly through the vadose zone (Wood
479 and Huang 2015) to the ESRP aquifer, where it forms an anomalously cool zone in this area of
480 the INL Site.

481 On the regional scale, the temperature distribution provides information about long-range ESRP
482 aquifer flow. Throughout the aquifer, temperature distribution reveals the numerous flow paths
483 that are defined by warm and cold groundwater moving through the aquifer (Figures 1 and 4).
484 For example, at the northeast portion of the aquifer, a warm zone near Juniper Buttes is
485 elongated to the west-southwest (Figure 1), at an oblique angle to the southwest trending axis of
486 the plain. The western elongation of this thermal anomaly rather than parallel to the axis of the
487 plain based on the regional hydraulic gradient may result from the large influx of cooler recharge
488 water from the drainage of the South Fork of the Snake River (Figure 1) as it emerges from the
489 southeastern margin of the plain near Idaho Falls, Idaho. USGS data for the Lorenzo gage on the
490 South Fork of the Snake River north of Idaho Falls shows that water temperature during the
491 irrigation season (May to September) is approximately 7 to 16°C and drops to <5°C from
492 November to March. Another major contributor to this diversion to the west is the influx of large
493 volumes of irrigation water diverted from the Snake River to support agriculture in the eastern
494 region of the ESRP. This large volume of cold-water recharge causes a ridge in the water table
495 and forces aquifer flow to the northwest, having the effect of forcing the flow from upgradient
496 parts of the aquifer through the INL Site area, most of it through the deep, cool channel
497 discussed in section 6 (Figures 3 and 6). Most of the cold water in the recharge zone from the
498 South Fork of the Snake River then flows downgradient near the southern eastern margin of the
499 plain, south to the Kimama well area. The warm groundwater zone near the southeast corner of
500 the INL Site (Figure 1) appears to be a zone of high geothermal input to the aquifer, resulting in
501 significant warming of groundwater flowing through this area. The warm flow path
502 downgradient of this warm groundwater zone remains intact throughout the reach of the aquifer
503 from the INL Site to discharge areas near Thousand Springs. Water from the cold channel at the
504 INL Site, from Birch Creek, and from the Little Lost River, flows parallel to the warm plume,
505 but remains along its northwest margin. Cold groundwater recharged from the South Fork of the
506 Snake River flows semi-parallel to it along the southeast side (Figure 1). The cold-groundwater
507 recharge plume from the Big Lost River remains close to the northwest margin of the plain and
508 merges with flow from the Little and Big Wood Rivers. The apparent persistence of the warm
509 stream for >100 km downgradient suggests that lateral dispersion in this reach of the aquifer is
510 limited.

511 Flow directions based on ESRP aquifer temperature distribution can be compared to previous
512 interpretations of flow directions (see for example, Garabedian 1986 and Ackerman et al. 2006).
513 This study's flow direction analysis based on temperature provides more details of the flow
514 regime for the area within the INL Site, where the resolution based on temperature is greater due
515 to the large number of temperature-logged wells. The presence of a warm zone in the aquifer
516 near the southeast corner of the INL Site (Figure 1) defines the western boundary between the
517 heat flow of the regional ESRP aquifer and the limit of influence that cold recharge from the
518 South Fork of the Snake River has on aquifer temperature. Although the South Fork of the Snake
519 River contributes a large amount of recharge water to the aquifer, the data for this study show
520 that this recharge is restricted to a zone that abuts the southeast margin of the plain (Figure 1).

521 **8. COMPARISON TO FLOW REGIME INDICATED BY GROUNDWATER
522 CHEMISTRY AND EQUILIBRATION OF NATURAL ISOTOPES**

523 Studies of the ESRP aquifer beneath the INL Site using naturally occurring chemical constituents
524 and isotopes of uranium and strontium support the temperature-defined flow paths presented in
525 this study. Johnson et al. (2000) and Roback et al. (2001) used uranium-234/-238 and strontium-
526 87/-86 isotope ratios to track groundwater flow paths. The areal distribution of uranium isotopes
527 provide a clear and detailed pattern of flow pathways that shows many similarities to that
528 provided by temperature data. For brevity, only the uranium data are discussed in detail.
529 However, similar conclusions can be made on the basis of strontium isotopes and to a lesser
530 extent the solute concentration data (Johnson et al. 2000). The Figure 7 map shows the
531 distribution of uranium isotope ratios and reveals flow patterns at scales of tens of kilometers in
532 length. These patterns reflect the fact that groundwater recharging the aquifer from drainages
533 north of the ESRP and from surface water sources has isotopic signatures that are distinct from
534 those of the main aquifer. This recharging groundwater, tagged with a unique natural isotopic
535 signature, can be traced downgradient until the uniqueness of the isotopic signature is lost due to
536 water-rock reaction or mixing and dilution.



537

538 Figure 7. Uranium isotope contour map, showing regions of preferential flow and low flow. High
 539 ratios characteristic of recharge source regions extend far into the aquifer in preferential flow
 540 zones (after Roback et al. 2001).

541 Despite the consistency derived from the two independent data sets (groundwater temperature
 542 and chemical signatures), there is not always direct correlation between temperature and isotope
 543 ratios at a local scale. This is especially the case along the margins of the ESRP where thermal
 544 input is highest. For example, zones with high uranium isotope ratios emanate from the valleys
 545 of Birch Creek and the Little Lost River and these zones generally correlate with the cold
 546 groundwater recharge plumes defined by the thermal profiles (Figure 6). However, when
 547 compared in detail, samples with high uranium-234/-238 isotope ratios at the mouths of the
 548 valleys of Birch Creek and the Little Lost River span a wide range of temperatures. This is
 549 interpreted to indicate that groundwater originating from these recharge valleys is warmed as it
 550 enters the ESRP aquifer proper, which along its northwest margin is an area of high heat flow,
 551 without significantly changing the isotope ratios. This implies that in these particular areas the
 552 flux of recharge water is sufficiently high to overwhelm the chemical signature of upwelling
 553 geothermal water. In a second example, cool groundwater zones in the southwest part of the INL
 554 Site and to the northeast of the INL Site correspond to zones of lower uranium-234/-238 isotope
 555 ratios. Both of these zones are interpreted to be zones of infiltration based on chemical, isotopic,
 556 and hydrologic data (Roback et al. 2001, and references therein) and based on temperature data
 557 (this study). Therefore, the fact that temperature and isotope ratios are not directly correlated is
 558 due to different mechanistic origins of the temperature and isotopic signatures. Regardless,
 559 interpretations of areal patterns of temperature and isotope ratios yield consistent flow patterns.
 560 Because of the different mechanistic origins of the temperature and isotope signatures combined,

561 use of the two data sets provides valuable information regarding the origin and evolution of the
562 groundwater.

563 **9. GEOTHERMAL IMPLICATIONS**

564 **9.1. High Geothermal Potential**

565 The many thermal springs along the margins of the ESRP (Cannon et al. 2014), the high heat
566 flow (Blackwell and Steele 1992) within the plain, and recent volcanic activity (Pierce and
567 Morgan 2009) suggest the presence of a significant geothermal potential beneath the ESRP
568 aquifer. However, the large volume of fast-flowing cold groundwater in the transmissive aquifer
569 effectively blankets the plain geothermal system. The high crustal heat flow of the plain
570 manifests itself in several geothermal springs and warm groundwater in domestic wells along the
571 margins of the plain, where the aquifer is absent or very thin. It is also apparent in the
572 temperature logs of deep wells that penetrate to depths beneath the bottom of the aquifer on the
573 plain as described in this study and Brott et al. (1981). In both these cases, heat flow
574 $>100 \text{ mW/m}^2$ is observed. In contrast, the heat flow in the plain wells drilled above or a short
575 distance into the aquifer averages only approximately 25 to 30 mW/m^2 (Brott et al. 1981),
576 illustrating the efficiency with which the aquifer intercepts heat before it reaches the near-surface
577 environment.

578 While there is little doubt concerning the existence of geothermal systems deep in the ESRP,
579 very little is known about their depth, geochemistry, and the ultimate geothermal potential. To
580 gain more insight into the plain's geothermal potential, a careful evaluation of a diversity of data
581 sets, including areal temperature distribution and temperature profiles from shallow and deep
582 wells, groundwater chemistry, and advanced computational models, is needed. Figures 1, 4,
583 and 7 show areas of commonality where isotope and temperature contours show a similar
584 pattern. This study conclude that the areas of the aquifer where the isotope and temperature
585 contours are parallel indicate flow paths over a high, uniform crustal heat flow or are areas
586 within the aquifer where the regional aquifer flow velocities are high enough to suppress the
587 thermal and chemical signature of thermal fluids. In contrast, areas where isotope and
588 temperature contours are orthogonal to the regional aquifer flow represent areas of the aquifer
589 with abnormally high heat flow (or the introduction of geothermal fluids) resulting in a positive
590 temperature anomaly or the infiltration and mixing of cooler waters for a negative temperature
591 anomaly. The conclusions provided from this study have added valuable insight into the flow
592 dynamics of the upper productive aquifer and help identify several areas of high geothermal
593 potential beneath the INL Site and ESRP.

594 **9.2. Enhanced Geothermal Potential**

595 In spite of the paucity of geothermal springs on the recently volcanically-active ESRP, the large
596 number of hot springs located on the periphery of the plain and the high heat flow in the plain
597 (Blackwell 1989), the ESRP remains an area of high geothermal potential. However, it is likely
598 that due to the depth of the geothermal system and lack of formation permeability any
599 development of geothermal energy associated with the ESRP would be through enhanced
600 geothermal system engineering. Observations made from core material collected for several deep
601 wells that penetrate through the upper productive aquifer (e.g., INEL-1, Kimama, and WO-2)
602 reveal that diagenetic processes in the deep aquifer system have effectively sealed most
603 conductive structure in the deep system. Additionally, the USGS conducted several hydraulic

604 tests in well INEL-1 (Mann 1986) at the interval of 1.3 to 3.2 km below ground surface. A
605 pumping test in this interval was conducted for 7 days and yielded an average reservoir
606 permeability of $7.2 \times 10^{-16} \text{ m}^2$ for the interval. Permeability this low in the reservoir zone
607 would almost certainly require advanced enhanced geothermal systems reservoir engineering to
608 economically develop the geothermal energy resources of the ESRP.

609 **10. SUMMARY**

610 This study documents an integrated effort, using ESRP aquifer temperature in conjunction with
611 previously-reported isotopic data (Johnson et al. 2000; Roback et al. 2001), to trace regional
612 groundwater flow to reveal the effective thickness of the aquifer and identify zones of
613 geothermal potential below the regional aquifer. Additionally, temperature data are compared
614 herein to isotope data from previous studies. Evaluation of these combined data sets confirms the
615 validity of using temperature to refine the ESRP aquifer conceptual model and geothermal
616 potential of the deep ESRP.

617 Thermal study of the nine deep wells used in this study shows details of the flow pattern in the
618 horizontal and vertical directions that have not been seen by other techniques and identified the
619 nature of the lower boundary of the transmissive portion of the ESRP aquifer (in a broad sense)
620 (Smith 2004). Surprisingly, this boundary is sharp and related to the first occurrence (with depth)
621 of moderate temperature thermal alteration (Morse and McCurry 2002) and is marked by a
622 change in groundwater chemistry from shallow Ca-Mg-HCO₃ to deep Na-K-HCO₃ type water
623 (McLing et al. 2002). A second unexpected fact is that the heat flow is high and uniform below
624 the aquifer and shows no depth variation over hundreds of meters to kilometers. Vertical
625 temperature profiles, the distribution of hydrothermal alteration and mineralization (Morse and
626 McCurry 2002), and groundwater chemistry in the ESRP aquifer (McLing et al. 2002) indicate
627 that the aquifer is comprised of two parts: an upper, cold, fast-moving aquifer and a deep, slow-
628 moving geothermal system. The shallow (or productive) portion of the aquifer occurs from the
629 water table (60 m to >200 m below land surface), to a depth of 300 to 500 m below land surface.
630 Fast-moving (1.52 to 10.51 m d⁻¹), cold (9 to 15°C), calcium- and magnesium-rich groundwater
631 characterize this part of the aquifer (Wood and Low 1986; McLing 1994). The deeper portion of
632 the aquifer is characterized by slower moving (0.006 to 0.091 m d⁻¹), warm (>30°C)
633 groundwater and has a higher sodium-potassium ratio (Mann 1986; McLing et al. 2002).
634 Although a sharp contact between these two systems is not always observed, changes in
635 geothermal gradients can be used to delineate the two systems.

636 Temperature profiles in deep wells (Figure 2) show a break in slope from an upper isothermal
637 gradient (nearly constant temperature with depth) to a deeper, moderately steep conductive
638 gradient (rapid temperature rise with depth). This study interprets this break in slope as the
639 effective base of the upper productive aquifer and the top of the deep geothermal system. Drill
640 core collected from some of the deep wells show that this break in slope also corresponds to the
641 inception of hydrothermal alteration and secondary mineralization of basalts beneath the upper
642 aquifer (Morse and McCurry 2002). The occurrence of mineral alteration is important because it
643 results in the sealing of conductive structure within the aquifer, causing permeability to
644 dramatically decrease, and allowing high heat flow from below to dominate aquifer temperature
645 below this horizon. Using these breaks in slope as a guide, aquifer thickness in the INL Site area
646 ranges from near 0 m to approximately 400 m and >855 m at the Kimama well to the south of the

647 INL Site. Deep channels of cold groundwater characterize the thickest portions of the aquifer
648 with very sharp inflection to the regional thermal gradient at depth.

649 Groundwater temperatures and borehole temperature profiles provide unique insight into the
650 geometry of the ESRP aquifer and generally support the conclusions of the isotope-preferred
651 flow path studies (Johnson et al. 2000; Lou et al. 2000; Roback et al. 2001). For example,
652 groundwater temperature at the top of the aquifer beneath the INL Site ranges from <8°C to
653 >18°C. At the regional scale, the coldest of this groundwater correlates with the preferential flow
654 corridors identified by Johnson et al. (2000) and Roback et al. (2001) and is associated with areas
655 where cold recharge moves rapidly through the aquifer system. And, regions where groundwater
656 temperature is warmer generally correlate with the slower flow regions identified by the previous
657 studies. Providing supporting evidence for the conclusion that in areas of the aquifer where there
658 are thermal anomalies, groundwater flow is slow enough that the regional geothermal gradient
659 can affect groundwater temperatures. Or, that geothermal input from depth is exceptionally
660 vigorous allowing the upwelling geothermal heat from depth to overwhelm the cold upper
661 productive aquifer. Overall, this study shows that using three-dimensional synthesis of new and
662 existing aquifer temperature data can aid in constraining three-dimensional aquifer geometry,
663 constraining groundwater flow paths, and identifying the location of potential shallow enhanced
664 geothermal systems resources.

665 **11. ACKNOWLEDGMENTS**

666 The authors would like to acknowledge the numerous past researchers who have contributed to
667 increasing the understanding of the Eastern Snake River Plain Aquifer. Specifically the United
668 States Geological Survey, Southern Methodist University and the Idaho National Laboratory

669 **12. REFERENCES**

- 670 Ackerman, D.J., G.W. Rattray, J.P. Rousseau, L.C. Davis, and B.R. Orr, 2006, A conceptual
671 model of ground-water flow in the eastern Snake River Plain aquifer at the Idaho
672 National Laboratory and vicinity with implications for contaminant transport, U.S.
673 Geological Survey, Scientific Investigations Report 2006-5122 (DOE/ID-22198), 62 p.
- 674 Anderson, M.P., 2005, "Heat as a groundwater gracer," *Groundwater*, Volume 43, No. 6,
675 November 2005, pp. 951–968, DOI: 10.1111/j.1745-6584.2005.00052.x.
- 676 Anderson, S.R., and B. Bowers, 1995, Stratigraphy of the unsaturated zone and uppermost part
677 of the Snake River Plain aquifer at Test Area North, Idaho National Engineering
678 Laboratory, Idaho, U.S. Geological Survey, Water-Resources Investigations
679 Report 95-4130 (DOE/ID-22122), 47 p.
- 680 Anderson, S.R., M.J. Liszewski, and L.D. Cecil, 1997, Geologic ages and accumulation rates of
681 basalt-flow groups and sedimentary interbeds in selected wells at the Idaho National
682 Engineering Laboratory, Idaho, U.S. Geological Survey, Water-Resource Investigations
683 Report 97-4010, 39 p.
- 684 Arnett, R.C., 2002, *TAN OU 1-07B ISB Groundwater Model Development and Initial
685 Performance Simulation*, INEEL/EXT-02-00560, Idaho National Engineering and
686 Environmental Laboratory, Idaho Falls, Idaho, June 2002, 32 p. plus appendices.

- 687 Bartholomay, R.C., L.M. Williams, and L.J. Campbell, 1997, Evaluation of radionuclide,
688 inorganic constituent, and organic compound data from selected wells and springs from
689 the southern boundary of the Idaho National Engineering Laboratory to the Hagerman
690 Area, Idaho, 1996, U.S. Geological Survey, Open-File Report OF 97-0360, 29 p.
- 691 Blackwell, D.D., 1989, "Regional implications of heat flow of the Snake River Plain,
692 Northwestern United States," *Tectonophysics*, Volume 164, No. 2, August 1989,
693 pp. 323–343, DOI: 10.1016/0040-1951(89)90025-5.
- 694 Blackwell, D.D., 1990, Temperatures and heat flow in the INEL-GT1 and WO-2 boreholes,
695 Snake River Plain, Idaho, Idaho National Engineering and Environmental Laboratory,
696 Idaho Falls, Idaho, Edgerton, Germeshausen, and Grier Informal
697 Report EGG-NPR-10690, 26 p.
- 698 Blackwell, D.D., and G.R. Priest, 1996, "Comment on "Rates and patterns of groundwater flow
699 in the Cascade Range volcanic arc and the effect on subsurface temperatures" by
700 S.E. Ingebritsen, D.R. Sherrod, and R.H. Mariner," *Journal of Geophysical Research: Solid Earth*,
701 Volume 101, No. B8, August 1996, pp. 17561–17568,
702 DOI: 10.1029/96JB01507.
- 703 Blackwell, D.D., and J.L. Steele, 1992, "Geothermal Map of North America," The Geological
704 Society of America, The Decade of North American Geology, Continent-Scale Map-006,
705 scale 1:5,000,000.
- 706 Blackwell, D.D., S., Kelley, and J.L. Steele, 1992, Heat flow modeling of the Snake River Plain:
707 Idaho Falls, Idaho, Idaho National Engineering and Environmental Laboratory, Idaho
708 Falls, Idaho, Edgerton, Germeshausen, and Grier Informal Report EGG-NPR-10790,
709 109 p.
- 710 Bredehoeft, J.D., and I.S. Papadopoulos, 1965, "Rates of vertical groundwater movement
711 estimated from the Earth's thermal profile," *Water Resources Research*, Volume 1,
712 No. 2, June 1965, pp. 325–328, DOI: 10.1029/WR001i002p00325.
- 713 Brott, C.A., D.D. Blackwell, and J.P. Ziagos, 1981, "Thermal and tectonic implications of heat
714 flow in the eastern Snake River Plain," *Journal of Geophysical Research: Solid Earth*,
715 Volume 86, No. B12, December 1981, pp. 11709–11734,
716 DOI: 10.1029/JB086iB12p11709.
- 717 Burns E.R., C.F. Williams, S.E. Ingebritsen, C.I. Voss, F.A. Spane, and J. DeAngelo, 2015,
718 "Understanding heat and groundwater flow through continental flood basalt provinces:
719 insights gained from alternative models of permeability/depth relationships for the
720 Columbia Plateau, USA," *Geofluids*, Volume 15, Nos. 1–2, February 2015, pp. 120–128,
721 DOI: 10.1111/gfl.12095.
- 722 Burns, E.R., D.S. Morgan, R.S. Peavler, and S.C. Kahle, 2011, Three-dimensional model of the
723 geologic framework for the Columbia Plateau regional aquifer system, Idaho, Oregon and
724 Washington, U.S. Geological Survey, Scientific Investigations Report 2010-5246, 44 p.

- 725 Cannon, C., T. Wood, G. Neupane, T. McLing, E. Mattson, P. Dobson, and M. Conrad, 2014,
726 "Geochemistry Sampling for Traditional and Multicomponent Equilibrium
727 Geothermometry in Southeast Idaho," *Geothermal Resources Council Transactions*,
728 Volume 38, 2014, pp. 425–431.
- 729 DeSimone, L.A., P.B. McMahon, and M.R. Rosen, 2014, "The Quality of Our Nation's
730 Waters—Water Quality in Principal Aquifers of the United States, 1991–2010," U.S.
731 Geological Survey Circular 1360, 151 p., <http://dx.doi.org/10.3133/cir1360>.
- 732 EPA, 1999, "25 Years of the Safe Drinking Water Act: History and Trends,"
733 EPA-816-R-99-007, U.S. Environmental Protection Agency, Washington, D.C.,
734 December 1999, 54 p.
- 735 Fisher, J.C., and B.V. Twining, 2011, Multilevel groundwater monitoring of hydraulic head and
736 temperature in the eastern Snake River Plain aquifer, Idaho National Laboratory, Idaho,
737 2007–08, U. S. Geological Survey, Scientific Investigations Report 2012-5259, 78 p.
- 738 Garabedian, S.P., 1986, Application of a parameter estimation technique to modeling the
739 regional aquifer underlying the eastern Snake River Plain, Idaho, U.S. Geological Survey,
740 Water-Supply Paper 2278, 60 p.
- 741 Ge, S., 1998, "Estimation of groundwater velocity in fracture zones from well temperature
742 profiles," *Journal of Volcanology and Geothermal Research*, Volume 84, Nos. 1–2,
743 August 1998, pp. 93–101, DOI: 10.1016/S0377-0273(98)00032-8.
- 744 Goode and Konikow 1990 Goode, D. J., and L. F. Konikow, 1990, "Reevaluation of Large-Scale
745 Dispersivities for a Waste Chloride Plume: Effects of Transient Flow," *International
746 Conference on Calibration and Reliability in Groundwater Modeling, International
747 Association of Hydrological Sciences, The Hague, The Netherlands*, September 1990
- 748 Hackett, W.R., and R.P. Smith, 1992, "Quaternary volcanism, tectonics, and sedimentation in the
749 Idaho National Engineering Laboratory area," in Wilson, J.R., ed., *Field Guide to
750 Geologic Excursions in Utah and Adjacent Areas of Nevada, Idaho, and Wyoming:
751 Geological Society of America Rocky Mountain Section Guidebook*, Utah Geological
752 Survey, Miscellaneous Publication 92-3, 18 p.
- 753 Helm-Clark, C.M., R.P. Smith, D.W. Rodgers, and F.K. Carroll, 2004, "Neutron Log
754 Measurement of Moisture in Unsaturated Basalt," *Vadose Zone Journal*, Volume 3, No.
755 2, May 2004, pp. 485–492, DOI: 10.2136/vzj2004.0485.
- 756 INEEL, 2003, *Update to the Test Area North Large-Scale Groundwater Flow and Transport
757 Model for the Assessment of Monitored Natural Attenuation*, INEEL/INT-03-00709,
758 Idaho Completion Project: Idaho National Engineering and Environmental Laboratory,
759 Idaho Falls, Idaho, Rev. 0, November 2003.
- 760 Ingebritsen, S.E., D.R. Sherrod, and R.H. Mariner, 1992, "Rates and patterns of groundwater
761 flow in the Cascade Range Volcanic Arc, and the effect of subsurface temperatures,"

- 762 *Journal of Geophysical Research: Solid Earth*, Volume 97, No. B4, April 1992,
763 pp. 4599–4627, DOI: 10.1029/91JB03064.
- 764 Johnson, T.M., R.C. Roback, T.L. McLing, T.D. Bullen, D.J. DePaolo, C. Doughty, R.J. Hunt,
765 M.T. Murrell, and R.W. Smith, 2000, “Groundwater “fast paths” in the Snake River Plain
766 aquifer, Radiogenic isotope ratios as natural groundwater tracers,” *Geology*, Volume 28,
767 No. 10, October 2000, pp. 871–874,
768 DOI: 10.1130/0091-7613(2000)28<871:GFPTS>2.0.CO;2.
- 769 Kuntz, M.A., S.R. Anderson, D.E. Champion, M.A. Lanphere, and D.J. Grunwald, 1992,
770 Tension cracks, eruptive fissures, dikes, and faults related to late Pleistocene-Holocene
771 basaltic volcanism and implications for the distribution of hydraulic conductivity in the
772 eastern Snake River Plain, Idaho, in Link, P.K., and Mink, L.L., eds., *Geology,*
773 *Hydrology and Environmental Remediation, Idaho National Engineering and*
774 *Environmental Laboratory, Eastern Snake River Plain, Idaho*, Geological Society of
775 America, Special Paper 353, pp. 111–133.
- 776 Kuntz, M.A., Anderson, S.R., Champion, D.E., Lanphere, M.A., and Grunwald, D.J., 2002,
777 “Tension cracks, eruptive fissures, dikes, and faults related to late Pleistocene-Holocene
778 basaltic volcanism and implications for the distribution of hydraulic conductivity in the
779 eastern Snake River Plain, Idaho”, in Link, P.K., and Mink, L.L., eds., “*Geology,*
780 *Hydrology and Environmental Remediation, Idaho National Engineering and*
781 *Environmental Laboratory, eastern Snake River Plain, Idaho,” Geological Society of*
782 *America Special Paper 353, p.111-133.*
- 783 Lewis, B. D and Goldstein, F. J. (1982) Evaluation of predictive ground-water solute-transport
784 model at the Idaho National Engineering Laboratory, Idaho, U. S. Geological Survey
785 Water-Resources Investigations 82-25Lindholm, G.F., S.P. Garabedian, G.D. Newton,
786 and R.L. Whitehead, 1987, “Configuration of the water table and depth to water, spring
787 1980, water-level fluctuations, and water movement in the Snake River Plain regional
788 aquifer system, Idaho and eastern Oregon,” U.S. Geological Survey, Hydrologic
789 Investigations Atlas HA-703, scale 1:500,000.
- 790 Lou, S., T.L. Ku, R. Roback, M. Murrell, and T.L. McLing, 2000, “Insitu radionuclide transport
791 and preferential groundwater flows at INEEL (Idaho): decay-series disequilibrium
792 studies,” *Geochimica et Cosmochimica Acta*, Volume 64, No. 5, March 2000,
793 pp. 867–881, DOI: 10.1016/S0016-7037(99)00373-7.
- 794 Mann, L.J., 1986, Hydraulic properties of rock units and chemical quality of water for INEL-1—
795 a 10,365-foot-deep test hole drilled at the Idaho National Engineering Laboratory, Idaho,
796 U.S. Geological Survey, Water-Resources Investigations Report 86-4020 (IDO-22070),
797 23 p.
- 798 McLing, T.L., 1994, *The Pre-Anthropogenic Groundwater Evolution at the Idaho National*
799 *Engineering Laboratory, Idaho*, Master of Science Thesis: Idaho State University,
800 Pocatello, Idaho, 62 p.

- 801 McLing, T.L., R.W. Smith, and T.M. Johnson, 2002, Chemical characteristics of thermal water
802 beneath the eastern Snake River Plain Aquifer, in Link, P.K., and Mink, L.L., eds.,
803 *Geology, Hydrology and Environmental Remediation, Idaho National Engineering and*
804 *Environmental Laboratory, Eastern Snake River Plain, Idaho*, Geological Society of
805 America, Special Paper 353-13, pp. 205–211.
- 806 MIT, 2006, *The Future of Geothermal Energy: Impact of Enhanced Geothermal Systems (EGS)*
807 *on the United States in the 21st Century*, INL/EXT-06-11746, U.S. Department of Energy
808 Office of Geothermal Technologies, November 2006, 48 p. plus appendices.
- 809 Morse, L.H., and M. McCurry, 2002, Genesis of alteration of quaternary basalts within a portion
810 of the eastern Snake River Plain aquifer, in Link, P.K., and L.L. Mink, eds., *Geology,*
811 *Hydrology and Environmental Remediation, Idaho National Engineering and*
812 *Environmental Laboratory, Eastern Snake River Plain, Idaho*, Geological Society of
813 America, Special Paper 353. 14p.
- 814 Neely, K.W., 2005, Nitrate Overview for the Statewide Ambient Ground Water Quality
815 Monitoring Program, 1990 – 2003; Ground Water Quality Technical Brief, Idaho
816 Department of Water Resources,
- 817 Olmsted, F.H., 1962, Chemical and physical character of groundwater in the National Reactor
818 Testing Station, Idaho: U.S. Geological Survey Open-File Report IDO-22043-USGS,
819 81 p.
- 820 Pierce, K.L., and L.A. Morgan, 2009, “Is the track of the Yellowstone hotspot driven by a deep
821 mantle plume? — Review of volcanism, faulting, and uplift in light of new data,” *Journal*
822 *of Volcanology and Geothermal Research*, Volume 188, Nos. 1–3, November 2009,
823 pp. 1–25, DOI:10.1016/j.jvolgeores.2009.07.009.
- 824 Roback, R.C., T.M. Johnson, T.L. McLing, M.T. Murrell, S. Luo, and T.L. Ku, 2001, Uranium
825 isotopic evidence for groundwater chemical evolution and flow patterns in the eastern
826 Snake River Plain aquifer, Idaho, *Geological Society of America Bulletin*, Volume 113,
827 No. 9, September 2001, pp. 1133–1141,
828 DOI: 10.1130/0016-7606(2001)113<1133:UIEFGC>2.0.CO;2.
- 829 Robertson, J.B., 1976, Numeric modeling of subsurface radioactive solute transport from waste-
830 seepage ponds at the Idaho National Engineering Laboratory, U.S. Geological Survey.
831 Open-File Report 76, 717 p.
- 832 Robertson, J.B., R. Schoen, and J.T. Barracough, 1974, The influence of liquid waste disposal
833 on the geochemistry of water at the National Reactor Testing Station, Idaho, 1952–1970,
834 U.S. Geological Survey, Open-File Report IDO-22053, 210 p.
- 835 Saar, M.O., 2011, “Review: Geothermal heat as a tracer of large-scale groundwater flow and as a
836 means to determine permeability fields,” special theme issue on environmental tracers
837 and groundwater flow, editor-invited peer-reviewed contribution, *Hydrogeology Journal*,
838 Volume 19, No. 1, February 2011, pp. 31–52, DOI: 10.1007/s10040-010-0657-2, 2011.

- 839 Ge, S., 1998, Estimation of groundwater velocity in fracture zones from well temperature
840 profiles, *Journal of Volcanology and Geothermal Research*, 84, 93-101.
- 841 Shervais, J.W., D.R. Schmitt, D.L. Nielson, J.P. Evans, E.H. Christiansen, L. Morgan,
842 W.C.P. Shanks, T. Lachmar, L.M. Liberty, D.D. Blackwell, J.M. Glen, D. Champion,
843 K.E. Potter, and J.A. Kessler, 2013, "First results from HOTSPOT: The Snake River
844 Plain Scientific Drilling Project, Idaho, U.S.A," *Scientific Drilling*, No. 15, March 2013,
845 pp. 36–45, DOI: 10.2204/iodp.sd.15.06.2013.À.
- 846 Smith, R.P., 2004, "Geologic Setting of the Snake River Plain Aquifer and Vadose Zone,"
847 *Vadose Zone Journal*, Volume 3, No. 1, February 2004, pp. 47–58,
848 DOI: 10.2136/vzj2004.4700.
- 849 Stearns, H.T., 1936, "Origin of the Large Springs and Their Alcoves Along the Snake River in
850 Southern Idaho," *The Journal of Geology*, Volume 44, No. 4, May–June 1936,
851 pp. 429–450.
- 852 Sterns, H.T., L. Crandall, and W.G. Steward, 1938, Geology and ground water resources of the
853 Snake River Plain in southeastern Idaho, U.S. Geological Survey, Water-Supply
854 Paper 774, 56 p.
- 855 Twining, B.V., and R.C. Bartholomay, 2011, Geophysical logs and water-quality data collected
856 for boreholes Kimama-1A and -1B, and a Kimama water supply well near Kimama,
857 Southern Idaho, U.S. Geological Survey, Data Series 622 (DOE/ID 22215), 18 p. plus
858 appendix.
- 859 USGS, 2004, *National Water Information System, Site Inventory for the Nation*,
860 <http://waterdata.usgs.gov/nwis/inventory>, Web page updated November 24, 2003, Web
861 page visited July 14, 2004.
- 862 Welhan, J.A., and M.F. Reed, 1997, Geostatistical analysis of regional hydraulic conductivity
863 variations in the Snake River Plain aquifer, Eastern Idaho, *Geological Society of America
864 Bulletin*, Volume 109, No. 7, July 1997, pp. 855–868,
865 DOI: 10.1130/0016-7606(1997)109<0855:GAORHC>2.3.CO;2.
- 866 Whitehead, R.L., 1986, "Geohydrologic framework of the Snake River Plain, Idaho and eastern
867 Oregon," U.S. Geological Survey, Hydrologic Investigations Atlas HA-681,
868 scale 1:1,000,000.
- 869 Williams, C.F., and J. DeAngelo, 2008, "Mapping Geothermal Potential in the Western United
870 States," *Geothermal Resources Council Transactions*, Volume 32, 2008, pp. 181–188.
- 871 Wood, T., and H. Huang, 2015, *Fluid Dynamics in Complex Fractured-Porous Systems*,
872 Chapter 14, Experimental and modeling studies of episodic air-water two-phase flow in
873 fractures and fracture networks, American Geophysical Union, July 2015, pp. 209–228,
874 ISBN 9781118877203.

- 875 Wood, W.W., and W.H. Low, 1986, Aqueous geochemistry and diagenesis in the eastern Snake
876 River Plain aquifer system, Idaho, *Geological Society of America Bulletin*, Volume 97,
877 No. 12, December 1986, pp. 1456–1466,
878 DOI: 10.1130/0016-7606(1986)97<1456:AGADIT>2.0.CO;2.
- 879 Ziagos, J.P., and D.D. Blackwell, 1986, “A model for the transient temperature effects of
880 horizontal fluid flow in geothermal systems,” *Journal of Volcanology and Geothermal*
881 *Research*, Volume 27, Nos. 3–4, March 1986, pp. 371–397,
882 DOI: 10.1016/0377-0273(86)90021-1.

Appendix D

Thermal and Geochemical Anomalies in the Eastern Snake River Plain Aquifer: Contributions to a Conceptual Model of the Proposed FORGE Test Site

Thermal and Geochemical Anomalies in the Eastern Snake River Plain Aquifer: Contributions to a Conceptual Model of the Proposed FORGE Test Site

John A. Welhan

Idaho Geological Survey, Dept. of Geosciences, Idaho State University, Pocatello, Idaho 83209-8072

welhjohn@isu.edu

Keywords: FORGE, ESRP, rhyolite, geochemical tracers, conceptual model

ABSTRACT

Data from the U.S. Geological Survey's National Water Information System (NWIS) database reveal the existence of a number of thermally anomalous areas on the eastern Snake River Plain (ESRP) aquifer, most of them near its margins, and NWIS temperature and chemistry data provided conclusive evidence that thermal waters originating in the hot rhyolitic rocks underlying the ESRP basalts inject heat and solute mass into the overlying ESRP aquifer.

Thermal waters issuing from hot felsic basement rocks in southern Idaho are Na-HCO₃ type due to water-rock reactions at elevated T. They are characteristically depleted in Ca and Mg, typically low in Cl (depending on the source water that reacts with the felsic rock), and high in pH, Na, HCO₃, SiO₂, Li and B (as well as F, if not diluted with high-Ca waters). These diagnostic tracers are seen in thermal waters ($\leq 44^{\circ}\text{C}$) that issue from shallow wells in late Neogene rhyolites of the Newdale thermal area and thermal waters ($\leq 57^{\circ}\text{C}$) sampled from INEL-1, a 3.2 km-deep borehole in rhyodacite and welded tuff.

A correlation between SiO₂ and Na/Ca molar ratio appears to be a sensitive indicator of the presence of rhyolite-labeled water, as seen in thermal waters of the Newdale area, the highest-temperature anomaly in ground waters associated with ESRP volcanic rocks, and in dilute mixtures in the ESRP aquifer adjacent to the Newdale area, as well as in warm ground waters of the ESRP aquifer near the INL.

On the INL, contamination from anthropogenic sources and from recharge of both cold tributary surface and ground waters along the aquifer's northern margin renders geochemical tracing of thermal water ineffective in the area of the proposed FORGE test site. The clearest evidence of thermal water entering the aquifer through its base is seen 10-20 km to the southeast where previously identified thermal and geochemical anomalies have been identified, characterized by elevated Na, SiO₂, Li, B and slight enrichments in F, as well as high dissolved He.

An estimate of the advective flux of thermal water in this area was derived via a two-component mixing model. Based on published aquifer flux and porosity information, however, the magnitude of the estimated thermal flux through the base of the aquifer is incompatible with core-scale data on the rhyolite's hydraulic conductivity and vertical gradient observed beneath the INEL-1. This suggests that advective heat transport from the rhyolite is not spatially uniform but focused along localized preferential flow paths within the rhyolite and the mineralized basalts that overlie the rhyolite. This interpretation is consistent with observations of thermal fluid flow in INEL-1's fractured rhyolitic rocks and supports the hypothesis that the rhyolitic basement hosts preferential flow paths.

These findings were incorporated in a geohydrologic conceptual model of the proposed INL FORGE field site.

1. INTRODUCTION

The tremendous geothermal potential of hot rhyolitic rock beneath the eastern Snake River Plain (ESRP) along the track of the Yellowstone hotspot has long been recognized (MIT, 2006), but information necessary for effective exploration and development of this resource, such as its hydraulic characteristics and advective vs. conductive heat transfer mechanisms, has been hard to come by. Except for a very few deep geotechnical and monitoring wells on and near the Idaho National Laboratory (INL) and a few such wells in other locations on the ESRP, too little is known of the rhyolites to effectively constrain its regional thermal structure or our conceptual models of EGS-mineable heat. In the WSRP, for example, a study by Arney et al. (1982) illustrated the relevance of a wide variety of geophysical and geochemical information to assess EGS potential. As part of the Snake River Geothermal Consortium, the Idaho Geological Survey is working on the FORGE initiative to identify an EGS test site on the ESRP. This report the results of an analysis of thermal and geochemical data from the ESRP aquifer that have not previously been evaluated in a geothermal context, in order to refine the geohydrogeologic conceptual model of this thermal resource.

2. GEOHYDROLOGIC BACKGROUND

The ESRP comprises a complex sequence of volcanic materials that record the passage of the Yellowstone hotspot beneath the western North American plate beginning in early to middle Miocene time (Brott et al., 1981). Fractured and highly permeable basalt lava flows of Pliocene and younger age, intercalated with minor amounts of fine to coarse eolian, fluvial and playa sediments, hosts an active, fast-flowing aquifer in the uppermost part of the basalt section (Smith, 2004). Total basalt thickness approaches 2 km in the central portion of the basin, but secondary mineralization has reduced porosity and permeability by orders of magnitude in the deeper basalts (e.g., Morse and McCurry, 2002) and created an effective hydraulic base to the ESRP aquifer. This restricts active ground water flow to the

uppermost ca. 100 to 500 meters of the basalts in the vicinity of the INL (e.g., McLing et al., 2014). Underlying this mineralized aquifer base are more than 3 kilometers of ignimbrite, welded tuff, rhyolitic and granitic basement (hereafter collectively referred to as “rhyolite”) that reflect the pervasive silicic volcanism and caldera collapse that occurred in the wake of the hotspot’s passage.

Figure 1 depicts some of the many caldera collapse structures that have been postulated to underlie the ESRP basalts (Morgan 1984; Morgan and McIntosh 2005; Drew et al. 2012; Anders et al. 2013). Total volume of erupted felsic material, primarily ignimbrite, has been estimated from 750 km^3 to $>1800 \text{ km}^3$ (Morgan and McIntosh, 2005). Although the permeability of these rocks is generally low (e.g., Mann, 1986), intracaldera collapse breccias, ring dikes and fracture zones may be permeable (Branney, 1995; Cole et al., 2005). Deep boreholes that penetrate the rhyolitic rocks beneath the ESRP reveal the existence of open fractures that support active flow zones within otherwise hydraulically “tight” rock (Moos and Barton, 1990; Moody, in press, 2015).

These deep, felsic rocks retain considerable heat, possibly augmented locally by younger heat sources, as expressed in late Quaternary rhyolite domes and crypto-domes of the ESRP. Although the flow of ground water in the basalt aquifer masks high heat flow at depth (e.g., Brott et al., 1981), three quarters of the ESRP’s area is thought to exceed 200°C at 4 km depth, making these hot rhyolitic rocks one of the highest-value EGS exploration targets in the U.S. (MIT, 2006; Podgornay et al., 2013; McLing et al., 2014).

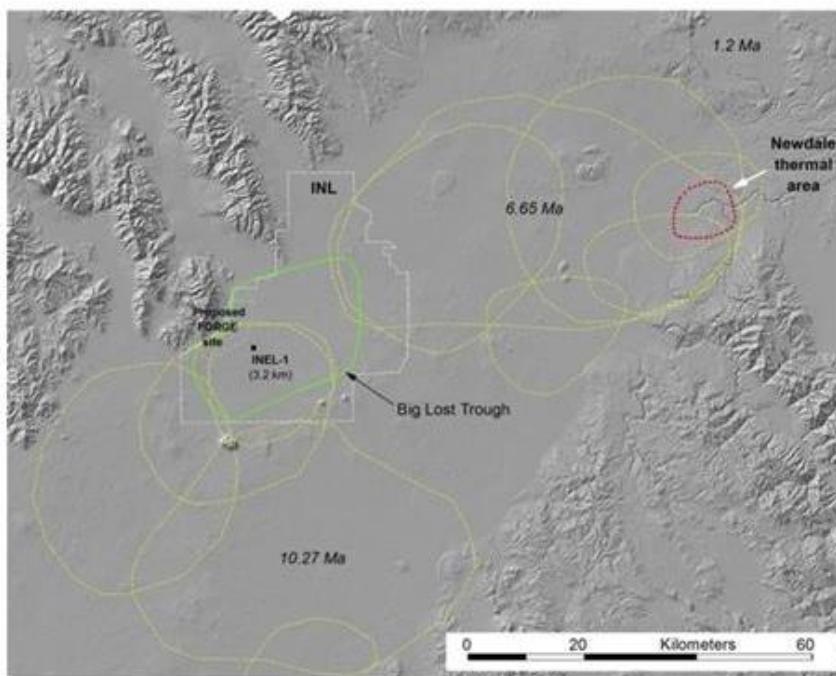


Figure 1: Inferred buried caldera collapse structures beneath ESRP basalts, after M. McCurry (written comm., 2015) based on Morgan (1984); Morgan and McIntosh (2005); Drew et al. (2012); Anders et al. (2013). Area designated as Big Lost Trough represents a long-lived topographic depression that has controlled sedimentation and basalt accumulation for over 0.5 Ma (Bestland et al., 2002), which may be an expression of one or more buried collapse structures in rhyolitic basement rocks.

3. NWIS DATABASE

The USGS’s National Water Information System (NWIS) database (<http://maps.waterdata.usgs.gov/mapper/index.html>) contains a wealth of data on the temperature and chemistry of ground waters in the ESRP aquifer, including trace-element data (**Figure 2**). The data reported on here have not been filtered by well depth, sampling time or aquifer lithology of the producing zone and represent samples collected from individual wells that have been sampled at various times, in some cases spanning a period of decades, by pumping from fixed depths within the aquifer. This report represents a preliminary evaluation of the NWIS data for the purpose of determining whether it sheds useful light on thermal influences in the ESRP aquifer and testable hypotheses with which to constrain geohydrologic conceptual models of the EGS resource beneath the ESRP aquifer.

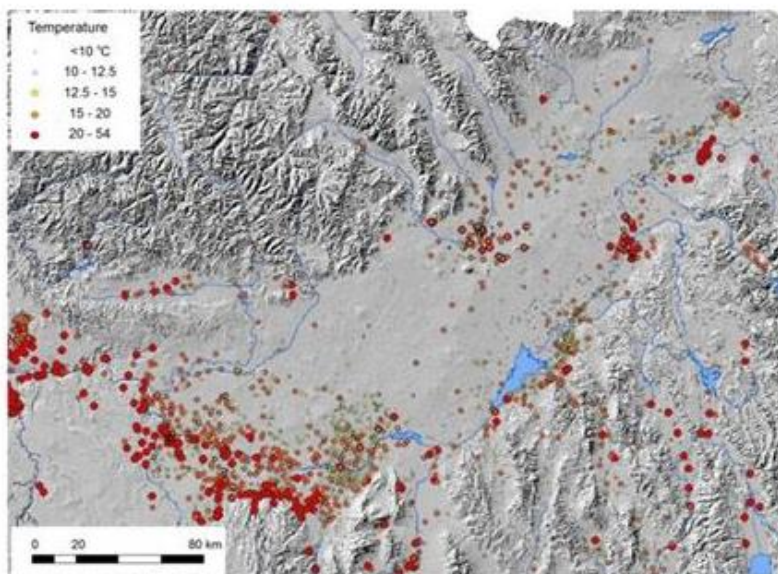


Figure 2: All available temperature data from USGS National Water Information System database for ground waters sampled in southeast Idaho from 1911 to 2015.

3.1. Thermal Data

A number of multi-level sampling systems have been installed on the INL recently, which provide discrete temperature and water quality information from discrete depth intervals within a well (Bartholomay and Twining, 2010). **Figure 3** summarizes all available temperature data from the NWIS data set collected from well Middle 2050A, indicating two important features: (1) pre-2008 data collected by contractors prior to adoption of formal sampling protocols (R. Bartholomay, pers. comm., 2015) shows considerable scatter ($2\sigma \sim 1$ °C); and (2) thermal equilibration following drilling, particularly in low-yield and/or infrequently sampled wells could take several years in areas where aquifer permeability or ground water velocities are low. For some wells, therefore, even though measurements were made using standardized protocols, the NWIS temperature data may contain significant uncertainties due to factors such as infrequent or incomplete purging and contributions of water from different depths when sampled under different hydrologic conditions.

The great majority of the ESRP-area wells in the NWIS data set represent ground water from the shallow basalt aquifer; a very small subset of sampled wells represent water issuing from rhyolitic rocks in the Ashton and Newdale areas. As shown in **Figure 4**, the NWIS temperature data define several areas that have ground water temperatures above ambient (defined as ca. 10–12 °C over most of the ESRP). The tendency of anomalous temperatures to cluster near the margins of the aquifer indicates that the source of this thermal water lies beneath these areas. Whether these thermal manifestations reflect upwelling directly from the underlying hot rhyolitic rocks or whether thermal water rises along structural heterogeneities at the basin margins is not known.

3.2. Regional Geochemical Context

Table 1 summarizes key major and trace-element characteristics of ground water from thermally influenced areas in southern Idaho that reflect the geochemical fingerprint of thermal reaction with felsic rock. Relative to ambient, non-thermal ground water characteristic of the ESRP aquifer, these thermal waters display a striking shift in major-ion composition to Na-HCO₃-type water, with decreased Ca, Mg and increased SiO₂, consistent with thermodynamic predictions of Ramirez-Guzman et al. (2004). They are also greatly enriched in F (indicating they are not influenced by mixing with Ca-rich ground water), as well as Li and B. The fact that thermal waters from the Banbury area are much higher in Cl, while sharing all other characteristics, suggests that the Cl content of the initial reacting water may be a determining factor, as born out by reaction-path modeling (e.g., Ramirez-Guzman, 2004), which shows that the Cl content during reaction with granite remains unchanged.

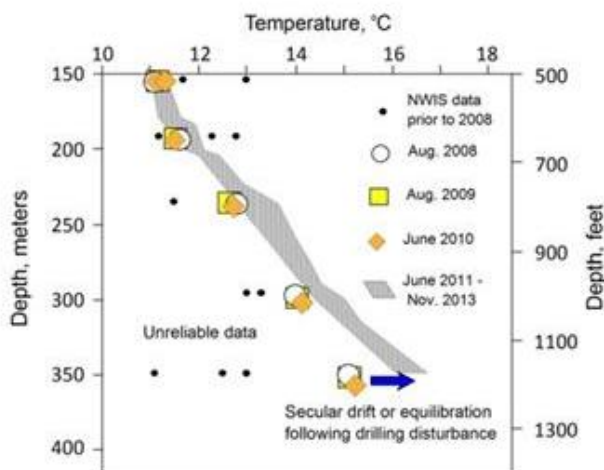


Figure 3: Example of USGS multi-level well temperature data from well Middle 2050A (drilled 2005), showing poor precision of pre-2008 measurements collected by contractors relative to post-2008 data collected by USGS using consistent sampling protocols. The post-2008 data suggest that thermal equilibration in this well occurred over a time span of at least five years following drilling.

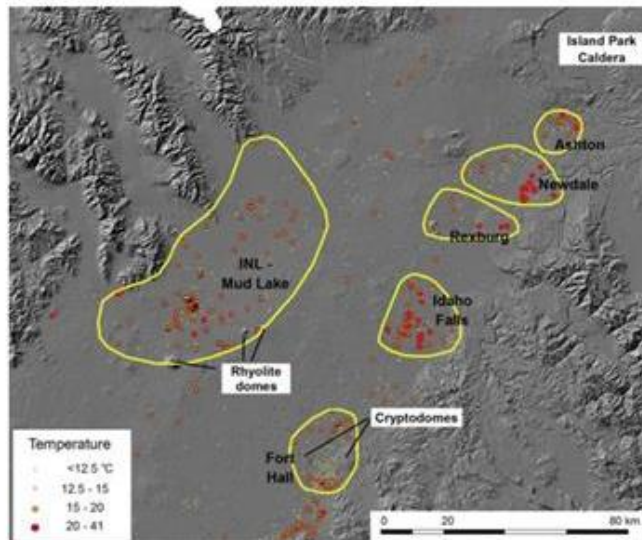


Figure 4: Locations of thermally affected areas in the eastern Snake River Plain aquifer, which may inform on the mechanisms of heat transport from underlying rhyolitic rocks (the EGS resource) into the shallow flow system as well as on the hydraulic characteristics of the resource.

Area		T, °C	pH	Ca	Mg	Na	K	SiO ₂	HCO ₃	CO ₃	SO ₄	Cl	F	Li	B	Water Type	Sources	
INL rhyodacite (INEL-1 deep borehole)	Mean	48	8.1	8.1	0.9	363	8	85	833		88	14	13	0.29	0.39	Na-HCO ₃	Mann, 1986	
	2 σ	19	0.4	1.6	1	61	2	30	122		34	5	1	0.01	0.62			
n = 3	Min	38	7.9	7.3	0.5	330	8	71	780		69	12	12	0.28	0.03			
	Max	57	8.8	8.9	1.1	390	9	101	900		99	17	13	0.29	0.58			
Idaho batholith	Mean	68	9.1	1.8	0.1	82	2	79	54	42	26	9	13	0.08	0.09	Na-HCO ₃	Druschel, 1998	
	2 σ	32	0.7	2.5	0.1	51	2	37	90	81	23	17	10	0.07	0.11			
n = 17	Min	42	8.0	0.9	0.0	52	1	46	1	0	10	1	2	0.03	0.02	White, 1967		
	Max	88	9.6	6.1	0.2	160	5	105	160	118	45	39	22	0.13	0.20	Young, 1985		
																Youngs, 1981		
Boise Front	Mean	76	8.4	1.8	0.1	84	1	58	139		22	7	16	0.04	0.08	Na-HCO ₃	Berkeley Group, 1990	
	2 σ	14	0.8	1.2	0.1	7	1	26	51		6	6	6	0.02	0.03			
n = 8	Min	65	7.6	1.3	0.0	79	1	32	110		16	1	12	0.03	0.06	Mayo & others 1984		
	Max	88	8.8	3.2	0.1	89	2	78	171		26	11	19	0.05	0.09			
Mountain Home area	Mean	51	9.0	4.5	0.2	85	2	106	128	29	10	8	12	0.01	0.12	Na-HCO ₃	Arney et al., 1992	
	2 σ	11	Min	30	7.8	0.9	0.2	52	1	42	50	0	5	2	0.00	0.06		
	Max	68	9.6	16.0	0.0	160	5	145	447	49	17	16	20	0.03	0.23			
	2 s	29	1.2	8.3	0.3	57	3	71	236	35	7	8	13	0.02	0.13			
Banbury Hot Springs	Mean	64	9.3	1.1	0.1	130	1	88	67	49	32	40	21	0.05	0.39	Na-HCO ₃ -Cl	Lewis and Young, 1982	
	2 σ	13	0.4	0.5	0.0	37	0	12	26	16	7	25	12	0.02	0.23			
n = 7	Min	57	8.0	0.7	0.1	100	1	82	56	35	27	23	14	0.04	0.28			
	Max	72	9.5	1.5	0.1	150	2	100	90	58	35	51	27	0.06	0.51			

Table 2: Summary of major ion and F, Li and B concentration (all as mg/l) characteristic of thermal waters in felsic rock environments of the Snake River Plain and Idaho batholith.

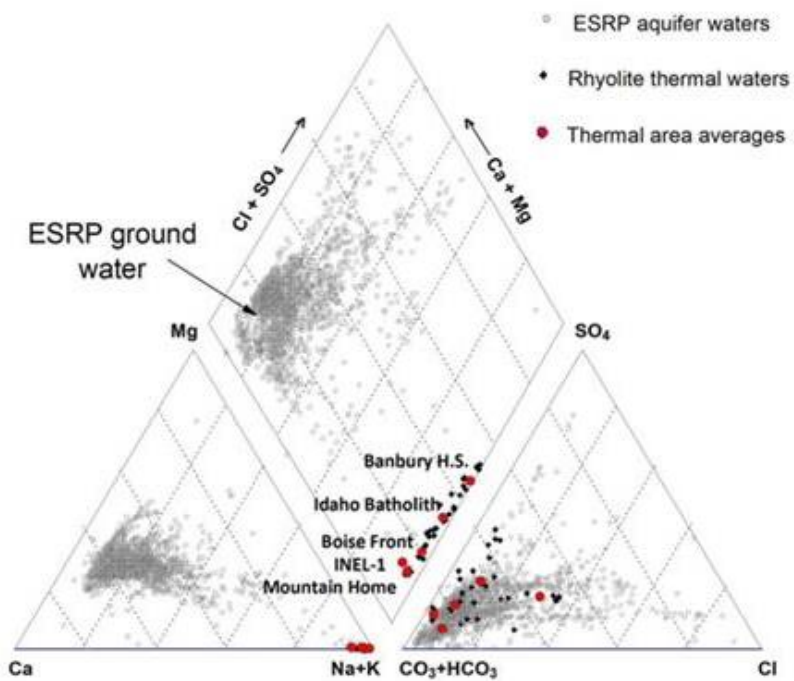


Figure 5: Piper plot summarizing major-ion compositions of ESRP ground water relative to thermal waters that issue from rhyolitic and granitic rocks of southern and central Idaho, which are characteristically depleted in Ca, Mg and enriched in Na, HCO₃, SiO₂ and occasionally Cl, where Cl-rich sedimentary waters have reacted with the hot rock.

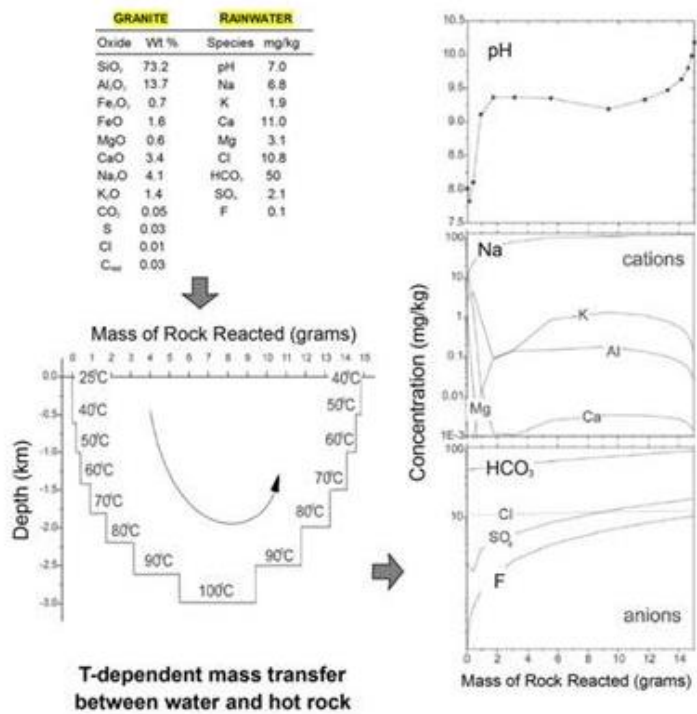


Figure 6: Origin of high-pH, Na-HCO₃-type water as a consequence of a multi-stage reaction path for meteoric water in contact with a granite at elevated temperatures. From Ramirez-Guzman et al. (2004), based on simulations using the CHILLER reaction-path code of Reed and Spycher (1984).

Figure 5 shows general compositional variations in NWIS major-ion data for ground waters of the ESRP aquifer and emphasizes the extreme difference in major-ion composition of thermal waters issuing from hot rhyolitic and granitic rocks of southern and central Idaho, including those adjacent to and that underlie the ESRP aquifer. In general, thermal water-rock reactions between ground waters and these rocks shift the major ion composition away from a Ca-Mg-HCO₃ type that characterizes ESRP ground water toward a strongly Na-HCO₃ composition. As predicted thermodynamically on the basis of reaction-path modeling (e.g., Ramirez-Guzman et al., 2004; **Figure 6**), depletion of Ca²⁺ and Mg²⁺ and enrichment of Na⁺, HCO₃⁻, SiO₂, pH and F⁻ are diagnostic of thermal waters that react with granitic rocks. A similar pattern of tracer behavior in thermally affected ground waters of the ESRP would suggest that such waters have interacted with felsic rocks at elevated temperatures and are geochemically so labeled.

3.3. Trace-element Abundances

Thermally anomalous ground waters of the ESRP aquifer (Figures 2 and 4) display certain trace-element enrichments that are diagnostic of thermal waters in contact with felsic volcanic rocks. Enrichments of F, Li and B have been reported in thermal waters of the Idaho batholith as well as in ground waters along the margins of the western SRP (Waag and Wood, 1987; Krahmer, 1995; Druschel, 1998) and have been sampled within the deep borehole, INEL-1, that was drilled into hot rhyolitic rocks beneath the ESRP aquifer (Mann, 1986). Work by Fisher et al. (2012) presented the latest assessment of some of these data in the immediate vicinity of the INL, demonstrating that shallow tributary recharge from the highlands in the vicinity of the aquifer's margins encroaches on and dilutes diagnostic tracers like Li and B in a systematic fashion.

3.4. The Newdale Thermal Area

Figure 7 shows the Newdale thermal area noted in Figure 4, located on the northeastern flank of the ESRP aquifer. In this area, waters up to 44 °C issue from shallow wells (≤ 300 m) completed in late-Neogene rhyolitic rocks. Ground water in this thermal area serves as a useful end member for evaluating geochemical patterns that arise from high-temperature water-rock reactions with rhyolitic rocks of the ESRP. It also provides a convenient site for examining the low-T waters of the nearby ESRP aquifer for evidence of tracers that could be used to identify thermal water inputs to the aquifer from the adjacent thermal area.

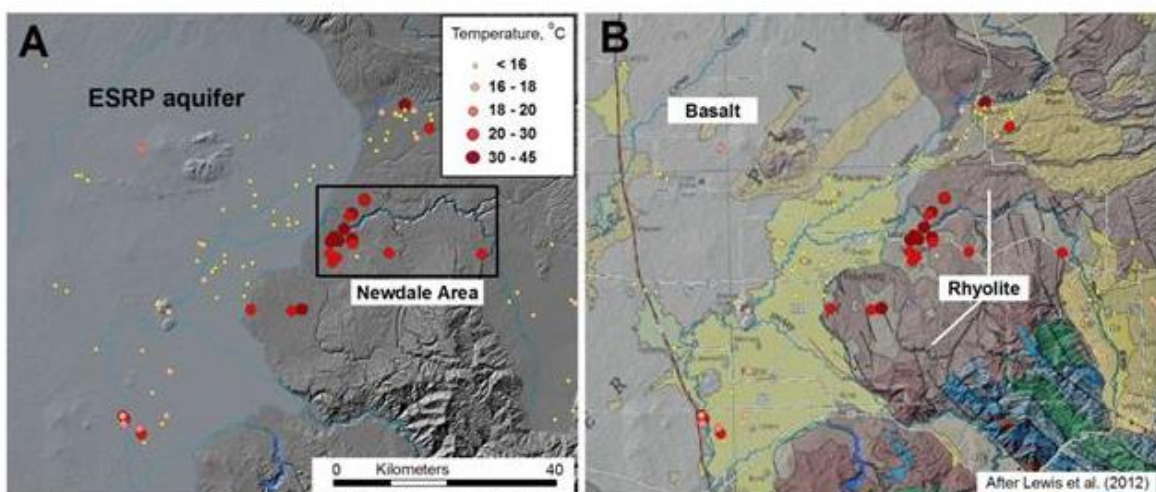


Figure 7: (A) Location of the Newdale thermal area on the northeastern flank of the ESRP aquifer, showing locations of thermal wells completed in late-Neogene rhyolitic rocks of the Heise Group (B). Also shown are locations of low-temperature wells in the ESRP aquifer (A) adjacent to the Newdale area that were evaluated for their tracer patterns and behavior, which might indicate a thermal contribution to ground waters in this part of the ESRP aquifer.

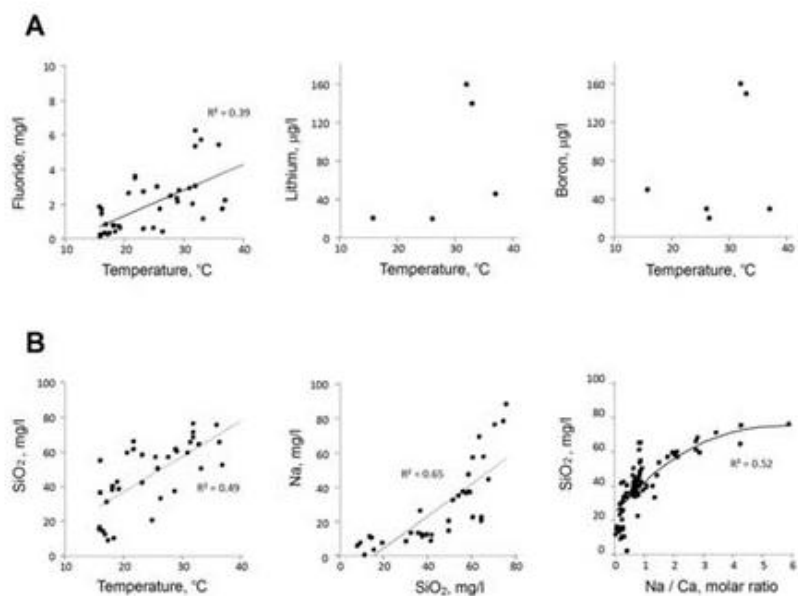


Figure 8: Tracer behavior in thermal well waters of the Newdale thermal area ($> 16^\circ\text{C}$), showing key relationships in (A) minor and trace elements and (B) correlations among major elements.

Figure 8 summarizes concentrations of major and minor solutes as reported in the NWIS database for Newdale thermal waters ($\geq 16^{\circ}\text{C}$) that issue from rhyolitic rocks outside the ESRP aquifer. Evidence for rhyolite water-rock labeling is seen in elevated F, Li and B concentrations (Figure 8A), although the data are insufficient to discern any meaningful patterns in Li and B, as well as Na, SiO₂ and Na/Ca ratio. Fluoride concentrations are characteristically limited by fluorite (CaF₂) solubility when Ca²⁺ concentrations exceed 20-30 mg/l in mixtures of Ca-rich ground water.

Figure 9 shows solute tracer behavior in low-temperature ($< 16^{\circ}\text{C}$) ground waters of the ESRP aquifer adjacent to the Newdale thermal area (Figure 7). Note that the correlation of SiO₂ vs. Na/Ca ratios is almost identical to that seen in Newdale's thermal waters (Figure 8) for Na/Ca ratios < 2 , suggesting that this correlation may be a sensitive indicator of rhyolite-labeled thermal water where it enters the ESRP aquifer.

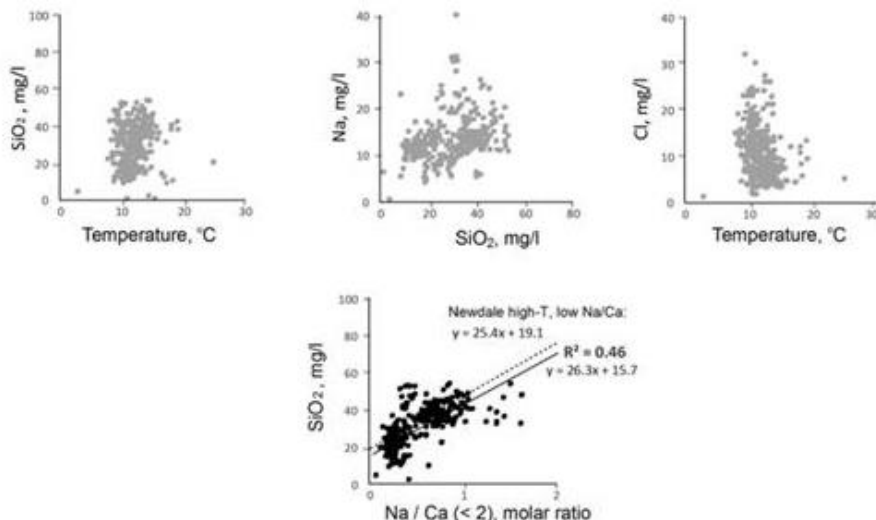


Figure 9: Tracer behavior in low-temperature ($< 16^{\circ}\text{C}$) ground waters of the ESRP aquifer adjacent to the Newdale thermal area. Unlike other solute tracers of rhyolite-labeled thermal waters, which display no useful information (grayed symbol plots), the SiO₂ vs. Na/Ca correlation is almost identical to that observed in Newdale thermal waters in which Na/Ca < 2 .

3.5. The Idaho National Laboratory Area

The geochemical patterns observed in the Newdale area are clearly consistent with dilution of rhyolite-labeled thermal water with local Ca-Mg-HCO₃ ground water. In other thermal areas, such as the Rexburg and Ashton areas (Figure 4), high Cl- concentrations observed in the thermal end-member suggest that Cl-rich sedimentary fluids reacted with rhyolitic rock, similar to the Cl-enriched thermal waters of Banbury Hot Springs (Table 1). Even more complex behavior is seen in the Idaho Falls thermal area, with evidence of rhyolite-labeled thermal waters, Cl-enriched thermal waters, and possible anthropogenic water sources (e.g., infiltration from drain wells and canals; Welhan, 2015).

The most complex tracer relationships are observed in wells of the INL thermal area, reflecting local anthropogenic contamination but also mixing processes within boreholes open over a wide depth interval and those that are sampled at multiple depths. **Figure 10A** shows a sitewide plot of 67 samples in which Li correlates with B, and Li correlates with temperature in all but a small subset of samples (Figure 10B); this subset is not site specific and is geographically scattered. Far fewer boron data are available sitewide (not shown), and do not show a correlation with temperature.

Figure 11 summarizes the principal types of Cl vs. T behavior observed in individual INL wells. The majority display essentially isothermal behavior but with large Cl variations (Figure 10B, C). Possible reasons are that Cl is locally introduced from anthropogenic sources (storage ponds, disposal wells, storm water retention basins), and intra-borehole flow in wells open over large intervals may promote mixing of hydrostratigraphic units of different water types (e.g., Bartholomay and Twining, 2010).

4. DISCUSSION

The NWIS data for the Rexburg, Idaho Falls and INL thermal areas indicate that anthropogenic influences as well as water-rock reactions other than with felsic volcanics (e.g., sedimentary rocks) can limit the utility of geochemical tracing. However, where such influences can be ruled out, trace element and temperature information appear to be diagnostic indicators of thermal waters that have originated within the hot rhyolitic rocks of the ESRP.

Table 2 summarizes data on basaltic and felsic rocks from southern Idaho, showing that rhyolitic rocks of the Snake River Plain / Yellowstone volcanic province have much higher Cl and F, elevated Li and slightly higher B compared to SRP basalts, with Cl and F contents in the same range as the granitic rock composition used by Ramirez-Guzman et al. (2004) in their modeling of water-rock interaction (Figure 6). Available B analyses of SRP basalt are very similar to mid-ocean ridge basalt (MORB), whereas the available analyses of evolved basalts at Craters of the Moon show higher B levels, consistent with these rocks' evolved nature.

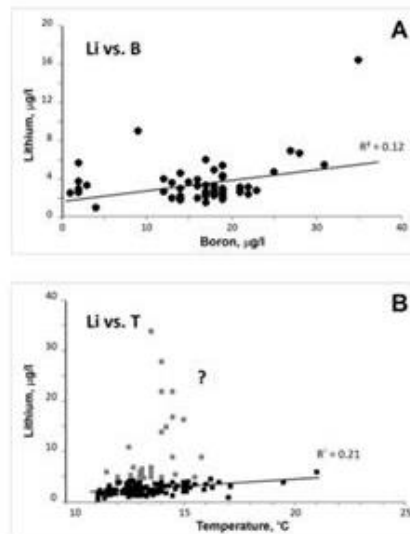


Figure 30: (A) All available NWIS data on Li and B in INL ground waters; far fewer B data (not shown) are available and do not correlate with temperature. (B) Aside from those high Li values shown in grey symbols (possibly reflecting anthropogenic contamination), which exceed the mean of Li values plotted in (A), the great majority of Li concentrations sitewide correlate with temperature at > 99.5% confidence.

Figure 12 depicts the shift in major-ion and trace-element chemistry that occurs in deep borehole INEL-1, a well that was drilled to a depth of 3160 m near the margin of the ESRP, in which rhyodacite and welded tuff comprise the section between 750 m depth and TD (Mann, 1986). These thermal waters also display characteristic major and minor element relationships that reflect thermal reactions with felsic rock, and highlight the striking contrast between these waters and the shallow basalt aquifer (Ca-HCO₃-type above ca. 750 m depth), with very low F, Li. The underlying welded tuff and rhyodacite, in contrast, host a Na-HCO₃-type thermal water considerably enriched in F, Li and B. The step-like change in composition reflects the shift from low-temperature water-rock reactions characteristic of the ESRP aquifer (e.g., Wood and Low, 1988) to reactions with felsic rocks at elevated temperature.

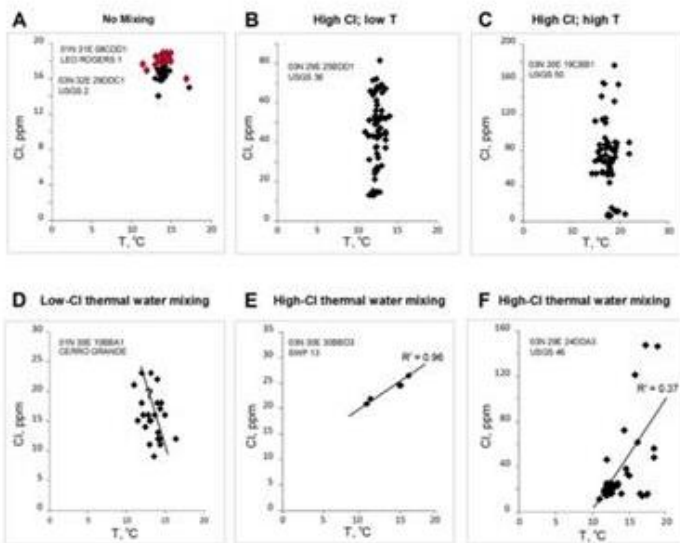


Figure 41: Examples of the most common types of Cl and temperature variability seen in INL-area wells. A minority of wells display no evidence of a mixing relationship (A), whereas the overwhelming majority is characterized by isothermal behavior with large variations in Cl (B, C). Relatively few wells display clear evidence of two-component mixing, such as between ambient ground water with a thermal water having low Cl (D) or elevated Cl (E, F).

Rock type	Sample provenance	wt. %		ppm				Source	
		SiO ₂	CaO	Na ₂ O	Cl	F	Li		
Basalt, MORB	Famous area, MAR; Tamayo FZ; Juan de Fuca Ridge; EPR; 48 analyses	47.0 - 51.5			5.6 (3-17)	1.8 (3-11)		1	
Basalt, SRP	Gerritt basalt, Mesa Falls (~0.2 Ma)	47.8	11.47	2.35		4.2	1.1	2	
" "	Fissure basalt, Spencer Kilgore (~0.5 Ma)	44.2	11	2.15		10.2	1.5	2	
" "	Kimama flow (15 ka)	45.2	7.5	3.5		21		3	
" "	Lava Creek flow, Craters of the Moon (13 ka)	43.5	8.13	3.47		19		3	
Average SRP Basalt		45.2	9.5	2.9	<<20*	<<100*	13.6	1.3	
Basalt, evolved	Devils Orchard flow, Craters of the Moon (~5 ka)	62.1	3.2	4.55		34.4	11.1	2	
" "	Highway flow, Craters of the Moon (2.4 ka)	62.9	2.94	4.2		30		3	
" "	Serrate flow, Craters of the Moon (2.4 ka)	59.9	3.55	4		30		3	
Average COM Basalt		61.6	3.2	4.3		31.5	11.1		
Rhyolite	Cougar Point tuff, Bruneau-Jarbridge eruptive center (11.5 Ma), three analyses	74.3	1.1	2.63		29.6	11.2	2	
"	Lava Creek Tuff Member B, east of Magic Reservoir (0.64 Ma)	76.9	0.53	3.78		49.6	11	2	
"	Big Southern Butte, obsidian (0.3 Ma)	75.9	0.48	4.4		116.7	22.4	2	
"	Big Southern Butte, obsidian (0.3 Ma)	74.8	0.47	4.33	2000	2900		4	
"	Moonstone Mountain, NW of Magic Reservoir	74.3	0.83	3.43	< 500	2100		4	
"	Wedge Butte flow, SE of Magic Reservoir (3.0 Ma)	74.7	0.7	3.94	< 500	4200		4	
"	Ammon quarry, ash-flow tuff (4.1 Ma)	71.3	0.99	3.16	< 500	400		4	
"	Lost River Range near Howe, vitrophyre	76.5	0.53	3.37		1200		4	
"	Nez Perce flow, Yellowstone plateau (0.15 Ma)	76.9	0.49	3.58		41.2	12.5	2	
"	Canyon flow, Yellowstone plateau (0.48 Ma)	75.5	0.89	2.7			12.8	2	
"	Crystal Springs flow, Yellowstone plateau (70 ka)	76.9	0.49	3.99		74.6	12.5	2	
"	Obsidian Cliffs flow, Yellowstone plateau (0.17 Ma)	77.1	0.45	3.93		71.3	12.8	2	
Average SRP Rhyolite		75.4	0.7	3.6	<500	2160	63.8	13.6	
Topaz rhyolite	China Hat flow (57 ka), seven analyses	Topaz Rhyolite **	73.7 ± 5.6	0.7 ± 0.9	4 ± 0.3	380 ± 247	4322 ± 1586	95 ± 18	5.6 ± 7

* inferred from contents of MORB vesicles (Kagoshima et al., 2012)

** mean and 2 σ range

1 - Ryan and Langmuir (1987, 1993)

2 - Savov et al. (2009)

3 - Kuntz et al. (1992)

4 - Leeman (1982)

5 - Lewis and Kauffman (2013)

6 - Ford (2005)

Table 2: Comparative summary of available data on F, Li, and B content of basalts and rhyolites of the SRP and vicinity.

4.1. Implications of a Thermal Advective Input

The data from INEL-1 clearly define the geochemical nature of thermal water that has equilibrated with hot rhyolite in one area of the ESRP. The fact that INEL-1's deep thermal water is > 35k years old (Mann, 1986) is consistent with the hypothesis that its Na-HCO₃ composition reflects prolonged reaction with felsic volcanic rocks. The existence of a substantial upward vertical hydraulic gradient between rhyolite and basalt in the areas of INEL-1 (ca. 0.05 - 0.1; Mann, 1986) implies that the hydraulic conductivity of rhyolite and/or mineralized basalts and sedimentary interbeds at the base of the ESRP aquifer must be quite low in order to explain such long residence times. This conjecture is corroborated by hydraulic conductivity measurements which indicate that K < 0.01 m/day in these rocks (Mann, 1986). Even so, Mann (1986) estimated that the flux of these thermal waters into the base of the ESRP aquifer is of the order of 2 x 10⁶ m³/year over the INL's area. If this proves to be typical of other thermally affected areas in the ESRP aquifer, then the magnitude of thermal recharge derived from the rhyolite could comprise a significant fraction of the ESRP aquifer's overall water budget.

4.2. Evidence for Thermal Inputs From Hot Rhyolites

It would be difficult to evaluate such an hypothesis where anthropogenic solutes play a major role, such as on the northwestern half of the INL. Rather, an area of the aquifer that is affected by thermal water inputs but not by anthropogenic disturbances is required. **Figure 13** shows all NWIS wells sampled between 2000 and 2012, together with a kriged interpolation of NWIS temperature data (unfiltered for depth) that are available for the ESRP. The data define a subdued thermal high that extends along the axis of the aquifer southwest of the INL for a distance of more than 80 km. This axial anomaly has persisted in wells sampled post-1995 and therefore is a real feature of the aquifer's thermal structure. Recent heat flow modeling of aquifer temperatures (C. Palmer, unpubl. report, 2015) suggests that this axial thermal feature may be an artifact of low ground water velocities in this area of the aquifer in response to an otherwise geographically uniform basal conductive heat flux.

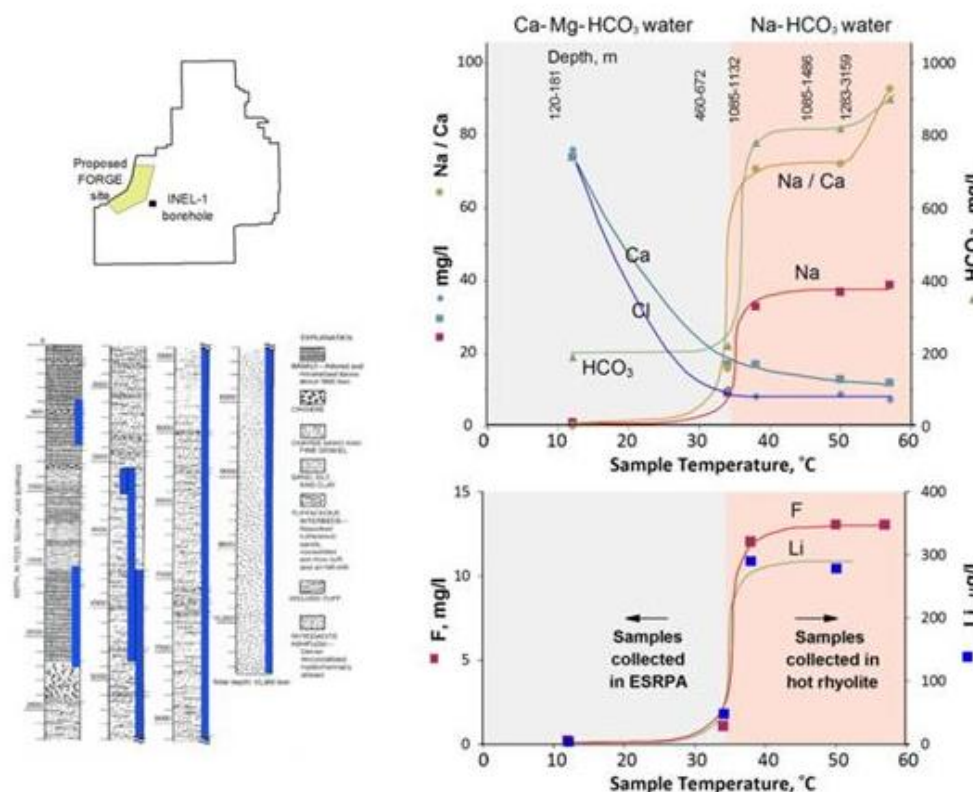


Figure 52: Comparison of thermal waters sampled in deep borehole INEL-1 drilled to 3.2 km in ESRP rhyodacite and welded tuff (Mann, 1986). Major-cation compositional shifts between the ESRP basalt aquifer ($\text{Ca}-\text{Mg}-\text{HCO}_3$ water type; $T \sim 12^\circ\text{C}$) and thermal waters in the rhyolitic rocks ($\text{Na}-\text{HCO}_3$ water type; $T > 30^\circ\text{C}$) are accompanied by a 300-fold increase in Na/Ca , a two-fold enrichment in dissolved silica and boron (not shown), and 60-fold enrichments in fluorine and lithium.

As shown in **Figure 14**, however, there are areas where ground water temperatures in excess of 14 °C reflect the input of heat and solute tracers that are characteristic of rhyolite-labeled thermal waters (after Olmsted, 1962; Busenberg et al., 2000, 2001; Fisher et al., 2012). Figure 14 summarizes previous work in this regard, showing locations of thermally affected waters beneath the INL as well as areas of anomalous trace solute concentrations that are indicative of rhyolite-labeled thermal waters. These patterns indicate that advective inputs of heat and solute occur in discrete areas of the ESRP where thermal waters enter through the aquifer's base and along its northern margin.

The zone of elevated temperatures along the aquifer's northern margin is heavily influenced by historic waste reprocessing and disposal activities, by dilution with tributary recharge from the highlands outside the aquifer (Olmsted, 1962; Fisher et al., 2012), and by thermal fluid inputs from the northern margin of the aquifer. In contrast, ground waters east of this zone are less diluted by tributary sources and have consistently higher Li, B, F, Na and SiO₂ concentrations. Two areas mapped by Busenberg et al. (2000; 2001) have dissolved He concentrations above air-saturation, which is further evidence for a rhyolitic basement source. The inference is that thermal waters such as those sampled by deep borehole INEL-1 (Figure 12) are injected through the ESRP aquifer's base in these areas.

In Figure 14, a local thermal anomaly identified by Busenberg et al. (2000; 2001) in the southeast corner of the INL has been extended on the basis of NWIS temperature data from additional wells to the southwest, suggesting that Busenberg's thermal anomaly may be part of a much larger axial thermal zone (Figure 13).

Figure 15 summarizes temperature and solute tracer behavior for wells within the axial thermal zone as well as upgradient of it, particularly in the area having enhanced levels of Li, B, F, Na and SiO₂ identified by Busenberg et al. (2000, 2001). As shown in the inset, the low signal/noise contrast in these waters precludes any identification of mixing behavior based on major-ion solutes such as Na and SiO₂. However, the axial thermal zone, as well as ground waters in Busenberg's anomaly (whose dissolved He concentrations are >3 times air-saturation), are characterized by elevated levels of Li and B, with a SiO₂ vs. Na/Ca correlation that is very similar to that observed in the ESRP aquifer adjacent to the Newdale thermal area (Figure 9) and which characterizes Newdale's high-temperature waters (Welhan, 2015).

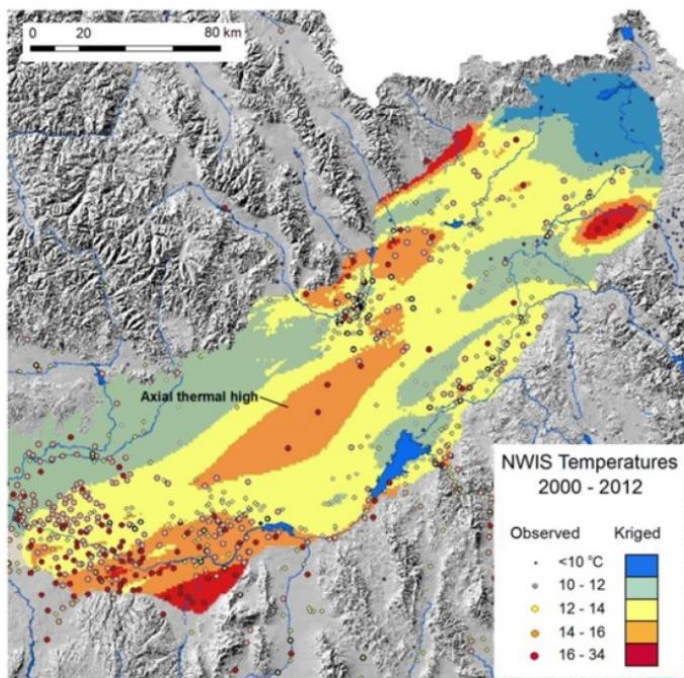


Figure 63: All NWIS temperature data from the period 2000 to 2012 overlain on regional temperature trends as interpolated by ordinary kriging.

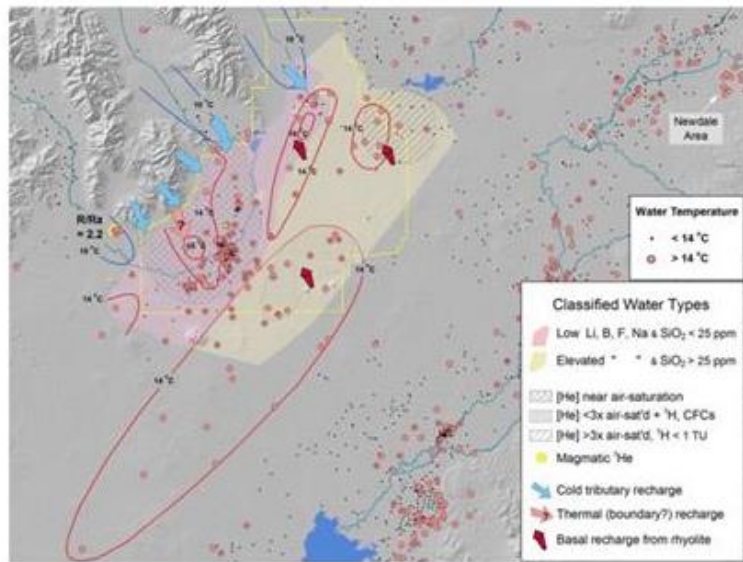


Figure 74: Summary of solute tracer patterns and areas of thermally affected ground waters on the INL, modified after Olmsted (1962), Busenberg et al. (2000; 2001) and Fisher et al. (2012), plotted together with all USGS NWIS data. Helium-isotope (R/Ra) data from Dobson et al. (2015). The area of thermally affected water identified by Busenberg et al. in the INL's southeast corner (stippled) has been extended to include the larger thermal anomaly that extends to the southwest, as indicated in Figure 13.

The pattern of elevated levels of diagnostic tracers in the axial thermal anomaly are summarized in Figure 15: of 24 wells in the axial thermal zone, 17 have $T > 14^{\circ}\text{C}$; 18 have Na above 15 mg/l; 20 have Na/Ca ratios > 0.7; and 11 have Li and $\text{B} > 10 \mu\text{g/l}$ and 20 $\mu\text{g/l}$, respectively. These solute enrichments appear to be confined to the area of this axial thermal anomaly and one identified by Busenberg in the east-central INL area (hatched, in Figure 14). However, well coverage in the intervening area is poor, so it is unclear whether these represent separate thermal anomalies or a larger, contiguous zone of elevated temperatures and tracer concentrations.

Nevertheless, the spatial pattern of solute enrichments that are diagnostic of rhyolite-labeled thermal water indicates that solute mass from the rhyolitic basement is being injected through the base of the aquifer at one or more locations in this area of the ESRP. The spatial distribution of these diagnostic tracers suggest two alternate hypotheses: (1) thermal waters are injected into the ESRP aquifer over a considerable geographic area within and upgradient of the INL; or (2) injection of thermal water and tracer mass is localized where preferential flowpaths exist in the rhyolitic rocks and intervening mineralized basalts that define the base of the ESRP aquifer.

4.3. Advective Heat Transfer

The results of heat transport modeling by Palmer (unpubl. rept., 2015), based on a purely conductive heat-transfer mechanism between the rhyolite and the ESRP aquifer, indicate that localized thermal anomalies in the central ESRPA (Figures 13 and 14) are the expression of low-transmissivity zones in the ESRP flow field. That is, aquifer temperatures are higher where ground water flow velocities are low and advective overprinting by shallow ground water flow of basal heat conduction is diminished. However, the model does not consider the implications of advective input of heat, nor can it be used to evaluate whether both conductive and advective heat-transfer processes are operative.

The large vertical hydraulic gradient observed in INEL-1 between the rhyolitic and basaltic flow systems (Mann, 1986) coupled with observations of openly flowing fractures and active thermal water flow in the rhyolite (Moos and Barton, 1990), indicates that a significant advective input of thermal water from the rhyolitic basement is not only possible but needs to be evaluated for a geohydrologic conceptual model.

Corroborating Mann's (1986) hypothesis that a significant advective flux of thermal water through the base of the ESRP aquifer would provide valuable information on the hydraulic connection between the rhyolite and the overlying aquifer as well as the manner in which heat is stored and transported out of the rhyolite. Stated another way, if dilution ratios between ambient ground water and thermal water can be inferred from temperature and/or trace element data, such information would provide an independent estimate of the rhyolite's hydraulic conductivity and the manner in which thermal waters enter the aquifer.

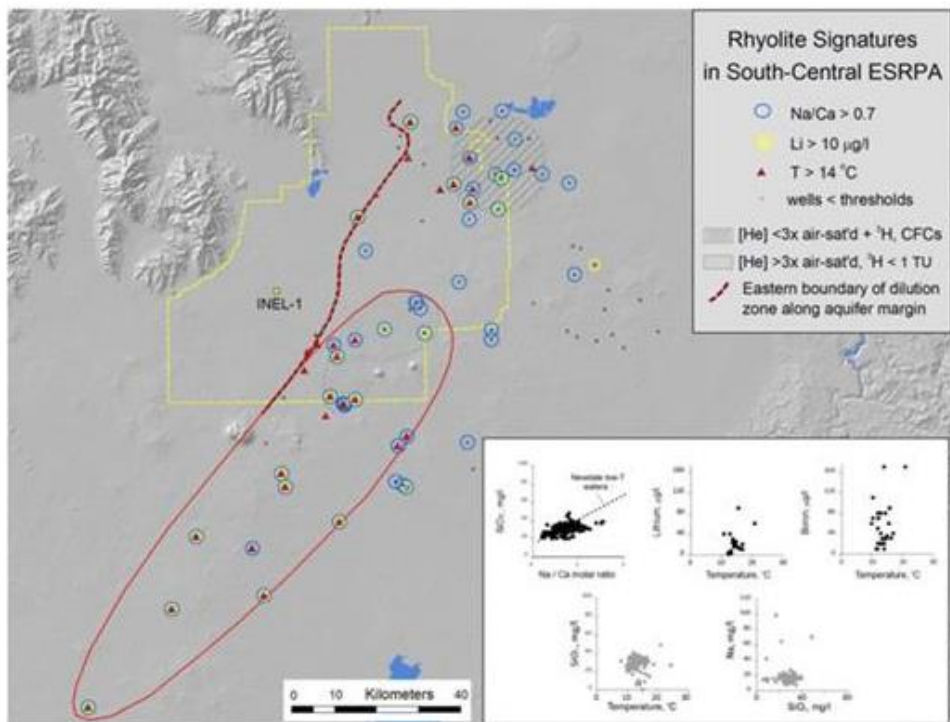


Figure 85: Solute tracer behavior in wells of the axial thermal zone and upgradient wells. The observed SiO₂ vs. Na/Ca correlation is very similar to that seen in the ESRP aquifer adjacent to the Newdale thermal area (Figure 9) and, together with elevated Li and B levels, confirms that rhyolite-labeled thermal water is being advected into the ESRP aquifer in this area.

A two-component mixing model was evaluated in the area of the axial thermal zone (Figure 14), assuming that the chemistry of ground water in the area of the axial thermal high only reflects mixing between regional ESRP ground water and thermal water discharging from the rhyolite.

The average water temperature in wells of the axial thermal zone is 14.9 °C ($2\sigma = 1.6^\circ$, $n = 54$). **Figure 16** shows all NWIS temperature and Cl data for these wells. In general, the pattern of Cl-temperature variations is reminiscent of that seen in the majority of INL monitoring wells (e.g., Figures 11B, 11C).

The end members in the two-component mixing analysis are: (1) thermal water issuing from the rhyolite beneath the axial thermal zone; (2) local shallow ground water immediately upgradient of the mixing zone; and (3) the composition of the mixture within the mixing zone. To simplify the analysis, mixing between components was assumed to be instantaneous and complete between the base of the aquifer and the sampling depth of each well.

4.3.1 Thermal End Member

Ostensibly, data from INEL-1 would seem to provide a reasonable constraint on the thermal component (Cl = 12 mg/l; Mann, 1986). However, recognizing that its chemical composition and temperatures could be spatially variable, depending on rock type, heat content and water-rock reaction temperature, and the Cl content of ground water that reacts at depth, the best estimate of the maximum Cl composition of thermal water entering the axial thermal zone is assumed to be the minimum Cl concentration shown in Figure 16: ca. 7.5 mg/l. Although lower than INEL-1, it is still well within the range observed in thermal waters that have interacted with felsic rocks in other areas of the SRP (Table 1) and is consistent with INL wells that exhibit mixing behavior with a low-Cl thermal component (e.g., Figure 11D).

The temperature of the thermal end member was defined by the depth to the base of the aquifer where the thermal water enters (ca. 100 m; Podgornay et al., 2013), and INEL-1's thermal gradient (40 °C/km; Mann, 1986), thereby constraining its temperature at 25 °C. Information from the nearby Kimama deep borehole (Freeman, 2013) was not considered relevant, because those waters have an unusual Na-Cl composition, and are non-representative of thermal fluids issuing from rhyolite in the INL area.

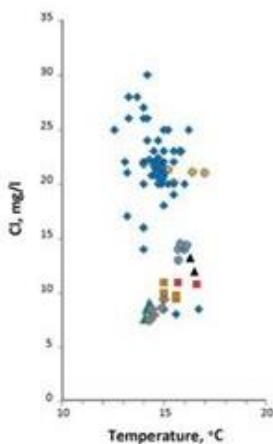


Figure 96: Available Cl-temperature data for wells that define the axial thermal zone south of INL (Figure 14). Data from individual wells are plotted with different symbols.

4.3.2 Non-thermal End Member

The nearest NWIS wells defining upgradient ground water conditions are more than 20 km from the axial thermal zone; more than 70 measurements from such wells within a distance of 60 km have a mean of $T = 11.6^\circ\text{C}$ ($2\sigma = 3.0$) and $\text{Cl} = 17.6 \text{ mg/l}$ ($2\sigma = 30.0$). Considering the distances involved and the large relative uncertainties in these averages, however, a better estimate of local ground water flowing through the axial thermal zone was derived from the 119 NWIS analyses of the two highest-Cl wells plotted in Figure 16 with a mean of $T = 14.7^\circ\text{C}$ ($2\sigma = 1.4$) and $\text{Cl} = 21.2 \text{ mg/l}$ ($2\sigma = 8.0$). These values are similar to, but somewhat higher than, those defined by the 70 upgradient wells and are considered the best available estimates of the non-thermal end member.

4.3.3 Mixed Water Composition

The thermal water issuing from the base of the aquifer is assumed to mix with ground water moving through the axial thermal zone, a mixture whose composition was estimated from the average of 27 measurements in the lowest-Cl wells shown in Figure 13: $T = 15.6^\circ\text{C}$ ($2\sigma = 1.5$) and $\text{Cl} = 10.3 \text{ mg/l}$ ($2\sigma = 6.0$). Note that the 60% relative uncertainty in this Cl estimate renders any mixing calculation highly uncertain.

With the above estimates in hand, the mixing fractions of the thermal and non-thermal end members can be determined using the following relationship (for temperature):

$$T_{\text{mix}} = f \cdot T_{\text{thermal}} + (1-f) \cdot T_{\text{non-thermal}} \quad (1)$$

where $T_{\text{mix}} = 15.6^\circ\text{C}$, $T_{\text{thermal}} = 25^\circ\text{C}$, $T_{\text{non-thermal}} = 14.7^\circ\text{C}$, and f is the mixing fraction of thermal water flux relative to the diluting flux of ESRP ground water, defined as $Q_{\text{thermal}}/(Q_{\text{thermal}} + Q_{\text{non-thermal}})$, where Q is the specific vertical Darcy flux (per m^2) defined by the hydraulic conductivity (K) and vertical gradient (I) within the rhyolitic rocks:

$$Q_{\text{thermal}} = K_{\text{rhyolite}} \cdot I_{\text{rhyolite}} \quad (2)$$

Solving for f in equation (1) yields an estimate of the mixing fraction based on temperature. In this case, $f = 0.087$; i.e., Q_{thermal} is an order of magnitude smaller than $Q_{\text{non-thermal}}$. In comparison, the flux ratio estimated using Cl data is unreasonably large, being almost an order of magnitude greater ($f = 0.82$). Given the large relative uncertainties in the estimated T and Cl end member values, such a discrepancy is not unexpected.

4.4. Inferred Hydraulic Conductivity of Rhyolite

Based on linear tracer velocities and porosities (0.05–0.2) for basalts in the vicinity of the axial thermal zone, Ackerman et al. (2006) estimated the specific Darcy flux in the aquifer, $Q_{\text{non-thermal}}$, to be in the range of 1.5 to 13 m/day. Mann (1986) estimated a vertical hydraulic gradient of 0.07 m/m in the upper part of INEL-1. Assuming the vertical gradient beneath the axial thermal zone is in the range of 0.05 to 0.1 m/m, then the flux ratio estimated via f in equation (1) and the specific Darcy flux in the ESRP aquifer allows K_{rhyolite} to be estimated using equation (2). The estimated range of K_{rhyolite} is therefore 1.5 to 25 m/day.

This estimate is orders of magnitude larger than the hydraulic conductivity reported for unfractured rhyolite in borehole INEL-1 (0.0005 to 0.01 m/day; Mann, 1986). The only way to reconcile these disparate results is to conclude that either (i) the flux ratio derived on the basis of temperatures is grossly inaccurate or (ii) the thermal flux into the aquifer is localized and focused along preferential flow paths

having a much higher effective hydraulic conductivity, such as in large fracture zones, zones of collapse breccias associated with buried caldera structures, and/or vertical heterogeneities along the feeder dikes of Big Southern Butte and nearby rhyolite domes.

Possibility (i) cannot be ruled out, because flux ratios < 0.01 apply to scenarios where $T_{\text{thermal}} \gg 25^\circ\text{C}$ and/or $T_{\text{non-thermal}}$ is very close to T_{mix} . Possibility (ii) could apply to either or both the fractured rhyolite and/or mineralized basalt that overlies the rhyolite and defines the base of the ESRP aquifer. The colored underlay in **Figure 17**, taken from Whitehead (1986), represents interpreted basalt thickness based on resistivity data; since basalt outcrops at or near the surface in this part of the ESRP, its thickness can be used as a first-order proxy for depth to rhyolite. Note that the axial thermal high in Figure 17 originates near where rhyolite appears to shallow to within 300-600 m of the surface before deepening rapidly to the northeast, south and southwest. This fact alone could facilitate the transport of thermal water into the shallow aquifer at this location.

The clustered nature of thermal occurrences on the ESRP (Figure 4), therefore, may be a reflection of thermal outflow from rhyolitic basement rocks along preferential flow paths associated with buried caldera collapse structures that are inferred to underlie the ESRP (Figure 1), and is also consistent with the highly fractured nature of rhyolitic rocks beneath the Snake River Plain that have been drilled. For example, Moos and Barton's (1990) analysis of INEL-1's high-resolution televiewer log confirmed that fracture density varies considerably in different depth zones, that large-aperture fractures exist in the rhyolite, and even though most fractures are sealed due to past hydrothermal deposition, open fractures do exist and are associated with elevated temperatures that indicate active flow of thermal water. Together with the inferences made from the mixing calculation, these facts suggest that thermal water, that is actively circulating within the rhyolite, makes its way into the ESRP aquifer only in certain areas, possibly where the rhyolite is shallowest and/or where local preferential flow paths channel thermal water into the shallow aquifer. This may explain the geographically localized nature of thermal ground water occurrences in the ESRP aquifer (Figure 4).

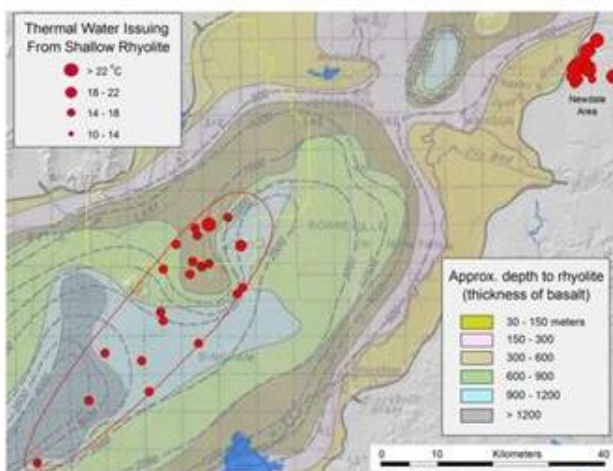


Figure 107: Wells that define the axial thermal zone in the vicinity of the southern INL. The colored underlay, taken from Whitehead (1986), represents interpreted basalt thickness based on resistivity data and deep control wells; it serves as a proxy for depth to rhyolite/mineralized basalt (contours are in feet).

5. GEOHYDROLOGIC CONCEPTUAL MODEL

The NWIS geochemical and temperature data examined in this study lead to some significant inferences and conclusions. **Figure 18**, adapted from McIing et al. (in press), depicts the current working hypothesis: the head of the axial thermal zone coincides with the area where the conductive gradient in altered basalts and underlying rhyolite shallows considerably, which is consistent with the inference based on Figure 17's basalt thickness / depth to the base of the aquifer. The figure also underscores the complex nature of the aquifer's northern margin where both thermal and non-thermal tributary inputs (including possible fault-controlled upwelling) and their corresponding geochemical signatures can complicate interpretations of mixing.

Figure 19 summarizes essential elements of the geohydrologic conceptual model, which incorporates the geochemical information and constraints identified in this work. The key elements of the model are:

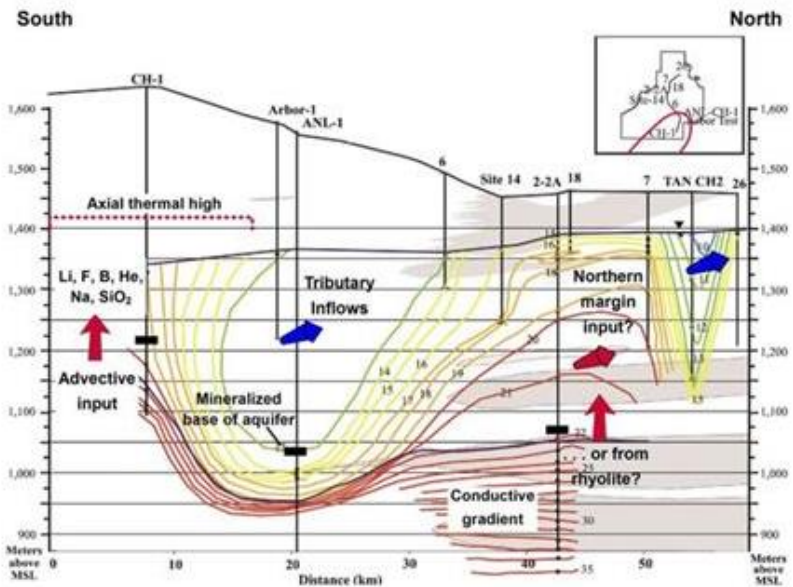


Figure 118: Cross section from north to south showing isotherms ($^{\circ}\text{C}$) in the ESRP aquifer beneath the INL, the base of the aquifer (mineralized basalt / rhyolite and the depth of conductively dominated heat flow), and inferred fluxes of thermal and non-thermal into the aquifer from its northern margin and from the underlying rhyolite. Red arrows represent, thermal water inputs through the base of the aquifer as well as possible fault-controlled upwelling along the aquifer's margin, and blue arrows represent cold ground water / surface water inflows from the ESRP's bounding highlands and tributary valleys. The position of the axial thermal anomaly of Figure 17 is indicated in the inset.

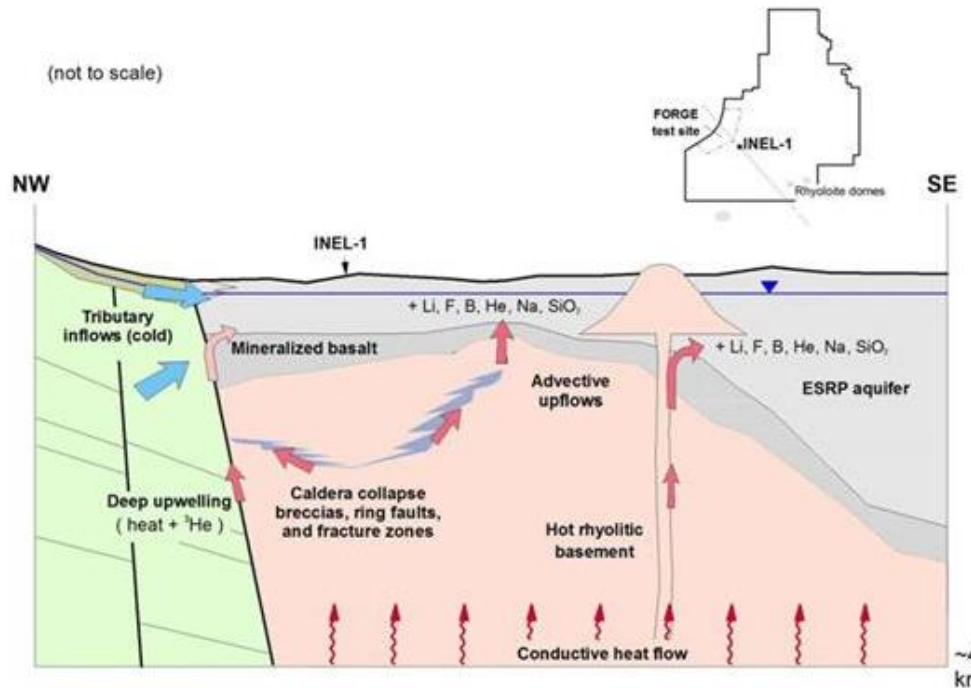


Figure 129: Conceptual model of ESRP geohydrology in the vicinity of the proposed FORGE test site, illustrating key elements controlling advective heat and solute inputs to the ESRP aquifer.

- Conductive heat flow raises aquifer water temperatures in low-velocity zones
- Heat and solute tracers from rhyolitic basement are injected into the aquifer's base
- Thermal and non-thermal advective inputs (heat + tracers) occur at the aquifer margin
- Preferential flow zones in the rhyolitic basement and the mineralized base of the aquifer focus these advective thermal inputs to the aquifer

Steady-state heat transport modeling indicates that ESRP aquifer temperatures are sensitive to the ground water velocity field (C. Palmer, per. comm., 2015). Assuming purely conductive heat transfer at the base of the active flow regime, elevated water temperatures are predicted a considerable distance above the base of the aquifer in areas where local ground water velocities are low. This builds on previous work (e.g., Brott et al., 1981; Blackwell, 1989) and confirms that conductive heat transfer exerts an important first-order control on the thermal state of the ESRP aquifer.

As Welhan (2015) has suggested, and the preceding analysis confirms, the association of elevated temperatures with the presence of certain major and trace elements in thermal ground waters of the ESRP is a characteristic feature of these waters. In particular, enrichments in Na, SiO₂, Li and B appear to be diagnostic of thermal water-rock reactions in the rhyolitic basement rocks and provides conclusive evidence that advective heat transport must be considered in any conceptual model of the deep EGS resource.

Work by Busenberg et al. (2000, 2001) has shown that these same elements, as well as dissolved He, are enriched in areas of the INL where above-ambient ground water temperatures are found, corroborating the hypothesis that rhyolite-labeled thermal waters are injected through the base of the aquifer in the area of the INL. Their work also suggests that thermal waters are injected into the aquifer at the aquifer's northern margin, perhaps along basin-bounding fault structures. Measurements by Dobson et al. (2014) of elevated $^{3}\text{He}/^{4}\text{He}$ ratios in a nearby thermal well corroborates the hypothesis that heat and solute mass from depth are injected along the aquifer margin. However, due to extensive dilution by tributary surface and ground waters in this area of the aquifer, it is not known whether these thermal waters also are enriched in rhyolite-derived solutes.

The most speculative element of the conceptual model portrayed in Figure 19 is the mechanism by which thermal water moves within the rhyolitic basement and makes its way to the overlying aquifer. The results of the two-component mixing model suggest that the axial thermal zone is supported by localized preferential flow. To date, the generation of permeable structures created by caldera collapse has focused on structures and lithofacies inferred from theoretical and experimental models (e.g., Branney, 1995; Cole et al., 2005) that have led to new insights into collapse mechanisms and resulting structures. Acocella (2008) proposed a four-stage, subsidence-controlled collapse sequence resulting in a series of nested calderas bounded by normal and reverse ring faults and intra-caldera collapse breccias. Together with permeable fault and fracture zones, these breccia facies may be particularly important in determining the geometry of preferential flow within the rhyolitic basement rocks.

6. IMPLICATIONS FOR EGS DEVELOPMENT

The scale of advective transport within the rhyolite basement is not known, but its existence raises the possibility that the thermal resource in the FORGE target zone may be significantly affected by hydrothermal heat transfer. Also, if preferential flow proves to be an important factor in this area and heterogeneous facies such as collapse breccias play a major role, then issues like rock strength, stress conditions and impacts on drilling and fracture stimulation in a highly fractured rock environment may need to be considered.

Finally, given the sharp contrast in chemical compositions of ESRP ground water and fluids that are expected to be encountered in the EGS target rocks, consideration should be given to the thermodynamic stability of the solute load in shallow ground water if it is used as the heat-transfer fluid. In addition, its potential to cause Ca-scaling problems due to CaCO₃ and CaF₂ must be evaluated and chemical necessary stabilization approaches identified.

7. CONCLUSIONS

Certain solutes found in anomalously warm ground waters of the ESRP aquifer are diagnostic of thermal water-rock reactions in rhyolitic / felsic rocks. Enrichments in Na, SiO₂, Li and B, in particular, are diagnostic indicators of the presence of rhyolite-labeled thermal water, as might high dissolved He concentrations (Busenberg, 2001) and diagnostic proportions of SiO₂ vs. Na/Ca, which appears to be a sensitive indicator even in highly dilute mixtures. The association of these tracer solutes with elevated ground water temperatures that occur in spatially discrete clusters throughout the ESRP conclusively demonstrates that heat transfer into the ESRP aquifer occurs not only via conduction but by advection of heat and solutes through its base and at its margins.

The failure of a simple two-component mixing model to independently confirm the magnitude of core-scale rhyolite hydraulic conductivity measurements in INEL-1 may simply reflect the low signal/noise contrast in thermally affected areas of the aquifer and uncertainty in the values of the end-member temperatures used in the mixing calculation. Significant spatial variability in the vertical hydraulic gradient and/or the magnitude of the lateral Darcy flux in the ESRP aquifer could also be responsible. On the other hand, it may indicate that considerable permeability heterogeneity exists and that preferential flow paths dominate advective transport in the rhyolites. This is supported by the observed association of thermal fluid flow in open fractures in INEL-1 (Moos and Barton, 1990), as well as more recent data on fracture geometry in deep boreholes drilled into rhyolite in other parts of the Snake River Plain (Shervais et al., 2013; Moody et al., in prep.), which indicate that open fractures and systematic changes in fracture density with depth will need to be considered in assessments of hydraulic conditions within the EGS resource.

ACKNOWLEDGEMENTS

I thank Rob Podgornay and Tom Wood for arranging INL-LDRD project funding and for their support of this work. Discussions with Mitch Plummer and Carl Palmer on their conductive heat flow modeling results proved very helpful in wrapping up this analysis, and Pat Dobson and Mike McCurry provided very helpful comments on helium and caldera collapse structures, respectively.

REFERENCES

- Ackerman, D.J., G.W. Rattray, J.P. Rousseau, L.C. Davis and B.R. Orr, 2006, A conceptual model of ground-water flow in the eastern Snake River Plain aquifer at the Idaho National Laboratory and vicinity with implications for contaminant transport; U.S. Geological Survey, Sci. Investigations Rept. 2006-5122, 62 pp.
- Acocella, V., 2008, Structural development of calderas: A synthesis from analogue experiments, Caldera Volcanism: Analysis, Modelling, and Response, p. 285-311.
- Arney, B.H., F. Goff and Harding-Lawson Associates, 1982, "Evaluation of the hot dry rock geothermal potential of an area near Mountain Home, Idaho," Los Alamos National Laboratory Report LA-9365-HDR, 65 pp.
- Bartholomay, R.C. and B. V. Twining, 2010, Chemical Constituents in Groundwater from Multiple Zones in the Eastern Snake River Plain Aquifer at the Idaho National Laboratory, Idaho, 2005-08; U.S. Geological Survey, Sci. Investigations Rept. 2010-5116, 82 pp.
- Berkeley Group, 1990, Boise geothermal aquifer study; Idaho Dept. of Water Resources, Final Report, DOE/ID/12748-3, 119 pp. plus appendices.
- Branney, M.J., 1995, Downsag and extension at calderas: new perspectives on collapse geometries from ice-melt, mining, and volcanic subsidence; *Bulletin of Volcanology*, v. 57, p. 303-318.
- Brott, A., D.D. Blackwell, and J.P. Ziagos, 1981, Thermal and tectonic Implications of heat flow in the eastern Snake River Plain: *Journal of Geophysical Research*, v. 86, p. 11,709-11,734.
- Busenberg, E., L.N. Plummer, M.W. Doughten, P.K. Widman and R.C. Bartholomay, 2000, Chemical and isotopic composition and gas concentrations of ground and surface water from selected sites at and near the Idaho National Engineering and Environmental Laboratory, Idaho, 1994 through 1997: U.S. Geological Survey Open-File Report 00-81 (DOE/ID-22164), 51 p.
- Christiansen, E.H., M.F. Sheridan and D.M. Burt, 1986, The Geology and Geochemistry of Cenozoic Topaz Rhyolites from the Western United States: *Geol. Soc. Am. Special Paper* 205, 82 pp.
- Cole, J.W., Milner, D.M., and Spinks, K.D., 2005, Calderas and caldera structures: A review; Earth-Science Reviews, vol. 69, p. 1-26.
- Druschel, G.K., 1998, Geothermal systems in the Idaho batholith: Geology and geochemistry; Washington State University, M.S. thesis, 183 pp.
- Dobson, P.F., B.M. Kennedy, M.E. Conrad, T. McLing, E. Mattson, T. Wood, C. Cannon, R. Spackman, M. van Soest and M. Robertson, 2015, *Proceedings*, 40th Workshop on Geothermal Reservoir Engineering, Stanford University, Stanford, California, SGP-TR-204, 7 pp.
- Fisher, J.C., J.P. Rousseau, R.C. Bartholomay and G.W. Rattray, 2012, A comparison of U.S. Geological Survey three-dimensional model estimates of groundwater source areas and velocities to independently derived estimates, Idaho National Laboratory and vicinity, Idaho; U.S. Geological Survey, Sci. Investigations Rept. 2012-5152, 130 pp.
- Ford M.T., 2005, The petrogenesis of Quaternary rhyolite domes in the bimodal Blackfoot Volcanic Field, southeastern Idaho: M.S. thesis, Idaho State University, 133 pp. plus one plate.
- Freeman, T.G., 2013, Evaluation of the geothermal potential of the Snake River Plain, Idaho, based on three exploration holes; Utah State University, M.S. thesis, 90 pp.
- Johnson, T. M., R.C. Roback, T.L. McLing, T.D. Bullen, D.J. DePaolo, C. Doughty, R.J. Hunt, R.W. Smith, L.D. Cecil and M.T. Murrell, 2000, Groundwater "fast paths" in the Snake River Plain aquifer: Radiogenic isotope ratios as natural groundwater tracers; *Geology*, v.28, p.871-874.
- Kagoshima, T., N. Takahata, J. Jung, H. Amakawa, H. Kumagai and Y. Sano, 2012, Estimation of sulfur, fluorine, chlorine and bromine fluxes at Mid-Ocean Ridges using a new experimental crushing and extraction method; *Geochem. Journal*, v.46, p.21-26.
- Krahmer, M.S., 1995, The geology and geochemistry of the geothermal system near Stanley, Idaho; Washington State University, M.S. thesis, 169 pp.
- Kuntz, M.A., H.R. Covington and L.J. Schorr, 1992, An overview of basaltic volcanism of the eastern Snake river Plain, Idaho; in P.K. Link, M.A. Kunz, and L.B. Platt (eds.), Regional Geology of Eastern Idaho and Western Wyoming, *Geol. Soc. America, Memoir* 179, p.227-267.
- Leeman, W.H., 1982, Rhyolites of the Snake River Plain-Yellowstone Plateau Province, Idaho and Wyoming: A summary of petrogenetic models; in B. Bonnichsen and R. Breckenridge (eds.), Cenozoic Geology of Idaho, p.203-212.
- Lewis, R.S., P.K. Link, L.R. Stanford and S.P. Long, 2012, Geologic map of Idaho: Idaho Geol. Survey Geologic Map 9, scale 1:750,000.

Welhan

- Lewis, R.S. and J.D. Kauffman, 2013, Selected radiometric and analytical data for the China Hat Dome area, NURE Project, southeastern Idaho: Idaho Geological Survey Digital Analytical Data Series DAD-9.
- Lewis, R.E. and H.W. Young, 1982, Thermal springs in the Payette River basin, west-central Idaho; U.S. Geological Survey, Water Resources Investigations Rept. 80-1020, 23 pp. plus plates.
- Mann, L.J., 1986, Hydraulic properties of rock units and chemical quality of water for INEL-I: A 10,365-foot deep test hole at the Idaho National Engineering Laboratory; U.S. Geological Survey, Water Resources Investigations Rept. 86-4020, 23 pp.
- Mayo, A.L., A.B. Muller and J.C. Mitchell, 1984, Geochemical and Isotopic Investigations of Thermal Water Occurrences of the Boise Front Area, Ada County, Idaho; Idaho Dept. of Water Resources, *Water Information Bull.* No. 30, Part 14, Geothermal Investigations in Idaho, 55 pp.
- McLing, T., McCurry, M., Cannon, C., Neupane, G., Wood, T., Podgorny, R., Welhan, J., Mines, G., Mattson, E., Wood, R., Palmer, C. and Smith, R., 2014, David Blackwell's Forty Years in the Idaho Desert, The Foundation for 21st Century Geothermal Research; Geothermal Resources Council *Transactions*, v.38, p.143-153.
- MIT, 2006, The Future of Geothermal Energy: Impact of Enhanced Geothermal Systems (EGS) on the United States in the 21st Century, Massachusetts Inst. Technology, Report INL/EXT-06-11746, 372 pp.
- Moody, A., J. Fairley and M. Plummer, in prep., Designing an engineered geothermal reservoir in the welded tuffs of the Snake River Plain; *Geol. Soc. America Special Paper*.
- Moos, D. and C.A. Barton, 1990, In-situ stress and natural fracturing at the INEL site, Idaho; a report to EG&G Idaho, Inc., EGG-NPR-10631.
- Morgan, L.A., and W.C. McIntosh, 2005, Timing and development of the Heise volcanic field, Snake River Plain, Idaho, western USA; *Geological Society of America Bulletin*, v. 117, p. 288.
- Morse, L.H. and M. McCurry, 2002, Genesis of alteration of Quaternary basalts within a portion of the eastern Snake River Plain Aquifer, in P.K. Link and L.L. Mink (eds.), Geology, hydrogeology, and environmental remediation: Idaho National Engineering and Environmental Laboratory, eastern Snake River Plain, Idaho, *Geological Society of America Special Paper* 353, p. 213-224.
- Podgorny, R., M. McCurry, T. Wood, T. McLing, A. Ghassemi, J. Welhan, G. Mines, M. Plummer, J. Moore, J. Fairley and R. Wood, 2013, Enhanced Geothermal System Potential for Sites on the Eastern Snake River Plain, Idaho; Geothermal Resources Council *Transactions*, v. 37, p. 191-197.
- Ramirez-Guzman, A., Y. Taran and M.A. Armienta, 2004, Geochemistry and origin of high-pH thermal springs in the Pacific coast of Guerrero, Mexico; *Geofisica Internacional*, v. 43, p. 415-425.
- Reed, M.H., and Spycher, N.F., 1984, Calculation of pH and mineral equilibria in hydrothermal water with application to geothermometry and studies of boiling and dilution; *Geochim. Cosmochim. Acta*, v.48, p.1479-1490.
- Ryan, J.G. and C.H. Langmuir, 1987, The systematics of lithium abundances in young volcanic rocks; *Geochim. Cosmochim. Acta*, v.51, p.1727-1741.
- Ryan, J.G. and C.H. Langmuir, 1993, The systematics of boron abundances in young volcanic rocks; *Geochim. Cosmochim. Acta*, v.57, p.1489-1498.
- Savov, I.P., W.P. Leeman, C.A. Lee and S.B. Shirey, 2009, Boron isotopic variations in NW USA rhyolites: Yellowstone, Snake River Plain, eastern Oregon; *J. Volcanology and Geothermal Research*, v. 188, p.162-172.
- Shervais, J.W., D.R. Schmitt, D.L. Nielson, J.P. Evans, E.H. Christiansen, L. Morgan, W.C.P. Shanks, T. Lachmar, L.M. Liberty, D.D. Blackwell, J.M. Glen, D. Champion, K.E. Potter and J.A. Kessler, 2013, First results from HOTSPOT: The Snake River Plain Scientific Drilling Project, Idaho, USA; *Scientific Drilling*, v. 15, p. 36-45.
- Smith, R.P., 2004, Geologic setting of the Snake River Plain aquifer and vadose zone; *Vadose Zone Journal*, v. 3, p. 47-58.
- Twining, B.V. and J.C. Fisher, 2015, Multilevel Groundwater Monitoring of Hydraulic Head and Temperature in the Eastern Snake River Plain Aquifer, Idaho National Laboratory, Idaho, 2011–13; U.S. Geological Survey, Sci. Investigations Rept. 2015-5042, 49 pp.
- Waag, C.J. and S.H. Wood, 1987, Evaluation of the Boise geothermal system; Idaho Dept. of Water Resources, Geothermal Investigations in Idaho, Final Report, 70 pp.
- Wedepohl, K.H. (ed.), 1974, Handbook of Geochemistry, Springer-Verlag Berlin.
- Welhan, J.A., 2012, Preliminary hydrogeologic analysis of the Mayfield area, Ada and Elmore Counties, Idaho; Idaho Geological Survey, Staff Report S-12-2, 41 pp.
- Welhan, J.A., 2015, Thermal and Trace-Element Anomalies in the Eastern Snake River Plain Aquifer: Toward a Conceptual Model of the EGS Resource; Geothermal Resources Council *Transactions*, v. 39, p. 363-375.
- White, D.E., 1967, Mercury and base-metal deposits with associated thermal and mineral waters; in H.I. Barnes (ed.), *Geochemistry of hydrothermal ore deposits*; Holt, Rinehart and Winston, NY, p. 575-631.

- Whitehead, R.L., 1986, Geohydrologic framework of the Snake river Plain, Idaho and eastern Oregon; U.S. Geological Survey, Hydrologic Investigations Atlas HA-681; three plates.
- Young, H.W., 1985, Geochemistry and hydrology of thermal springs in the Idaho batholith and adjacent areas, central Idaho; U.S. Geological Survey, Water Resources Investigations Report 85-4172, 44 pp.
- Youngs, S.W., 1981, Geology and geochemistry of the Running Springs geothermal area, southern Bitterroot lobe, Idaho batholith; Washington State University, M.S. thesis, 125 pp.

Appendix E

He Isotopic Evidence for Undiscovered Geothermal Systems in the Snake River Plain

PROCEEDINGS, Fortieth Workshop on Geothermal Reservoir Engineering
Stanford University, Stanford, California, January 26-28, 2015
SGP-TR-204

He Isotopic Evidence for Undiscovered Geothermal Systems in the Snake River Plain

Patrick F. Dobson¹, B. Mack Kennedy¹, Mark E. Conrad¹, Travis McLing², Earl Mattson², Thomas Wood³, Cody Cannon³, Ross Spackman⁴, Matthijs van Soest⁵, and Michelle Robertson¹

¹Earth Sciences Division, Lawrence Berkeley National Laboratory, Berkeley, CA

²Idaho National Laboratory, Idaho Falls, ID

³University of Idaho-Idaho Falls, Idaho Falls, ID

⁴Brigham Young University-Idaho, Rexburg, ID

⁵Arizona State University, Tempe, AZ

Corresponding author: pfdobson@lbl.gov

Keywords: He isotopes, Snake River Plain, geochemistry

ABSTRACT

The Snake River Plain is an area characterized by high heat flow and abundant Quaternary volcanism. While USGS assessments indicate that significant undiscovered geothermal resources are likely to be present in this region, no commercial geothermal development in this region has occurred. Elevated $^3\text{He}/^4\text{He}$ values reflect crustal input of mantle volatiles and may serve as a geochemical indicator of hidden geothermal systems that are masked by the presence of shallow cold water aquifers.

This study is part of an integrated geochemical investigation of thermal features in the central and eastern Snake River Plain region. Our project started by compiling existing He isotope data, regional heat flow data, and the locations of thermal wells and springs to develop compositional trends and identify new sampling opportunities where data gaps exist. Our initial field work has resulted in the highest $^3\text{He}/^4\text{He}$ measurements ever reported for the Snake River Plain, with three locations having Rc/Ra values greater than 2.0, suggesting that we can see through the effects of shallow cold water aquifers to indicate the presence of mantle-derived fluid and heat input into the shallow crust. Our new He isotopic results and previously reported data for the Snake River Plain range from 0.05 to 2.36 Rc/Ra . These results will be evaluated in conjunction with the results of conventional, isotopic, and multicomponent geothermometry studies.

1. INTRODUCTION

One of the key R&D challenges for the DOE Geothermal Technologies Office Hydrothermal program is to develop techniques that can be used to identify undiscovered geothermal resources in the US, which the USGS has estimated as having a mean power production potential of 30 GWe (Williams et al., 2008). One of the main areas with elevated heat flow in the US, the Snake River Plain (Figure 1), has no geothermal systems that have been commercially developed for energy generation. This area is characterized by abundant Quaternary volcanism associated with the migration of the Yellowstone hotspot, but in a large portion of this region there are shallow cold water aquifers that mask the presence of higher temperatures at depth.

Much of the volcanism in the Snake River Plain is associated with the migration of the Yellowstone hotspot (Pierce and Morgan, 2009), and consists of bimodal basalts and rhyolites that have been erupted over the past 17 Ma. The rhyolites were derived from a sequence of progressively younger to the east silicic volcanic centers (Morgan et al., 1984; Leeman et al., 2008). Voluminous basalt flows range in age from Tertiary to Holocene, and are found throughout both the Eastern and Western Snake River Plain. A small subset of these basalts are late Quaternary to Holocene in age, and form 8 distinct eruptive centers (Kuntz et al., 1992; Hughes et al., 2002), including the Craters of the Moon. A number of Quaternary rhyolitic domes and cryptodomes are located in the Eastern Snake River Plain – these are thought to have evolved from differentiation of basalt (McCurry et al., 2008).

While low enthalpy geothermal fluids have been harnessed for direct use in Idaho for more than a century, geothermal exploration activity in the Snake River Plain for high-enthalpy systems has been carried out sporadically over the past 50 years (Ross, 1970; Young and Mitchell, 1973; Parliman and Young, 1992), and has not yet resulted in the discovery and development of a commercial geothermal system in the area. One recent research study, Project Hotspot, drilled three deep (~2 km) wells in three different regions of the Snake River Plain (Nielson et al., 2012; Shervais et al., 2013). One of these wells (Kimama) intersected a thick (>900 m) cold water aquifer before encountering an elevated thermal gradient, while a second well (Kimberley) encountered a thick (~1500m) reservoir of 55-60°C water in rhyolitic lavas and tuffs. The third well (Mountain Home) discovered a high temperature (~150°C) geothermal system with artesian flow. None of these locations had any surface thermal features that could be used to predict the varying thermal conditions that were encountered.

With the exception of active rift zones (such as Iceland) and hot spots (Hawaii), basaltic dominated volcanic provinces are often neglected as possible hosts for productive geothermal systems (Nielson et al., 2015). This is in part due to the lack of shallow, long-

Dobson et al.

lived magma chambers that would provide a sustained source of heat to the shallow crust. However, as evidenced by the elevated heat flow, volcanic activity in the Snake River Plain region appears to be associated with magmatic intrusions in the crust that do provide a viable source of heat based on crustal models (Peng and Humphreys, 1998; DeNosaquo et al., 2009). McCurry and Welhan (2012), Nielson and Shervais (2014), and McLing et al. (2014) all postulate that basaltic sill complexes associated with these volcanic features could serve as the heat source for geothermal systems in the Snake River Plain region. However, such subsurface features are difficult to detect using standard exploration techniques. One possible way to detect such features is to use a tracer that would be present in geothermal fluids that would identify the presence of a magmatic component. Helium isotopes may serve as such a tracer for geothermal fluids in the Snake River Plain region.

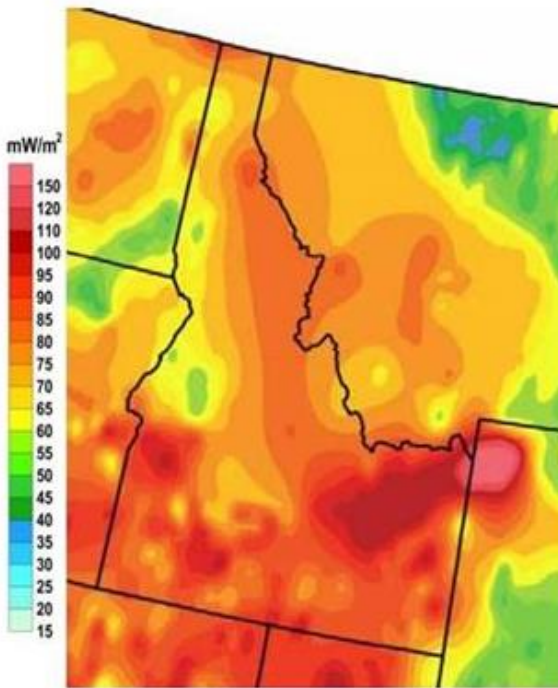


Figure 1: Heat flow map of Idaho and the surrounding region, showing elevated values in the Snake River Plain (Blackwell et al., 2011).

2. FIELD AND LABORATORY METHODS

Helium samples were collected during three field campaigns: September 2003, March 2014, and June 2014. Samples collected in 2014 were obtained from thermal springs and wells as part of a coordinated geochemical study of these features for multicomponent and isotopic geothermometry (McLing et al., 2014; Cannon et al., 2014). A type-K thermocouple was used to measure the temperature of the thermal features. Gas samples for noble gas analyses were collected from bubbling hot springs using an inverted plastic funnel that was connected with Tygon tubing to a copper tube. Gas was bubbled through the system to purge any atmospheric contamination, and the gas samples were then trapped in the copper tube using cold seal weld clamps, resulting in a gas sample volume of ~9.8 cm³. For water samples without a gas phase, water was collected in copper tubes to trap dissolved gases for analysis. The samples were then analyzed with a noble gas mass spectrometer at the Center for Isotope Geochemistry at LBNL using the methods described in Kennedy and van Soest (2006). Helium isotopic compositions have been corrected for air contamination (Rc) using the He/Ar and Ne/Ar ratios by assuming all of the Ne and Ar were derived from air or air saturated water.

3. RESULTS

There are very few published He isotope values for thermal waters in the Snake River Plain region. Welhan et al. (1988) reported He isotope values ranging from 0.14 to 0.51 R/Ra for four thermal springs in the Snake River Plain region. A more comprehensive unpublished study of He isotopic variations for 19 thermal springs and wells in southern Idaho was conducted by Jenkins (1979); he reported R/Ra values ranging from 0.1 to 1.56, with all but two samples having values less than 1.

The initial results of this study provide He isotope data from a wide range of thermal springs and wells in the Snake River Plain and neighboring areas. A total of 11 He samples were collected during the 2003 field season, and an additional 21 He samples were

collected in 2014. Three of the areas that were sampled in 2003 were resampled in 2014 as a check on the reproducibility of the analyses. In all cases, the Rc/Ra values for the resampled features are within 0.2 Rc/Ra of each other.

He isotope values for the features sampled thus far in this study range from a low of 0.05 Rc/Ra (for Lidy Hot Springs) up to a high value of 2.36 for the Barron's (Camas Creek Ranch) well (Figures 2 & 3). A total of eight features had Rc/Ra values greater than 1.5, with three of these having values greater than 2. The elevated ($Rc/Ra > 1.5$) values cluster in three distinct regions: one near Craters of the Moon (Green House well), a second in the Twin Falls area (Miracle HS, Banbury HS and well, and Sligers well), and a third located on the northern margin of the Snake River Plain north of Twin Falls (White Arrow HS, Magic Reservoir HS well, and Barron's well).

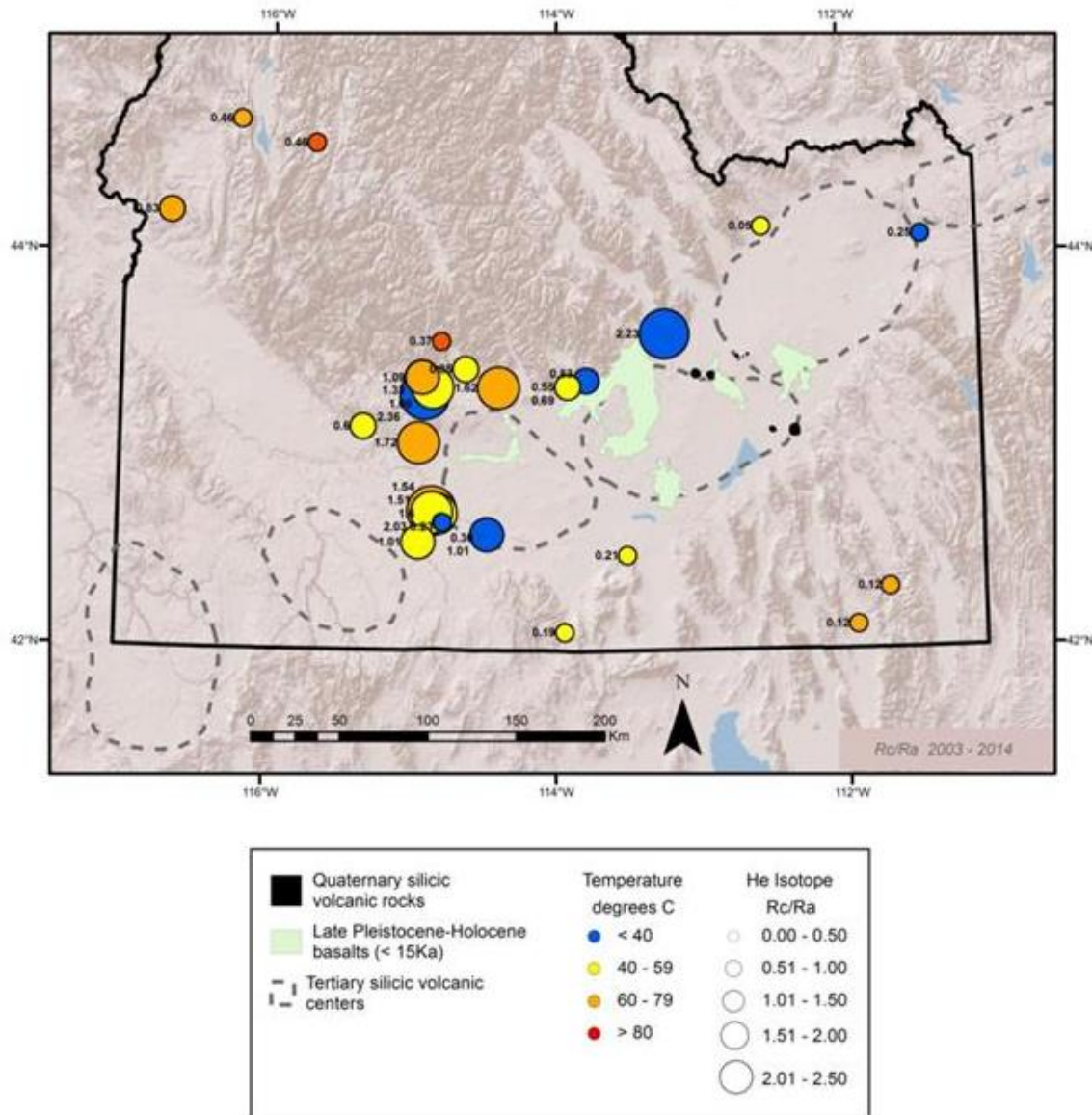


Figure 2: He isotopic values for the Snake River Plain superimposed on a digital elevation map with locations of latest Pleistocene-Holocene basalts (Kuntz et al., 1992; Hughes et al., 2002), Quaternary rhyolites (McCurry et al., 2008), and the outlines of major Tertiary silicic volcanic centers (Leeman et al., 2008). Symbol size and number indicates Rc/Ra He value, and symbol color indicates the measured surface temperature of spring or well.

Dobson et al.

4. DISCUSSION

Helium isotopes can be used to identify the source of the helium (Ballentine et al., 2002; Graham, 2002), thus facilitating its use as a tracer for the origin of geothermal fluids. There are three major reservoirs of helium: the mantle, the crust, and the atmosphere. The $^{3}\text{He}/^{4}\text{He}$ ratio of air is 1.4×10^{-6} , and is defined as Ra. Mantle (magmatic) He values are typically enriched in ^{3}He , with $^{3}\text{He}/^{4}\text{He}$ ratios 7 to 9 times that of atmosphere (7-9 R/Ra). Because ^{4}He is produced by radiogenic decay of Th and U, crustal He ratios are typically ~ 0.02 R/Ra.

Kennedy and van Soest (2007) conducted a detailed study of He isotopic compositions of thermal features across the Basin and Range. They observed that fluids from geothermal systems located on the western margin of the Great Basin that were associated with a volcanic heat source had elevated $^{3}\text{He}/^{4}\text{He}$ values ($\text{Rc/Ra} > 3$). In contrast, amagmatic geothermal systems in the Basin and Range Province had significantly lower values (Rc/Ra from ~ 0.2 to 2); however, these values are considerably above crustal values (~ 0.02). They interpreted the slightly elevated values for the nonvolcanic systems to reflect amagmatic flow of mantle fluids through the ductile lower crust. The values increased systematically from east to west, correlating with an east-west increase in crustal strain rate suggesting a concurrent east-west increase in deep crustal permeability, enhancing fluid flow to the surface. Several regions were found to have anomalously high R/Ra values with respect to the general trend. Siler et al. (2014) looked to correlate the occurrence of major structural features in these regions to see if they might serve as localized zones of higher permeability that would further facilitate deep crustal circulation of fluids and heat.

While the Snake River Plain has a clear association with young volcanism (Figure 2), the thermal effects of this magmatic activity in the shallow crust are often masked by a thick cold water aquifer that overlies much of the Eastern Snake River Plain region (McLing et al., 2014). This cold water aquifer has a thickness reaching up to more than 900 m in places (Nielson et al., 2012; Shervais et al., 2013). Another challenge is that most of the thermal features encountered in the Snake River Plain are located along its margins. Fluids sampled from these features may have undergone cooling and mixing, thus making interpretation of fluid geothermometry challenging. Multicomponent geothermometry has been employed to better constrain the source temperatures of these complex fluids (Neupane et al., 2014; Cannon et al., 2014).

During the preliminary phase of this project, we examined the three regions with elevated He isotopic ratios to see if they coincide with areas that have evidence of young volcanism (Figure 2) or high heat flow (Figure 3). Only one of the areas (Green House well – $\text{Rc/Ra} = 2.23$, by Areo) is near young (< 15 Ka) volcanic rocks (Craters of the Moon). This well is quite unremarkable in terms of its flowing temperature (36.3°C), and multicomponent geothermometry yields a source temperature estimate of only $67 \pm 15^\circ\text{C}$ (Cannon et al., 2014). The other two high He isotope clusters (the Twin Falls area and the area near Magic Reservoir HS) are in areas with Miocene rhyolites and Plio-Pleistocene basalts (Leeman et al., 1982; Whitehead, 1992; Ellis et al., 2010) but are generally associated with higher temperature thermal features and/or wells. These clusters are located in areas with high heat flow (Figure 3).

One area that warrants future study is the region around Mountain Home, where drilling has revealed the existence of a hidden 150°C geothermal reservoir (Shervais et al., 2013). Unfortunately this well was plugged and abandoned before it could be sampled for He isotopes, but other wells in the region might contain geochemical signatures related to this system. While this area does not have Holocene volcanism, it does host Quaternary basalts (Shervais et al., 2002) and may be underlain by younger basaltic sills (Nielson and Shervais, 2014).

4. CONCLUSIONS

New helium isotope data for thermal waters in the Snake River Plain has revealed a number of elevated ($\text{Rc/Ra} > 1.5$) He isotope values that are higher than previously reported data for this region. These values suggest a significant mantle helium component. These elevated values have been observed thus far in three different areas within the Snake River Plain. There is not a clear correlation between these elevated $^{3}\text{He}/^{4}\text{He}$ values and young (< 15 Ka) volcanic features. However, this He signature may be related to basaltic intrusions that are thought to sustain the high heat flow in this region. Future work will include integration of the He data with isotope and multicomponent geothermometry and collection of additional samples in areas such as Mountain Home, where a hidden geothermal system has been discovered. Such sampling will help test whether He isotopes can help identify systems that have no surface manifestations in the Snake River Plain region.

ACKNOWLEDGMENTS

This work was conducted with funding by the Assistant Secretary for Energy Efficiency and Renewable Energy, Geothermal Technologies Program, of the U.S. Department under the U.S. Department of Energy Contract No. DE-AC02-05CH11231 with Lawrence Berkeley National Laboratory. We thank Will Smith, Hari Neupane, Wade Worthing, and Steven Levesque for their assistance in the field, and to the many property owners in Idaho who graciously allowed us access to the springs and wells on their land. We also thank Colin Williams (USGS) for sharing his heat flow maps with our team.

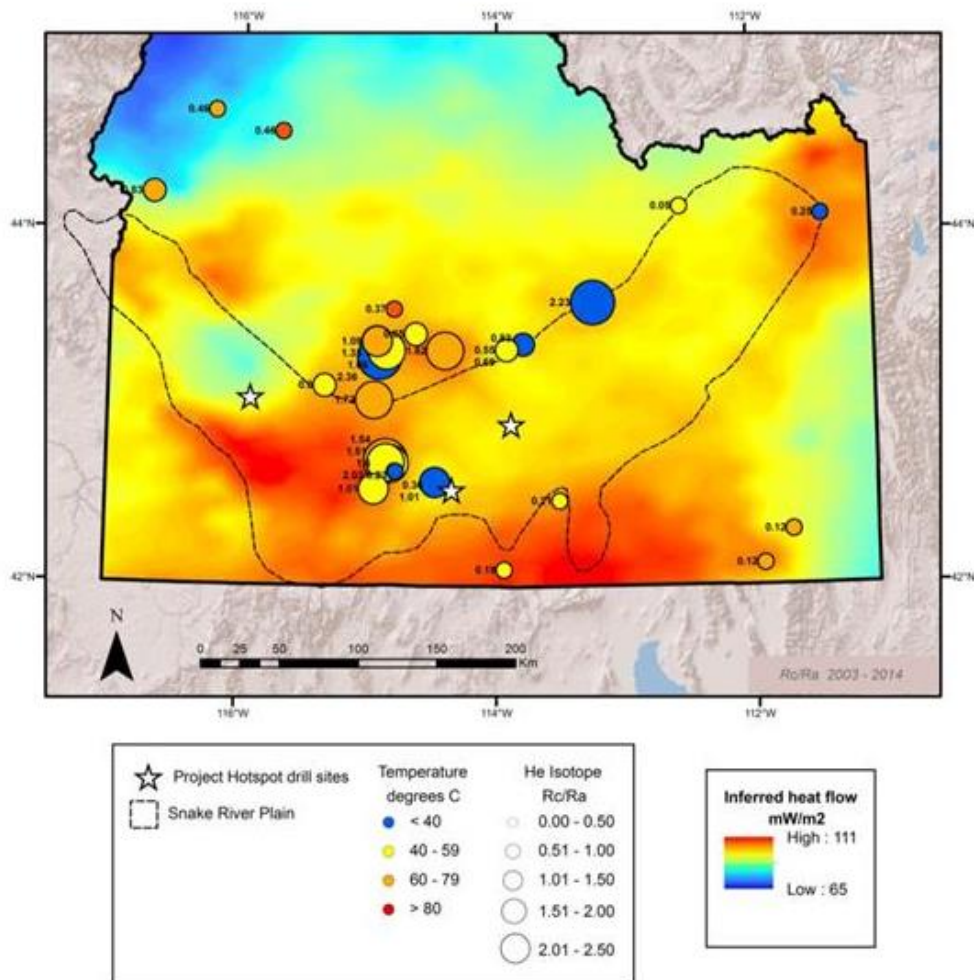


Figure 3: He isotopic values for the Snake River Plain superimposed on USGS heat flow map of the Snake River Plain (Williams and DeAngelo, 2011). Map depicts inferred heat flow below the groundwater flow system. Map was generated to identify regional-scale variations, so high heat flow in geothermal regions was capped at 120 mW/m². Outline of the Snake River Plain province from Payne et al. (2012). Symbol size and number indicates Rc/Ra He value, and symbol color indicates measured surface temperature of spring or well. The three Project Hotspot wells, depicted as stars, are (from west to east) Mountain Home, Kimberly, and Kimama (Shervais et al., 2013).

REFERENCES

- Ballentine, C.J., Burgess, R., and Marty, B.: Tracing Fluid Origin, Transport and Interaction in the Crust, in Porcelli, D., Ballentine, C.J., and Wieler, R., eds., Reviews in Mineralogy & Geochemistry—Noble Gases in Geochemistry and Cosmochemistry: Washington, D.C., Mineralogical Society of America, v. 47, (2002), 539–614.
- Blackwell, D.D., Richards, M.C., Frone, Z.S., Batir, J.F., Williams, M.A., Ruzo, A.A., and Dingwall, R.K.: SMU Geothermal Laboratory Heat Flow Map of the Conterminous United States, 2011, (2011), Available at <http://www.smu.edu/geothermal>
- Cannon, C., Wood, T., Neupane, G., McLing, T., Mattson, E., Dobson, P., and Conrad, M.: Geochemistry Sampling for Traditional and Multicomponent Equilibrium Geothermometry in Southeast Idaho, *Geothermal Resources Council Transactions*, **38**, (2014), 425–431.
- DeNosaquo, K.R., Smith, R.B. and Lowry, A.R.: Density and Lithospheric Strength Models of the Yellowstone-Snake River Plain Volcanic System from Gravity and Heat Flow Data. *Journal of Volcanology and Geothermal Research*, **188**, (2009), 108–127.

Dobson et al.

- Ellis, B.S., Barry, T., Branney, M.J., Wolff, J.A., Bindeman, I., Wilson, R. and Bonnichsen, B.: Petrologic constraints on the development of a large-volume, high temperature, silicic magma system: The Twin Falls eruptive centre, central Snake River Plain. *Lithos*, **120**, (2010), 475–489.
- Graham, D.W.: Noble Gas Isotope Geochemistry of Mid-Ocean Ridge and Ocean Island Basalts: Characterization of Mantle Source Reservoirs, in Porcelli, D., Ballentine, C.J., and Wieler, R., eds., *Reviews in Mineralogy & Geochemistry—Noble Gases in Geochemistry and Cosmochemistry*: Washington, D.C., Mineralogical Society of America, v. 47, (2002), 481–538.
- Hughes, S.S., Wetmore, P.H. and Casper, J.L.: Evolution of Quaternary Tholeiitic Basalt Eruptive Centers on the Eastern Snake River Plain, Idaho. In B. Bonnichsen, C.M. White, and M. McCurry, eds., *Tectonic and Magmatic Evolution of the Snake River Plain Volcanic Province*, Idaho Geological Survey Bulletin **30**, (2002), 23 p.
- Jenkins, W.J.: Mapping of Volcanic and Conducted Heat Flow Sources for Thermal Springs in the Western United States Using Helium Isotopes and other Rare Gases. U.S. Geological Survey unpublished report, (1979). Data reported in Kennedy and van Soest (2007) supplemental materials (www.sciedemag.org/cgi/content/full/318/5855/1433/DC1)
- Kennedy, B.M., and van Soest, M.C.: Flow of Mantle Fluids through the Ductile Lower Crust: Helium Isotope Trends. *Science*, **318**, (2007), 1433–1436.
- Kuntz, M.A., Covington, H.R., and Schorr, L.J.: Chapter 12 – An Overview of Basaltic Volcanism of the Eastern Snake River Plain, Idaho. In Link, P.K., Kuntz, M.A., and Platt, L.B., eds., *Regional Geology of Eastern Idaho and Western Wyoming*, *Geological Society of America Memoir* **179**, (1992), 227–267.
- Leeman, W.P.: Geology of the Magic Reservoir Area, Snake River Plain, Idaho. In B. Bonnichsen and R.M. Breckenridge, eds., *Cenozoic Geology of Idaho*, Idaho Bureau of Mines and Geology Bulletin **26**, (1982), 369–376.
- Leeman, W.P., Annen, C. and Dufek, J.: Snake River Plain – Yellowstone Silicic Volcanism: Implications for Magma Genesis and Magma Fluxes. In Annen, C. and Zellmer, G. F. (eds) *Dynamics of Crustal Magma Transfer, Storage and Differentiation*. Geological Society, London, Special Publications, **304**, (2008), 235–259.
- McCurry, M., Hayden, K.P., Morse, L.H. and Mertzman, S.: Genesis of Post-Hotspot, A-Type Rhyolite of the Eastern Snake River Plain Volcanic Field by Extreme Fractional Crystallization of Olivine Tholeiite. *Bulletin of Volcanology* **70**, (2008), 361–383.
- McCurry, M. and Welhan, J.: Do Magmatic-Related Geothermal Energy Resources Exist in Southeast Idaho? *Geothermal Resources Council Transactions*, **36**, (2012), 699–707.
- McLing, T., McCurry, M., Cannon, C., Neupane, G., Wood, T., Podgorny, R., Welhan, J., Mines, G., Mattson, E., Wood, R., Palmer, C. and Smith, R.: David Blackwell's Forty Years in the Idaho Desert, The Foundation for 21st Century Geothermal Research. *Geothermal Resources Council Transactions*, **38**, (2014), 143–153.
- Neupane, G., Mattson, E.D., McLing, T.L., Palmer, C.D., Smith, R.W. and Wood, T.R.: Deep Geothermal Reservoir Temperatures in the Eastern Snake River Plain, Idaho using Multicomponent Geothermometry, *Proceedings*, 39th Workshop on Geothermal Reservoir Engineering, Stanford University, Stanford, CA, (2014), 12 p.
- Nielson, D.L., Delahunty, C. and Shervais, J.W.: Geothermal systems in the Snake River Plain, Idaho, Characterized by the Hotspot Project. *Geothermal Resources Council Transactions*, **36**, (2012), 727–730.
- Nielson, D.L., and Shervais, J.W.: Conceptual Model for Snake River Plain Geothermal Systems, *Proceedings*, 39th Workshop on Geothermal Reservoir Engineering, Stanford University, Stanford, CA, (2014), 7 p.
- Nielson, D.L., Shervais, J., Evans, J., Liberty, L., Garg, S.K., Glen, J., Visser, C., Dobson, P., Gasperikova, E., and Sonnenthal, E.: Geothermal Play Fairway Analysis of the Snake River Plain, Idaho, *Proceedings*, 40th Workshop on Geothermal Reservoir Engineering, Stanford University, Stanford, CA, (2015), 9 p.
- Parlman, D.J. and Young H.W.: Compilation of Selected Data for Thermal-Water Wells and Springs in Idaho, 1921 through 1991. *U.S. Geological Survey Open-File Report 92-175*, (1992), 201 p.
- Payne, S.J., McCaffrey, R., King R.W., and Kattenhorn, S.A.: A New Interpretation of Deformation Rates in the Snake River Plain and Adjacent Basin and Range Regions Based on GPS Measurements. *Geophysical Journal International*, **189**, (2012), 101–122.
- Peng, X. and Humphreys, E.D.: Crustal Velocity Structure across the Eastern Snake River Plain and the Yellowstone Swell. *Journal of Geophysical Research, B, Solid Earth and Planets*, **103**(4), (1998), 7171–7186.
- Pierce, K.L. and Morgan, L.A.: Is the Track of the Yellowstone hotspot Driven by a Deep Mantle Plume? – Review of Volcanism, Faulting, and Uplift in Light of New Data. *Journal of Volcanology and Geothermal Research*, **188**, (2009), 1–25.
- Ross, S.H.: Geothermal Potential of Idaho. *Geothermics*, Special Issue **2**, v. 2, part 2, (1970), 975–1008.
- Shervais, J.W., Schmidt, D.R., Nielson, D., Evans, J.P., Christiansen, E.H., Morgan, L., Shanks, W.C.P., Prokopenko, A.A., Lachmar, T., Liberty, L.M., Blackwell, D.D., Glen, J.M., Champion, D., Potter, K.E. and Kessler, J.A.: First Results from HOTSPOT: The Snake River Plain Scientific Drilling Project, Idaho, U.S.A., *Scientific Drilling*, **15**, (2013), 36–45.
- Shervais, J.W., Shroff, G., Vetter, S.K., Mathews, S., Hanan B.B., and McGee, J.J.: Origin and Evolution of the Western Snake River Plain: Implications from Stratigraphy, Faulting, and the Geochemistry of Basalts near Mountain Home, Idaho. In B. Bonnichsen,

Dobson et al.

- C.M. White, and M. McCurry, eds., Tectonic and Magmatic Evolution of the Snake River Plain Volcanic Province: Idaho Geological Survey Bulletin **30**, (2002), 343–361.
- Siler, D.L., Kennedy, B.M. and Wannamaker, P.E.: Regional Crustal Discontinuities as Guides for Geothermal Exploration, *Geothermal Resources Council Transactions*, **38**, (2014), 39–47.
- Welhan, J.A., Poreda, R.J., Rison, W., and Craig, H.: Helium Isotopes in Geothermal and Volcanic Gases of the Western United States, I. Regional Variability and Magmatic Origin, *Journal of Volcanology and Geothermal Research*, **34**, (1988), 185–199.
- Whitehead, R.L.: Geohydrologic Framework of the Snake River Plain Regional Aquifer System, Idaho and Eastern Oregon, *U.S. Geological Survey Professional Paper 1408-B*, (1992), 32 p.
- Williams, C.F., and DeAngelo, J.: Evaluation of Approaches and Associated Uncertainties in the Estimation of Temperatures in the Upper Crust of the Western United States, *Geothermal Resources Council Transactions*, **35**, (2011), 1599–1605.
- Williams, C.F., Reed, M.J., Mariner, R.H., DeAngelo, J. and Galanis, S.P., Jr.: Assessment of Moderate- and High-Temperature Geothermal Resources of the United States, *U.S. Geological Survey Fact Sheet 2008-3082*, (2008), 4 p.
- Young, H.W. and Mitchell, J.C.: Geothermal Investigations in Idaho Part 1: Geochemistry and Geologic Setting of Selected Thermal Waters. Idaho Department of Water Administration, Water Information Bulletin **30**, (1973), 43 p.

Appendix F

Geomechanical Characterization of Core from the Proposed FORGE Laboratory on the Eastern Snake River Plain, Idaho

Geomechanical Characterization of Core from the Proposed FORGE Laboratory on the Eastern Snake River Plain, Idaho

Rohit Bakshi, Mostafa Eskandari Halvaci, Ahmad Ghassemi

1314 Sarkeys Energy center
Boyd St. Norman, Oklahoma - 73069
E-mail:Ahmad.Ghassemi@ou.edu

Keywords: Acoustic emission, MEQ, Geomechanics, Tuff, Rhyolite, Rhyodacite, Snake River FORGE

ABSTRACT

This paper presents the results of a geomechanical characterization of cores from a well in the Eastern Snake River Plain, Idaho, near a proposed FORGE EGS Laboratory. The geological and geothermics features of the area make the Eastern Snake River Plain a promising target for an EGS system. The cores tested were obtained from the INEL-1 well with core depths ranging from 1,558 - 3,160 m. According to previous geological studies, rock types present in this well are mainly rhyolitic tuffs, rhyodacites, basalts and lava deposits (Miller et al.). The section of core tested is mainly rhyolitic tuff or rhyodacites. These rocks are hydrothermally altered in places and are found to have varying permeability, depending upon the stress level and existence of natural fractures. The core segments from one well were plugged to obtain one inch diameter and two inch long specimens for geomechanical characterization including porosity, permeability, velocity data, elastic modulus, Poisson's ratio, tensile strength, and Mohr-Coulomb envelope as well as some acoustic emissions during triaxial tests. Pore scale characterization was also performed using thin section and Scanning electron microscope (SEM) imaging.

1. INTRODUCTION

Enhanced geothermal systems are expected to be a significant source of energy generation in the years to come. One of the most promising sites for this in the US is the Snake river geothermal Consortium's (SRGC) proposed located within Idaho National Laboratories' Geothermal Resource Research Area (GRRA), which is located along the Snake River Plain in south eastern Idaho. The presence of high underground heat flow and a large underground aquifer within the Snake River Plain makes it ideal for a geothermal energy development (Williams et. al).

EGS development relies on creation of conductive pathways for fluid flow and heat exchange. Low primary reservoir rock permeability requires hydraulic fracturing with shear and tensile fractures depending on the specific site characteristics. For a successful stimulation as well as drilling programs, geomechanical properties of the target rocks are needed. Two core sections form depths of 4874 ft and 10,365 ft, each about 4 to 6 inches, were provided by INEL. Plugs were extracted from these cores to obtain suitable samples for geomechanical testing. Mineral composition and pore scale characterization has been performed using SEM and thin sections. A variety of laboratory tests have been conducted on the plugs to determine rock strength (triaxial and uniaxial), velocity data (shear and compressional), elastic properties, acoustic emissions analysis, stress-dependent porosity and permeability, crushed porosity (low pressure pycnometer porosity).

2. MINERALOGICAL AND PETROLOGIC DESCRIPTION OF THE CORE SAMPLES

2.1 Mineralogy of the INEL Core

One inch plugs from each of the two cores were tested using Fourier transform infrared spectroscopy (FTIR). The following table shows the mineral composition of the two samples.

Spectrum Mineral	4874ft core plug (% composition)	10,365 ft core plug (% composition)
Quartz	25.55	23.13
Orthoclase Feldspar	25.48	10.87
Oligoclase Feldspar	16.25	10.06
Albite	6.07	21.30
Illite	16.78	2.85
Calcite	0.00	6.83

Bakshi, Halvaei and Ghassemi

Dolomite	1.33	4.60
Smectite	4.21	3.04
Kaolinite	1.04	0.09
Mixed Clays	0.88	13.50
Siderite	2.38	2.98

Table 1: Mineral composition in the INEL-1 core plugs using FTIR

Feldspars (Orthoclase, Oligoclase and Albite) constitute 42-27% of the composition here followed by silica (quartz) at 24-27%.

2.2 Petrology of INEL core

Two petrographic thin section images were prepared for the two cores (from depths 4874 ft and 10365 ft respectively). The rocks have an aphanitic texture with a few interspersed large grains of sizes 1-4 mm. The core from 4874 ft is lighter in colour.

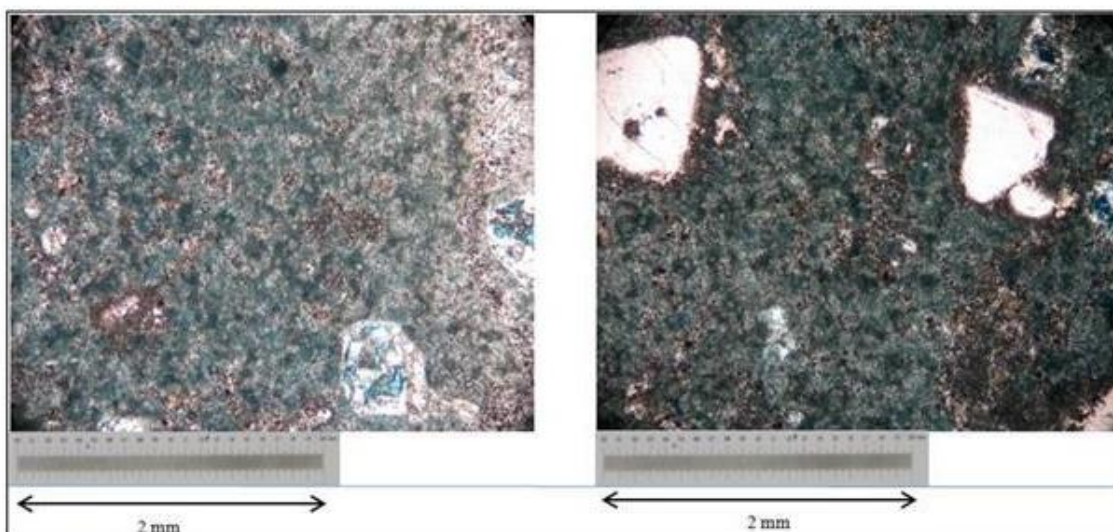
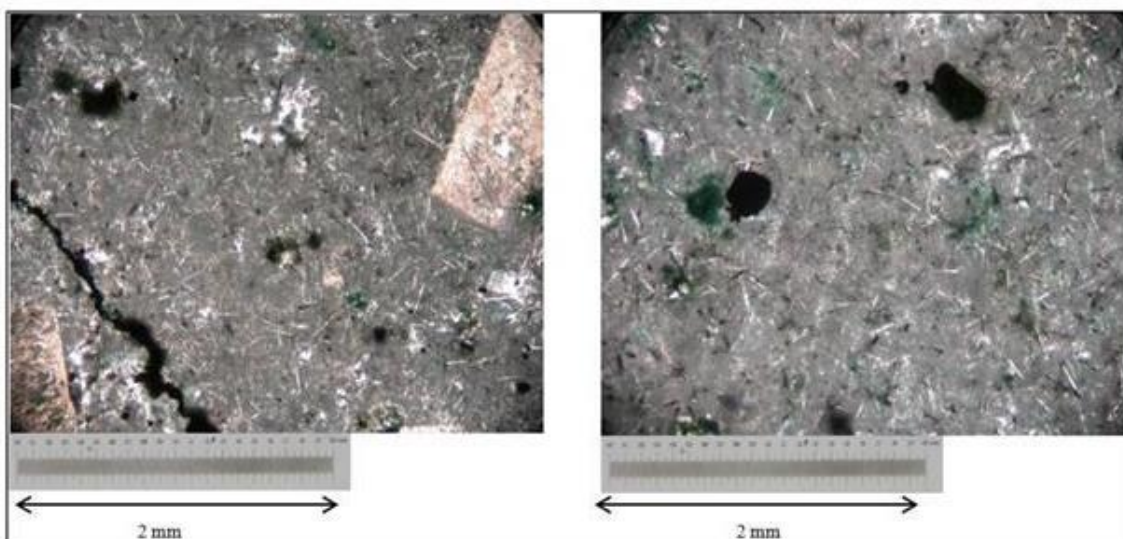


Figure 1: Thin section images of the core plugs from 4874 ft show a largely aphanitic texture with a few large quartz grains interspersed across. Porosity is not clearly observed suggesting small size pores which are described in detail in the SEM images.



Bakshi, Halvaei and Ghassemi

Figure 2: Thin section images of the core plugs from 10,365 ft, these also show a more aphanitic texture with a few large quartz grains interspersed across. Unconnected porosity and a micro-crack can be seen here (both black).

2.3 Scanning electron microscope (SEM) analysis

SEM imaging was used to understand the pore structure of the core – this includes mainly pore sizes, pore connectivity and presence of micro cracks. The following images show the pore structure at two different magnification levels. The core from 4874 ft shows pores of 20-100 µm at a 35x magnification. Most of the pores appear to be small though. Several large quartz grains (1-2 mm) can be seen interspersed within the sample (marked as green circles in figure 3). Pore connectivity is good. No micro cracks are seen here.

For the 10,365ft core, the structure is markedly different. No porosity is evident here in the 35x magnification. In the 240x magnified image though, a few pores can be seen with sizes less than 50 µm. A healed fracture is seen here, many more can be seen throughout the sample.

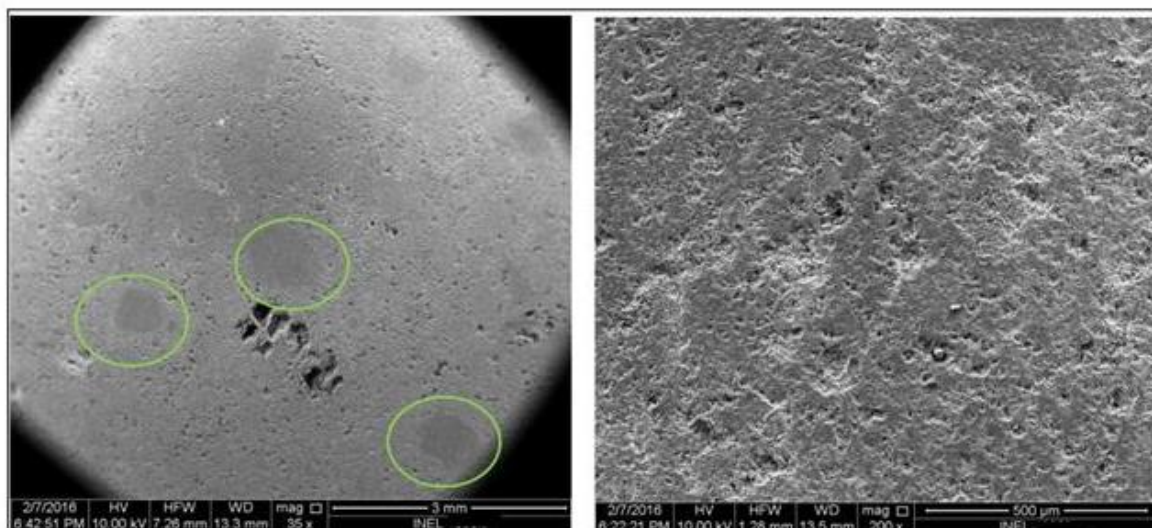


Figure 3: SEM images of the 4874 ft core

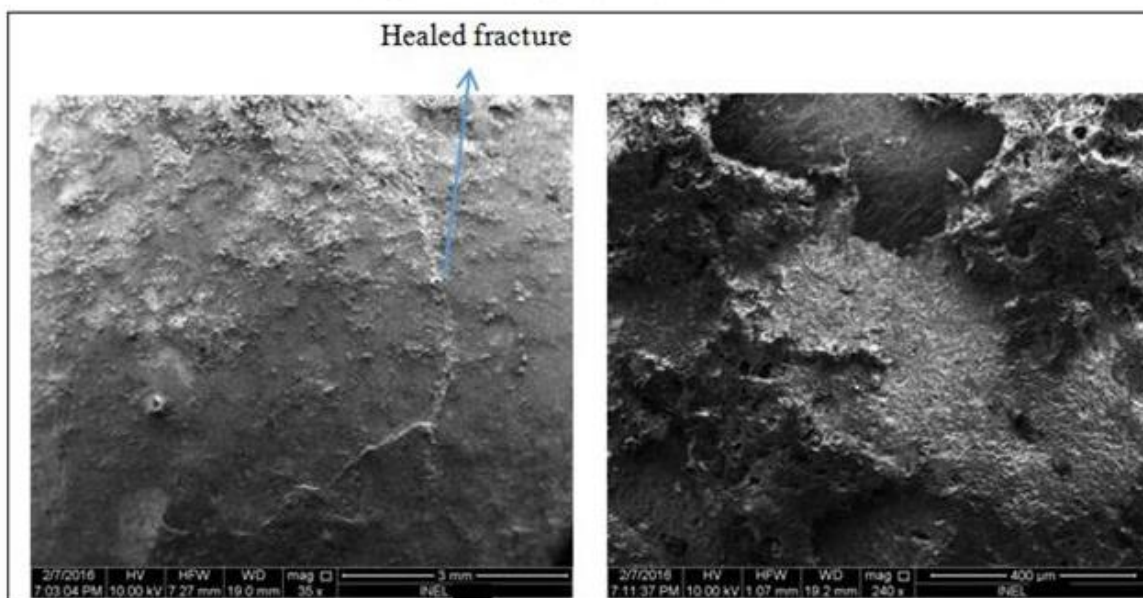


Figure 4: SEM images of the 10,365ft core

Bakshi, Halvaei and Ghassemi

2.4 Porosity and Permeability

Porosity and Permeability were measured for all samples before triaxial testing using an automated Porosimeter-Permeameter. The Porosity was measured first using Boyle's law technique using Helium expansion at different confining pressures. Helium was injected at both the ends of the core sample to achieve equilibrium faster. Below plot shows the variation of porosity (0.5%-11%) with confining pressure, the deeper core from 10,365ft depth was found to have very low porosity.

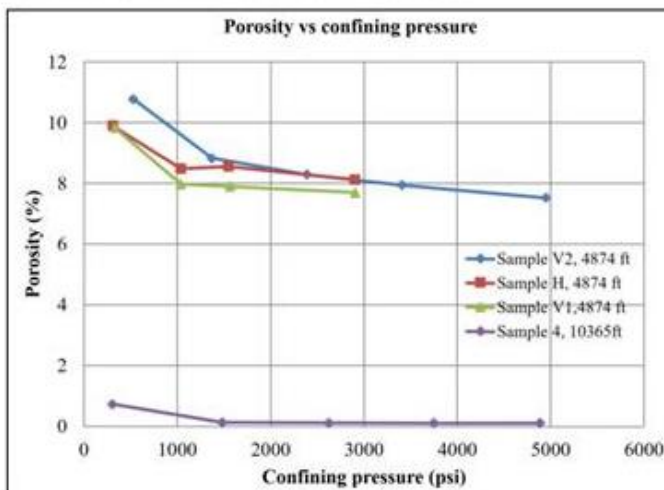


Figure 5: Porosity vs confining pressure for four core plugs from the INEL-1 core, sample depths are provided

Total porosity (crushed) was also measured using the displaced fluid method by taking a piece of core and crushing it to obtain grain density and total porosity values for both the core depths. These are shown below:

Sample	Bulk density (g/cc)	Grain density (g/cc)	Total porosity (%)
10365 ft	2.53	2.66	4.67
4874 ft	2.30	2.63	12.49

Table 2: Density and total porosity for INEL core plugs

The values of crushed porosity are very different from the connected porosity for the deeper core section; this indicates that it possibly has lots of unconnected pores.

Permeability was measured using the standard unsteady state pressure decay technique. The data is used to determine the equivalent liquid permeability, slip and turbulence factors. An equivalent air permeability at a defined confining pressure can also be calculated. Both these tests were done before triaxial testing of the sample.

To evaluate the permeability of the sample during triaxial testing, two precision syringe pumps are used to maintain a small pressure differential of 100 psi across the sample under a given confining pressure. Although any fluid can be used for permeability measurements, nitrogen gas was used in these experiments. Klinkenberg corrections were applied to correct for slippage. One way to avoid the need for corrections is to use higher pore pressure (>2000 psi). The confining pressure must be adjusted to maintain the required effective confining pressure during the test. Then, sample is left for achieving steady state – this is achieved when the flow rate in both the upstream and downstream pumps becomes approximately the same (figure 6).

The time period to achieve steady state varied – for Tuff or shales of nano-darcy permeability, 6-12 hours are needed (if using gas only, liquids can take a week or more). Hence for all samples with ~ micro-darcy or lower permeability, gas was used.

Bakshi, Halvaci and Ghassemi

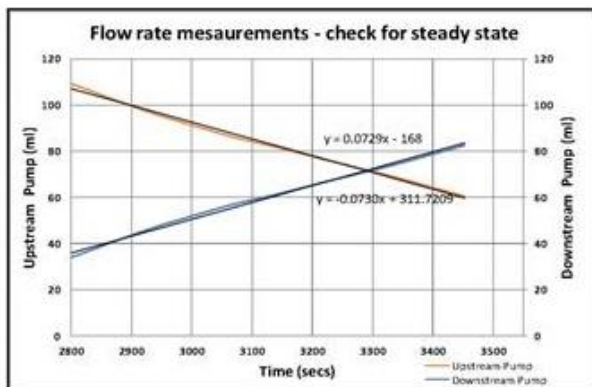


Figure 6: Plot shows steady state equilibrium between upstream and downstream pumps for measuring permeability.

3. DYNAMIC VELOCITY MEASUREMENTS

Both Compressional and shear velocities were measured using 500 kHz crystals at hydrostatic pressure of 3500 psi before triaxial testing. The following table shows these values for the respective samples:

Sample	P-wave velocity (m/s)	S-wave velocity (m/s)	Dynamic Elastic Modulus (GPa)	Dynamic Poisson's ratio (unitless)	Vp/Vs
V1	4089.46	2633.74	36.36	0.15	1.55
V2	3872.02	2516.81	32.64	0.13	1.54
H	5292.86	3425.12	59.40	0.14	1.55
Sample 4, 10365 ft	4648.65	3286.62	55.14	-	1.41

Table 3: Dynamic measurements on the INEL core plugs

As can be seen, both Compressional and shear velocities increase with depth. There is significant difference between velocities measured between vertical and horizontal plugs from the 4874ft depth. This indicates anisotropy between vertical and horizontal properties. As can be seen in the static measurements section later, this translates into a higher strength for the horizontal core plug as compared to a vertical plug as expected. Ratio of Compressional to shear velocities varies between 1.4-1.5.

A comparison between the static and dynamic measurements (Elastic modulus and Poisson ratio) is provided in the summary table below.

4. STRENGTH AND MODULUS MEASUREMENTS

4.1 Multistage triaxial and triaxial-injection testing

Triaxial testing normally involves taking several samples from the same depth (or close depths) and then subjecting them to triaxial tests at varying confining pressures to define the strength envelope. However, limited sample availability and sample heterogeneity can result in variations in strength and other parameters resulting into difficulties in defining a meaningful envelope. Multistage triaxial testing (Kovari and Tisa in 1975) has been used increasingly in defining strength envelopes (Wang et al., 2016). Use of multistage triaxial testing involves subjecting the sample to varying confining pressures and applying deviatoric stress to levels which won't cause irreversible damage. The range of confining pressures can be defined depending upon the expected stress levels in the reservoir. Prevention of permanent damage can be ensured by using a criterion to define when to stop applying deviatoric (see Tran et al (2010), Kovari and Tisa (1975), Kovari et al. (1983), Kim and Ko (1979), Crawford and Wylie(1987)). For the purpose of this paper, the experiments which were carried out have used the volumetric strain deflection in conjunction with AE information to define the stopping point.

In a triaxial test combined with injection (to replicate in-situ stimulation practice) the sample is loaded to the point of dilatancy where the volumetric strain curve shows a deflection. Then, the pore pressure is increased to induce rock failure.. The test provides useful data for stimulation treatment design. We performed two variants of this test. In the first case, the sample was stressed axially to a pre-determined level (close to failure based on analysis of reservoir stress data) with a certain confining pressure, then the pore pressure was

Bakshi, Halvaei and Ghassemi

increased and the sample deformation was observed. If the sample did not fail, a higher pore pressure and/or differential stress was applied to induce failure. In the second case, the sample was loaded until the deflection in the volumetric strain was observed. Then, the pore pressure was increased to bring the sample to failure. In each case, the principal stresses at failure were measured.

Two multistage triaxial compression tests, two injection tests, and five Brazilian tests were carried out to determine the geomechanical properties and the Mohr-Coulomb failure envelopes. Also, permeability before and after tests was measured for all the triaxially tested samples.

Figure below shows the four core plugs used for triaxial and injection tests. All samples are one inch in diameter and have a length to diameter ratio of 2:1 with the exception of sample H, which had a ratio of 1.92:1. It can be observed that, the three core plugs from 4,830ft had no visible fractures and looked very similar in appearance. However, the core plug from 10,365 ft depth had several healed fractures.



Figure 7: Pictures of samples before the triaxial or injection tests

Two samples – both from the well INEL-1, were subject to multistage triaxial tests; four to five different confining pressure stages were used for these tests and the samples were taken to failure using gas injection in the last loading stage. The axial stress was applied using a strain control mode at a rate of 5×10^{-6} strains/sec. The following procedure was followed:

1. Sample is jacketed with a thin copper jacket (0.003" thickness) and 8-12 acoustic crystals are added on the jacket at fixed locations.
2. Sample is hydrostatically loaded to a confining pressure slowly while monitoring strain.
3. Sample is then loaded deviatorically until volumetric strain deflection is observed, at this point sample is unloaded. Confining pressure is changed for the next stage. This is repeated until the last stage.
4. In the last stage, failure is initiated using injection while the sample is under a confining pressure of 3500 psi and an axial load which causes a negative change in volumetric strain. This has been described earlier.

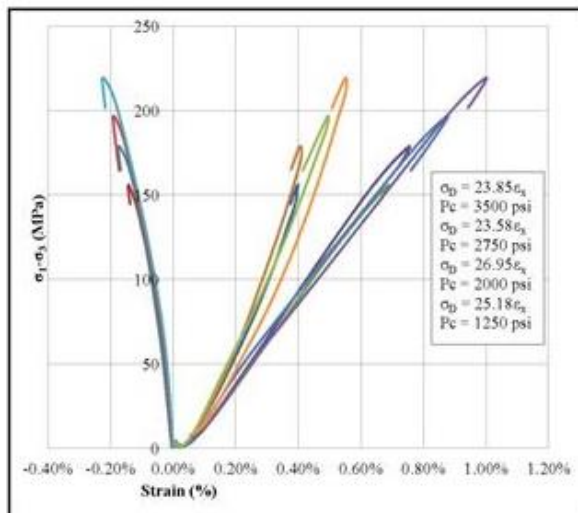


Figure 8: Stress strain response at four stages of multistage triaxial test for INEL-V1 (4874 ft depth) sample. Volumetric deflection point increases with increase in confining pressure signifying higher strength; Young's modulus also increases slightly at higher confining pressures.

Bakshi, Halvaci and Ghassemi

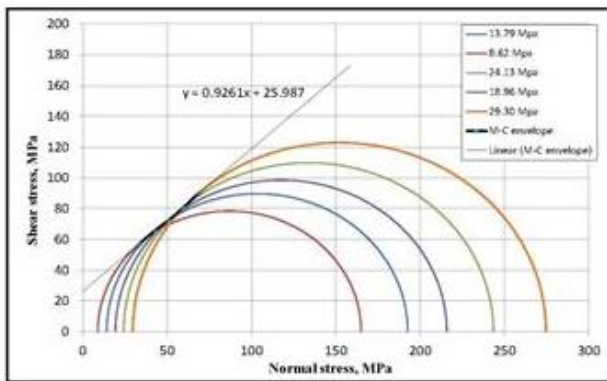


Figure 9: Mohr-Coulomb plot for INEL sample V1, depth 4874 ft.

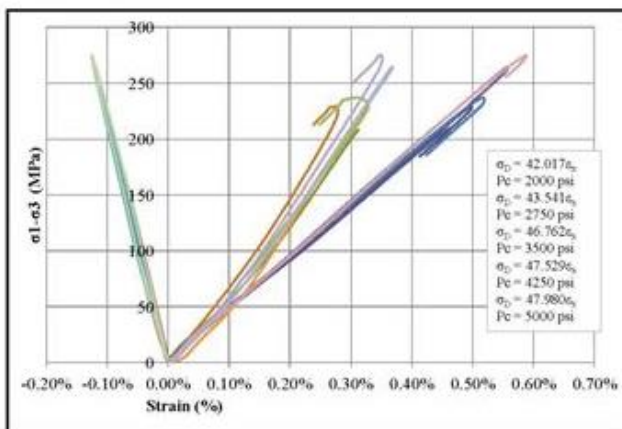


Figure 10: Stress strain response at four stages of multistage triaxial test for Sample no 4, 10365ft depth. Volumetric deflection point increases with increase in confining pressure signifying higher strength; Young's modulus also increases slightly at higher confining pressures. As compared to the shallower samples, this shows more strength.

The failure envelope for both the samples was calculated assuming that the best fit tangent line of non-failure Mohr circles has the same slope as the failure envelope, as shown in fig. above using technique defined by Pagoulatos (2004).

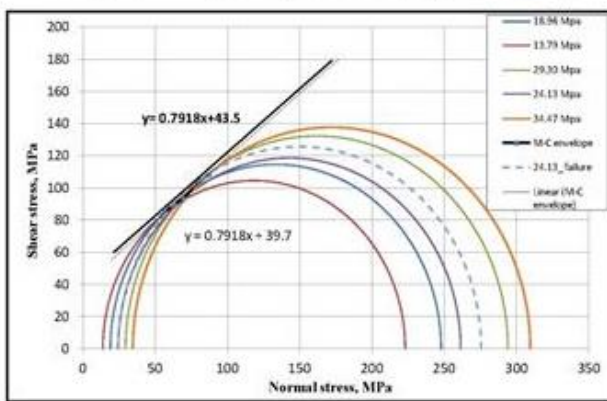


Figure 11: Mohr-Coulomb plot for INEL sample no 4, depth 10365 ft.

Bakshi, Halvaei and Ghassemi

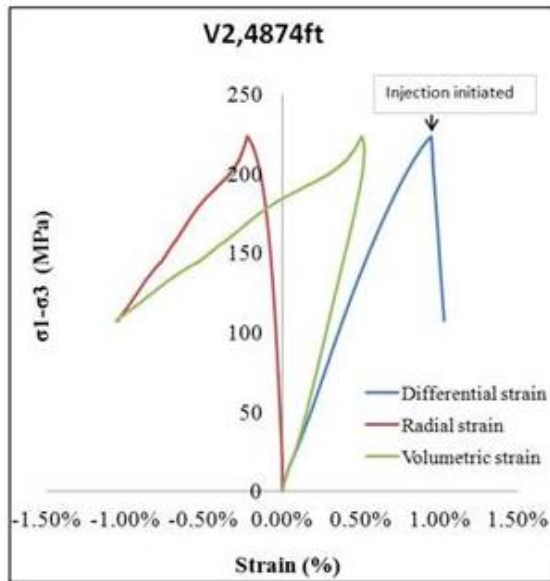


Figure 12: Triaxial – injection plot for sample V2, 4874ft depth

	Sample			
	V1, 4874ft	V2, 4874ft	H, 4874ft	Sample-4, 10365ft
Static Young's modulus (GPa)**	27.5	27.0	34.8	46.8
Static Poisson's Ratio**	0.17	0.15	0.16	0.16
Unconfined Compressive Strength (MPa)*	132.2	-	-	179.2
Cohesion (MPa)*	29.5	-	-	43.5
Friction angle*	42.8°	-	-	38.2°
Peak strength (MPa)**	229.8	223.5	260.1	251.4
Dynamic Young's modulus	36.4	32.6	59.4	55.1
Dynamic Poisson ratio	0.15	0.13	0.14	-

* - Measured using Mohr Circle data

** - Measured at 3500 psi confining pressure

Table 4: Summary of static and dynamic measurements performed on samples from the INEL-1 well

Bakshi, Halvaei and Ghassemi

Following inferences can be made from the measurements recorded above:

1. There is some anisotropy between horizontal and vertical plugs from the 4874ft core. Horizontal plug shows higher strength and higher young's modulus in both static and dynamic measurements.
2. Dynamic and static Poisson's ratios are almost same (within 10%). However static and dynamic young's moduli are different (14-41% difference, average 25%) but show similar trend in all four plugs with higher values in dynamic measurements.
3. Deeper core samples (lithologies) are stronger than the shallower core and have higher elastic modulus. This correlates very well with their porosities (lower porosity in deeper core) and velocities (higher velocity in deeper core).
4. Young's modulus increases very slightly as confining pressures are increased in the multistage triaxial tests- this indicates that these rocks are well compacted already.



Figure 13: Pictures of samples after testing; copper jacket hasn't been removed to prevent sample disintegration. Red lines show clear fractures seen on surface. Location of these fractures in 3-D has been studied in next section using acoustic emissions.

4.2 Brazilian Test (Indirect Tensile Strength Test)

Indirect tension tests often referred to as Brazilian tests were performed on plugs from both the core depths. The indirect tensile strength of the specimens were calculated as follows:

$$\sigma_t = \frac{2P}{\pi D t}$$

Where, σ_t is the Brazilian tensile strength (MPa); P is the load at failure (N); D is the diameter of the specimen (mm); t is the thickness of the specimen (mm) (ISRM 1978). A picture of the test assembly and a test result for the sample from 10,365ft depth are shown below.

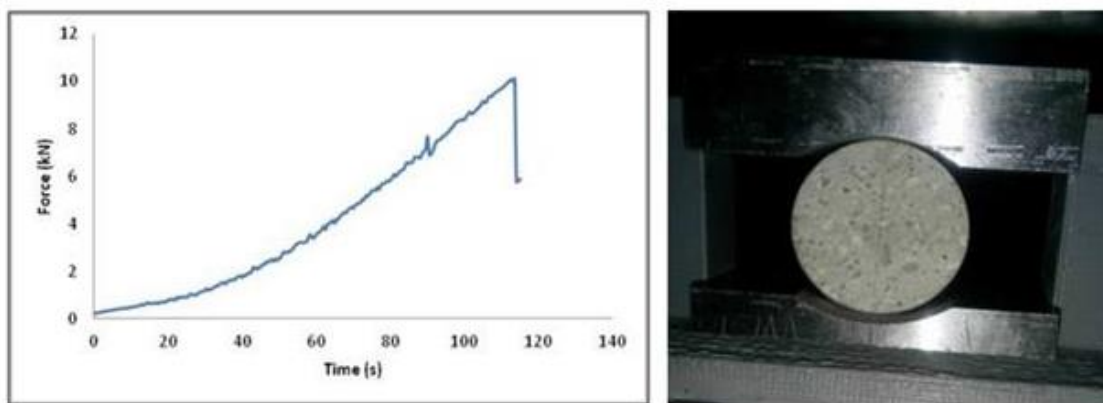


Figure 14: Axial force vs time plot for sample B1 (left) and picture showing the crack at centre of sample after Brazilian test.

Table 5 shows a summary of the tensile strength values for the five samples that were tested. It can be seen that the three plugs from 10,365 ft show significant variation in strength, this happened due to presence of healed fractures in all three samples. S2 had fewer fractures and hence shows higher strength. Samples were loaded to get highest possible value of strength (perpendicular to fractures).

Bakshi, Halvaei and Ghassemi

Sample name	Indirect Tensile Strength (MPa)
S1 (10365 ft)	19.2
S2 (10365 ft)	24.8
T1 (10365 ft)	13.8
B1 (4874 ft)	20.0
B2 (4874 ft)	15.2

Table 5: Brazilian test results for the INEL core plugs, the variation in the three values for the 10365 ft can be explained on the basis of presence of natural fractures

5. PERMEABILITY CHANGES DUE TO ROCK FAILURE

Table 6 describes the changes in permeability observed after fracturing. It should be noted that during compressional loading two processes compete – the sample compression reduces permeability due to pore closure, while micro fracturing or shear fracturing increases permeability. Permeability has been observed to decrease with increasing triaxial loading (even after fracture) for high porosity samples like sandstones and to increase for low porosity samples (Ohaka, 2010). The final permeability change is also a function of whether the fracture intersects the ends of the sample or more localized. Horizontal sample permeability was not measured during these tests. It can be seen from below table that most of the samples showed large increases in permeability after fracturing which shows that injection experiments could be successful in creating improved fluid flow in these rocks. The final values of permeability though are still low (μD).

Plug	Initial permeability (μD)	Final permeability (μD)	Ratio of Final to initial permeability
V-1, 4874 ft	18.2	1668.0	92
V-2, 4874 ft	0.068	0.590	9
H, 4874 ft	0.197	10.138	44
Sample 4, 10365	0.086	17.357	201

Table 6: Permeability values before and after triaxial testing for the INEL core plugs

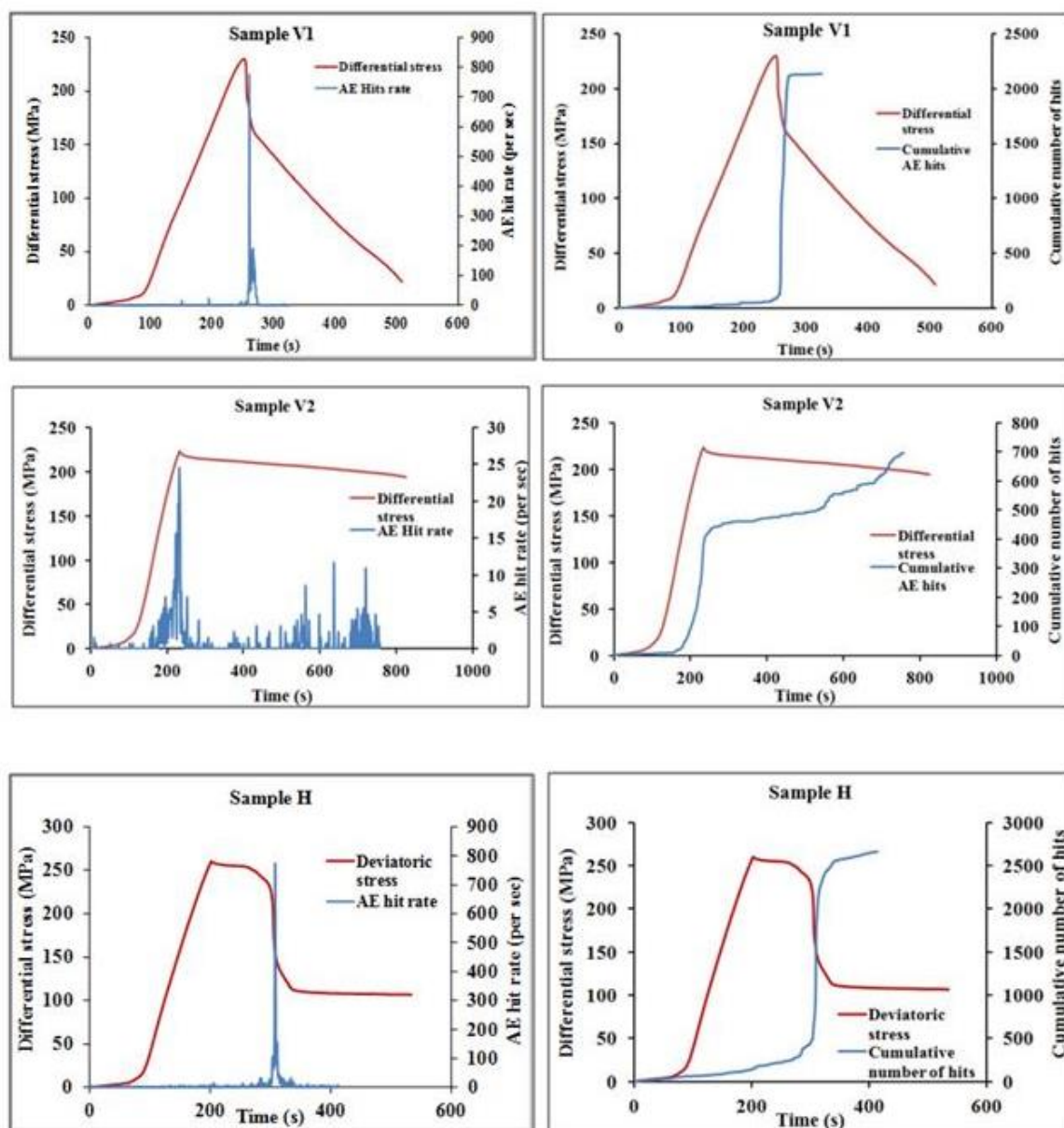
6. ACOUSTIC EMISSION ANALYSIS DURING ROCK FAILURE

The MISTRAS Express-24 channel, Acoustic Emission (AE) system with a frequency range of 1KHz - 1MHz was used with 8 to 12 AE sensors per sample for recording acoustic emissions generated during the triaxial tests. These sensors were attached to the sample using epoxy. A preamplifier of 40 dB was applied to all the sensors. The amplitude cut off on these sensors varied from 45-55 dB; any wave below this amplitude is discarded by the system as noise. Frequency and energy of failure events were also recorded during the tests – these give insights into the nature of failure, typically higher confining pressures result in lower energy released during the failure if the rocks become more ductile. A sample rate of 1 MSPS (million samples per second) was used to record the AE information. 3-D location analysis was also performed using AE information – this technique uses the source amplitude and the differences in time it took the wave to reach the different sensors to arrive at the location of the event. 3-D location is highly dependent upon the rock type – rocks which generate low AE (including Tuff) typically do not give a good 3-D location response as compared to very brittle rocks which generate high amplitude AE waves during the failure process.

AE/MEQ analysis was carried out for all the tests. Figure 15 below shows the time - stress responses in conjunction with AE information for each of the four tests. The figures show the rate and number of hits observed during the respective tests. It can be observed that generally the rocks tested have a good AE response with the strongest AE response observed close to and during failure. Also, low AE activity is observed after failure when slip takes place on the shear surface. Samples V1 generated low AE after failure while samples V2, H, and 4 show good AE response to fracture slippage. Overall the highest number of events were recorded for sample H and followed closely by V1, and 4 and far less for V2. This can be explained as follows:

Bakshi, Halvaei and Ghassemi

1. Sample H has the highest strength and is more brittle (sharp drop in stress after failure) than all other samples. This clearly contributed to its high AE rate and total number of events.
2. Sample V1 and sample no 4 both generated similar number of hits, however in terms of rate of AE generation, sample V1 had double the rate at fracture initiation as compared to sample no 4. This is because sample 4 had several healed fractures before testing and deformation localized on those prior to the formation of a new fracture plane. On actual observation after failure, sample 4 had several failure planes – it failed along the healed fractures in addition to newly generated failure planes resulting in a more gradual failure process than V1 which failed in a highly brittle manner.
3. Sample V2 had the lowest AE response, this despite it having almost the same strength and coming from the same exact depth as V1 and almost similar dynamic and elastic modulus. This can be attributed to presence of micro cracks in V1 which contributed to a good initial permeability value (more than 250 times that of V2). As a result the pore pressure within V1 was able to increase more rapidly throughout the sample, causing a more brittle failure as compared to V2 which had a very ductile failure. It can be seen in table 6 that even the final permeability in V2 after failure is lower than the initial permeability in V1.



Bakshi, Halvaei and Ghassemi

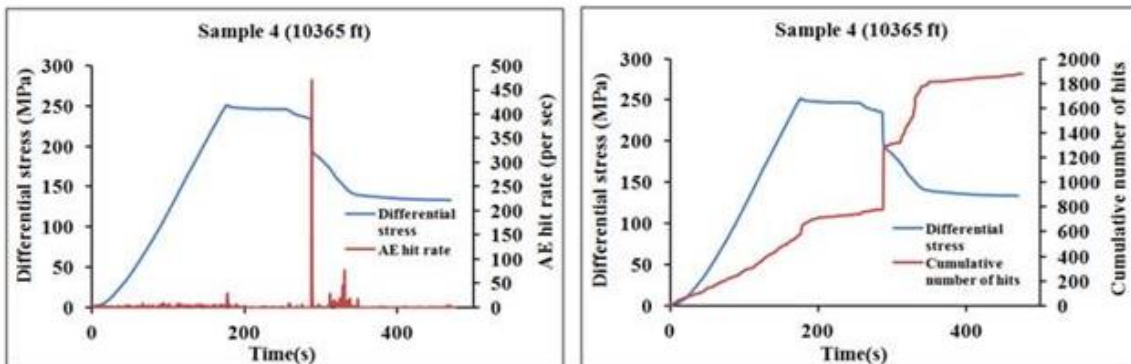
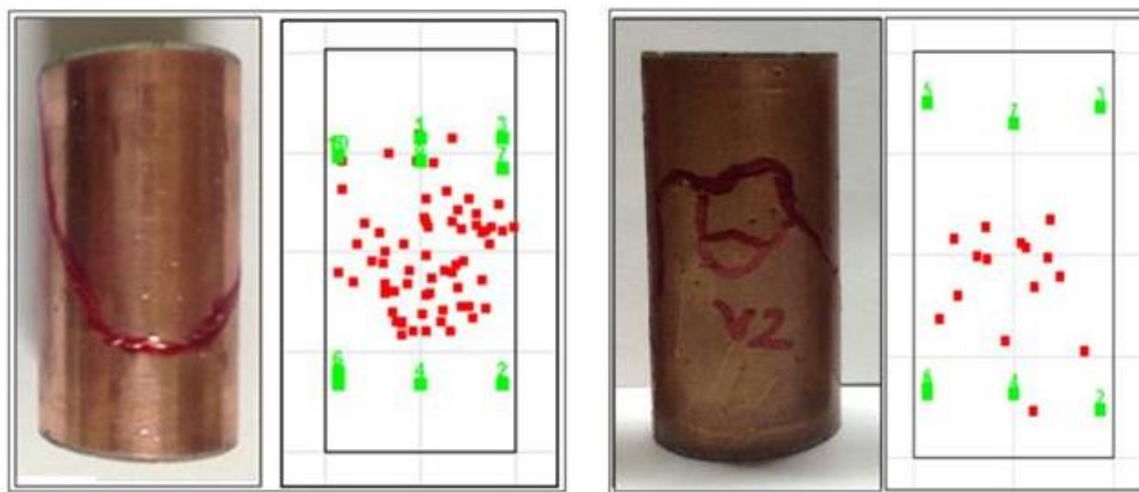


Figure 15: AE hits rate and cumulative number of hits correlated to axial stress during triaxial testing observed in the four INEL -1 well core plugs. More brittle failure (V1, H and sample no 4) show high number of hits as compared to sample V2 (ductile failure – observe stress plot). Most of the hits are generated during fracturing although some are generated just before and during fracture sliding.

It should be noted that the AE was recorded using 8-12 sensors and these rocks were observed to generate far less AE activity when compared with sandstones (for example Berea sandstone in a similar experiment generated over 10000 hits). AE responses vary from rock to rock and typically.

The following plots show the 2-D and 3-D location analysis of AE events for all the four samples. The figures show the failed sample next to the 2-D location plot and a three dimensional plot showing location of events. It should be noted that the red lines on the sample show the fracture location. Also, location analysis shows the location of micro-fracturing in addition to the large shear fracture locations.



Bakshi, Halvaci and Ghassemi

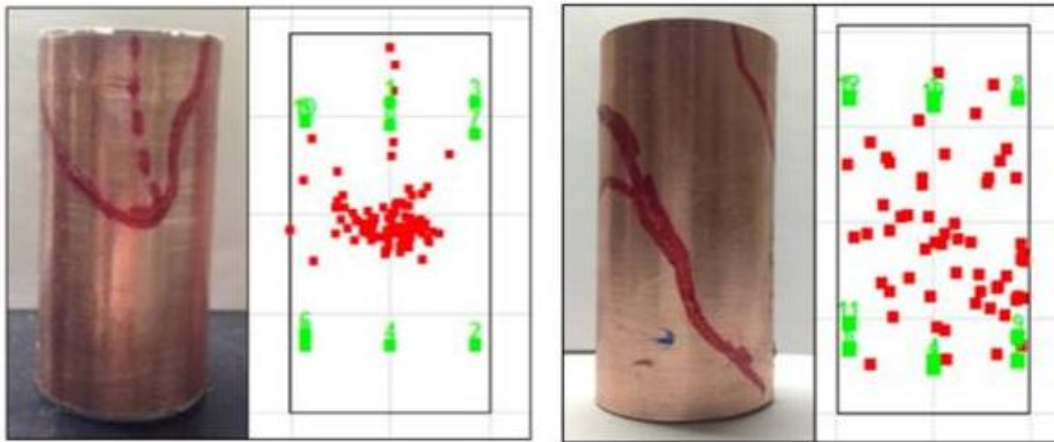


Figure 16: Sample 2D location plots with Sample V1 (top left), sample V2 (top right). Sample H (bottom left) and Sample no 4 (bottom right) showing event locations in 2-D within the sample as compared with the fracture location in the respective samples (marked red). Location algorithm picks up micro cracking as well within the sample.

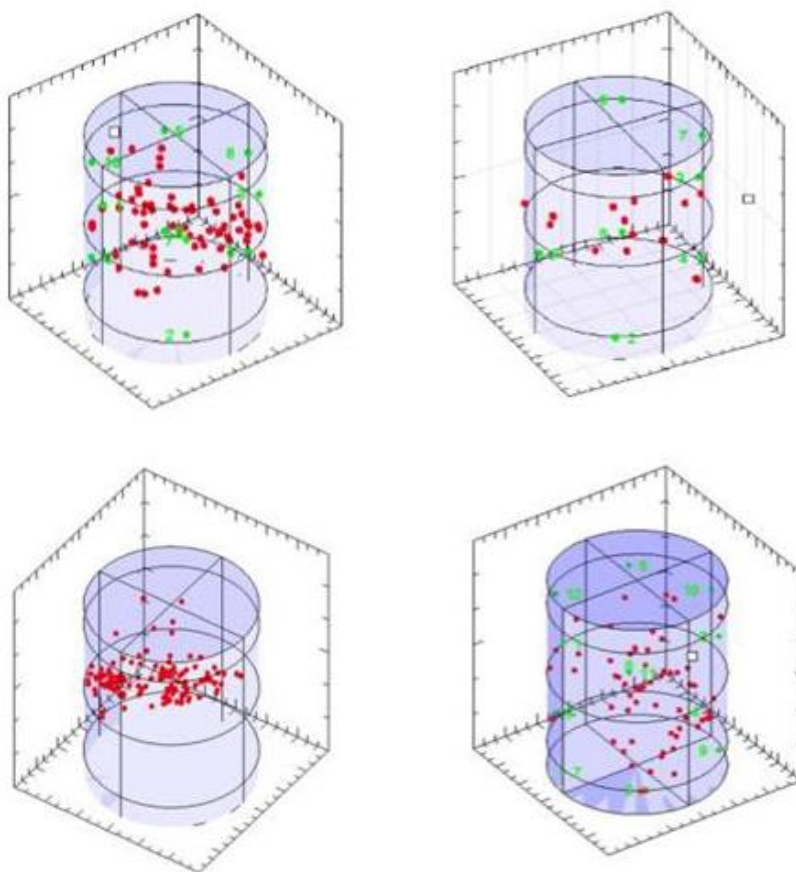


Figure 17: Sample 3-D location plots showing event locations in 3-D within the sample (right)

Bakshi, Halvaci and Ghassemi

CONCLUSIONS

Geomechanical properties of drill cores from the INEL-1 well have been characterized in this work. The results provide information regarding the elastic and failure properties along with pore structure, compositional analysis, and porosity and permeability. The mineralogical analysis clearly shows presence of mainly feldspars (42-48%) and silica (24-27%). Clay composition varies from 24-27%. Porosity varies from 14% at the 4,874ft depth to 4% at 10,365 ft depth – this can also help understand the higher strength in the deeper core. The deeper core showed the presence of healed fractures and the sample failed along these fractures. Elastic properties were found to increase with depth and a high MEQ rate was also observed. This can be seen in the much higher values of Young's modulus in the deeper core. Velocity measurements show considerable anisotropy in vertical and horizontal plugs in the 4874ft core – this correlated very well with strength measurements on the core plugs with horizontal plugs showing higher strength and velocities. Since only one plug was available from 10,365 ft depth, it is recommended to obtain more plugs with a different orientation to understand variations in strength, if any. Permeability measurements clearly show a large increase after fracturing – this shows that although fracture closure in absence of proppants will reduce overall conductivity, it will still be much higher than existing permeability. AE activity was observed during the tests, and was observed to increase exponentially during fracture with low activity during slippage.

Bakshi, Halvaei and Ghassemi

REFERENCES

- Williams, C.F., Reed, M.J., and Mariner, R.H., 2008, A review of methods applied by the U.S. Geological Survey in the assessment of identified geothermal resources: U.S. Geological Survey Open-File Report 2008-1296 [<http://pubs.usgs.gov/of/2008/1296/>].
- Miller, L.G., Prestwich,S.M., Griffith,J.L., 1978, INEL/Snake River Geothermal Drilling and Testing plan – INEL-1 Well
- Moos, Daniel, Barton, Colleen A., In-situ stress and natural fracturing at the INEL site, Idaho (1990).
- Li, Yawei, Wang, Jihoon, Jung, Woodong, Ghassemi, Ahmad, Mechanical properties of intact rock and fractures in welded Tuff from Newberry volcano.
- Kovari, K., Tisa, A., Einstein, H., and Franklin, J.A. (1983), "Suggested methods for determining the strength materials in triaxial compression," Int. J. of Rock Mech. & Min. Sci. & Geomechs Abs. 20: 283-290.
- Kim, M. M., and H. Y. Ko.(1979), "Multistage triaxial testing of Rocks," *Geotechnical Testing* 2: 98-105.
- Goodman, R.E, (1989), "Introduction to Rock Mechanics, 2nd Edition"
- Lutz, Susan Juch, Hickman, Stephen, Davatzes, Nicholas, Zemach, Ezra, Drakos, Peter, and Ann Robertson-Tait, Rock mechanical testing and petrologic analysis in support of well stimulation activities at the Desert peak geothermal field, Nevada
- Ohaka, Stanley, Evolution of porosity and permeability during brittle faulting, 2010
- Kwasniewski, M. Mechanical behavior of rocks under true triaxial compression conditions; volumetric strain and dilatancy. *Archives of Mining Sciences* [0860-7001] yr.2007 vol.52 iss.3 pg:409
- Crawford, A., and Wylie, D. (1987), "A modified multiple failure state triaxial testing method," 28th US Rock Mechanics Symposium, 133-140.
- Tran, D.T., Pagoulatos, A., Sondergeld, C.H. (2010), "Quantify Uncertainty of Rock Failure Parameters From Laboratory Triaxial Testings Using Conventional And Multistage Approaches," 44th U.S. Rock Mechanics Symp., June 27 - 30, 2010, Salt Lake City, Utah.
- Y. Bernabe' , U. Mok, and B. Evans. Permeability-porosity Relationships in rocks subjected to various evolution processes. *Pure Applied Geophysics*. 160 (2003) 937–960

Appendix G

Geomechanical Modeling

Appendix G

Geomechanical Modeling

Geologic Model Background

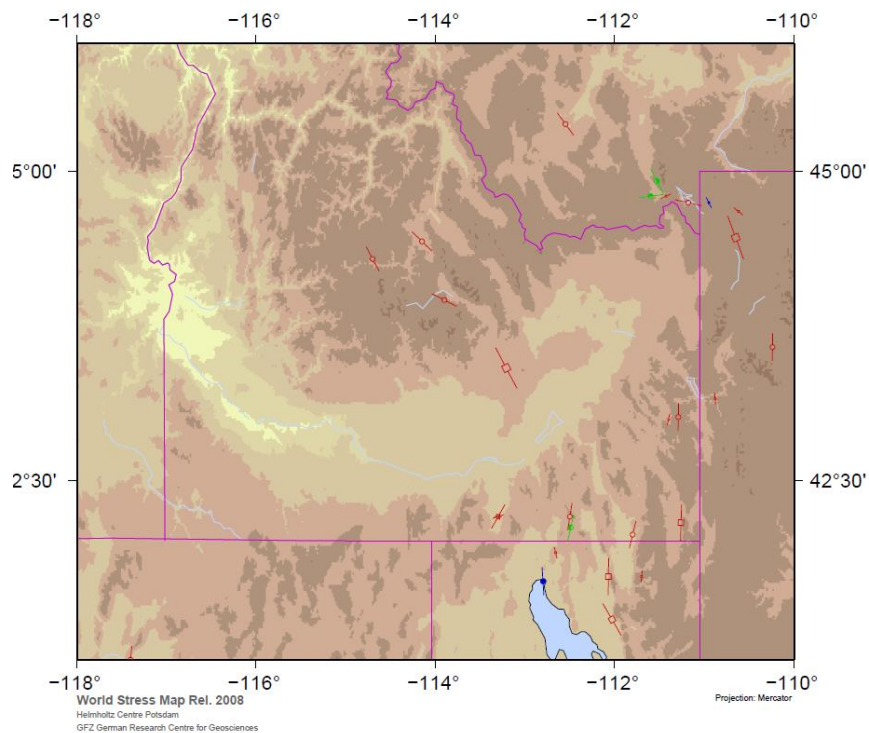
The Idaho National Laboratory (INL) is sited on the Eastern Snake River Plain (ESRP) west of Idaho Falls, Idaho. The Snake River Plain cuts a concave northward arc across the Northern Basin and Range physiographic province, the trace of a hotspot whose present position is marked by the Yellowstone caldera (e.g., Morgan, 1972). In the ESRP, initial silicic volcanism has since given way to extensive extrusion of basalts that now overlie the silicic volcanics. This volcanism is still active; flows within the Craters of the Moon National Monument a few miles west of INL are less than 10,000 years old (Kunz et al., 1986).

Information regarding the composition of the materials that underlie the ESRP has generally been obtained from interpretations of surface geophysical investigations. Analyses of cores and cuttings obtained during drilling of the INEL-1 borehole provide one of the few direct observations of the subsurface (Prestwich and Bowman et al., 1980). Based on these analyses, more than 610 m of basalts have been extruded onto the ESRP. Sands and gravels are interlayered with these basalts. The underlying silicic volcanics extend to the total depth of more than 3.1 km. These include more than 1,675 m of welded tuffs, with minor amounts of cinders and tuffaceous interbeds. Dense, recrystallized hydrothermally altered rhyodacite ash-flows were found in the borehole below about 2,500 m. Below this depth, the rock becomes increasingly dacitic; at 2,880 m, an abrupt change to dacites was inferred from an increase in logged density. At greater depths, basaltic intrusions comprise as much as 25% of the present 40-km-thick crust, based on interpretations of seismic refraction data (e.g., Sparlin et al., 1982).

Snake River Plain Tectonics

Basin and Range tectonic activity characterizes the regions on both sides of the ESRP, as characterized by the 1983 Borah Peak earthquake immediately to the north of the INL Site. Although significant activity appears to be concentrated within a parabolic arc with its head beneath Yellowstone National Park, no earthquakes larger than $M_s = 3$ have been detected in the period since 1961 beneath the plain itself. However, feeder vents for the extrusive basalts are aligned in a north-northwest direction, suggesting that the plain is extending in the same direction as the surrounding province. A number of ideas have been proposed to explain the lack of seismic activity beneath the plain. These include that the plain is undergoing ductile deformation, a consequence of elevated subsurface temperatures (e.g., Furlong, 1979), or alternatively that the basalts are simply too strong to fail (Anders et al., 1989).

The stress orientation data for a larger region surrounding the plain was compiled from the World Stress Data Base and includes data through 1989. Three earthquakes in northern Nevada indicate a roughly NE-SW direction of principal horizontal compression in the Basin and Range and a normal faulting environment. A series of earthquakes near the Idaho/Utah border suggests a similar magnitude and orientation of the principal stress field immediately to the SE of the plain. Immediately to the north of the Snake River Plain (SRP), maximum compression trends NW-SE, as illustrated by the stress directions inferred from the 1983 Borah Peak normal faulting event (indicated by a solid triangle).

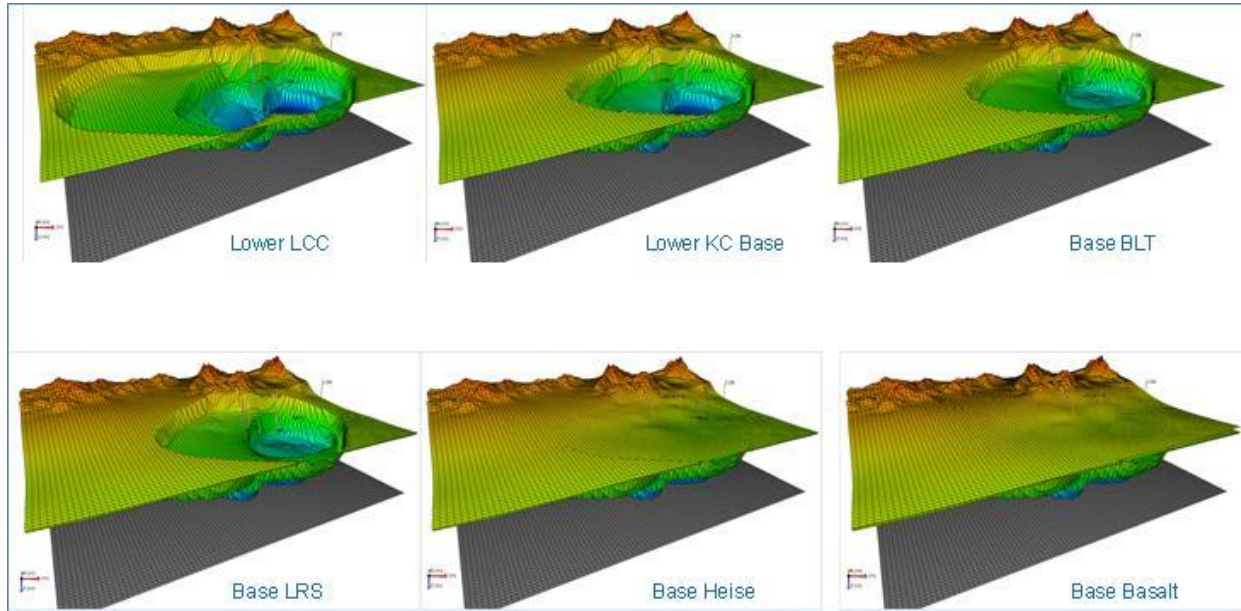


One- to Three-Dimensional Geomechanical Modeling of the ESRP

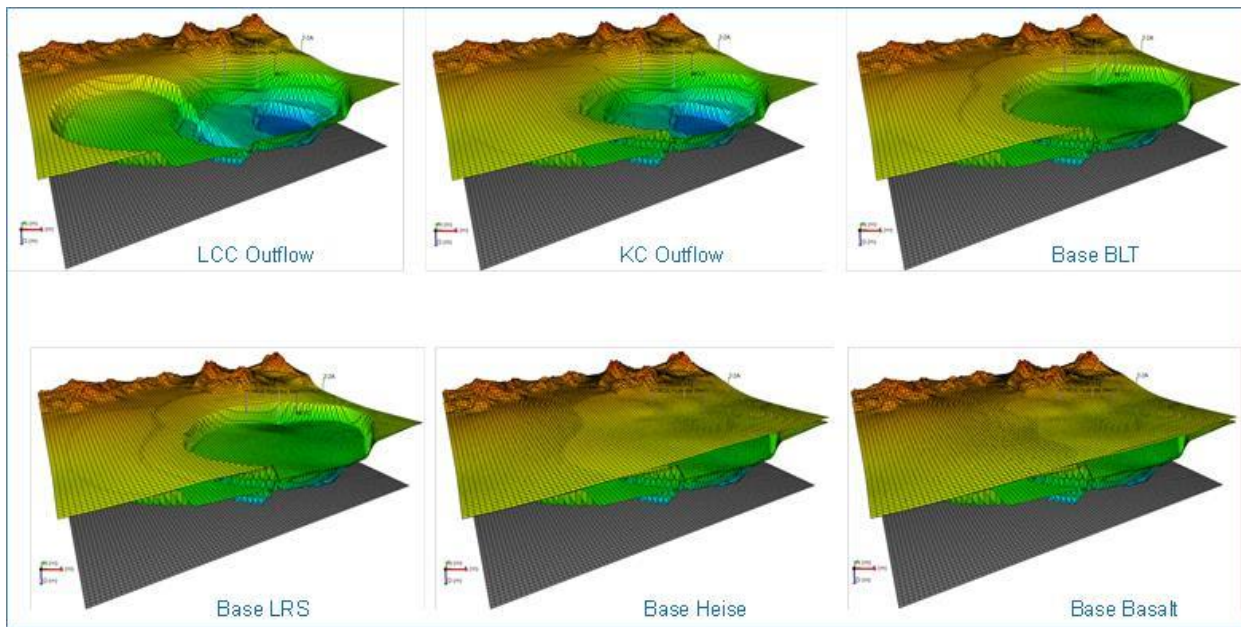
In low-matrix-permeability reservoirs, such as the ESRP, stimulation response is controlled largely by the properties of natural and induced fracture networks, which are in turn controlled by the in situ stresses, the fracture distribution and connectivity, and the hydraulic behavior of the fractures. Exploiting this complex interaction requires knowledge of the present-day stress field at the reservoir scale for effective and efficient stimulation.

The methodology to fully characterize the subsurface at the INL's proposed Frontier Observatory for Research in Geothermal Energy (FORGE) site integrates three field-scale models derived from a broad multidisciplinary set of data. A geologic model provides the structural framework, lithology and reservoirs properties, a three-dimensional (3D) geomechanical model of the magnitudes and orientations of reservoir stresses, pore pressure evolution and rock mechanical properties, and a discrete fracture network (DFN) model fracture characterization and distribution.

Interpreting rock types and distributions within a volcanic setting is complicated by the heterogeneity and discontinuity of the rocks. To develop the 3D geologic framework, geostatistical methods will be applied within a structural grid-cell model built using the JewelSuite software. For the base case model, the facies picks of formation tops from drilled wells are matched to interpreted facies boundaries as a set of well-tie cross sections. This information is used to generate a 3D structural volume with a consistent set of rock types within a given facies region. The base case geologic model result (best-case and worst-case scenarios below) provides the common framework for the subsequent modeling in this study. The base geologic structural model for the proposed FORGE site shows the geologic evolution and subsequent horizons through time.



Best case scenario geologic model.



Worst case scenario geologic model.

A complete geomechanical model consists of estimates of the in situ or present-day stresses (both orientation and magnitude), the rock strength and rock properties, and the pore pressure or formation pressure. In keeping with the majority of work in rock mechanics, tectonophysics and structural geology, we use the convention that compressive stress is positive. We use this convention because in situ stress at depth greater than a few tens of meters in the earth, confining pressure in apparatus, and fluid pressure in pores are always compressive. Positive compressive stress is also the convention used in the field of soil mechanics. This is opposite to the convention adopted in work on the theory of elasticity and continuum mechanics where stresses are assumed positive when tensile (see discussions in Jaeger and Cook, 1979; Zoback, 2007).

In geologically simple reservoirs, a 3D static geomechanical model can be developed based on sufficient well control, attributes derived from geophysical data and structural information. 3D dynamic geomechanical models are necessary where we need to solve correctly pressures in more complex reservoirs such as areas with large topographic relief, e.g., beneath mountain ranges, or with large lateral density contrasts, e.g., adjacent to salt bodies. Dynamic models are also required to calculate stress continuity across faults, stress perturbations due to active fault slip, and changes in stress magnitudes with depletion.

One-Dimensional Geomechanical Modeling Workflow

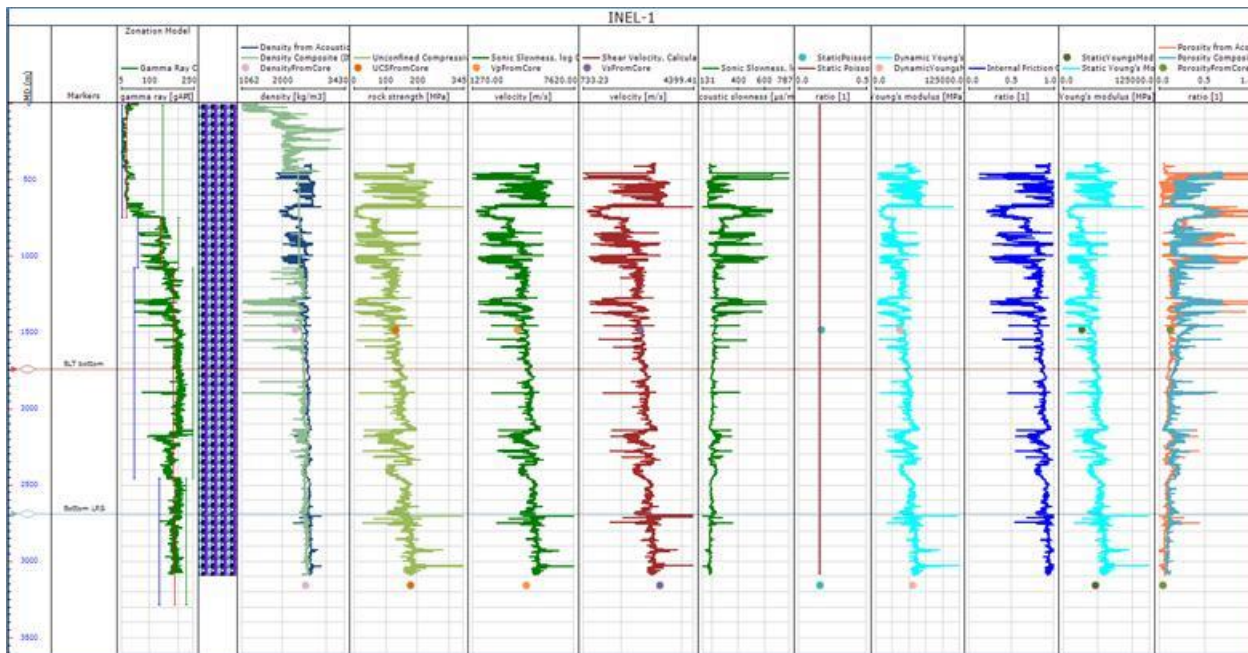
The initial phase of 3D geomechanical modeling involves the development of calibrated, one-dimensional (1D) geomechanical models based on data from wells distributed throughout the geothermal reservoir. The 1D models are an essential step toward creation of a 3D geomechanical model, because they are used to develop and verify static stochastic 3D geomechanical models and 3D dynamic geomechanical finite element simulations of more complex or time dependent aspects reservoirs evolution (i.e., reservoir pressure and temperature evolution with time).

For the FORGE study, offset well data will be utilized to derive 1D profiles of vertical stress, S_v , maximum horizontal stress, $S_{H\max}$, minimum horizontal stress $S_{h\min}$, pore pressure, P_p , and rock mechanical properties (UCS, T_0 , E, etc.). For 1D geomechanical models, we assume that one of the principal stresses acts essentially vertically and that the other two principal stresses act horizontally.

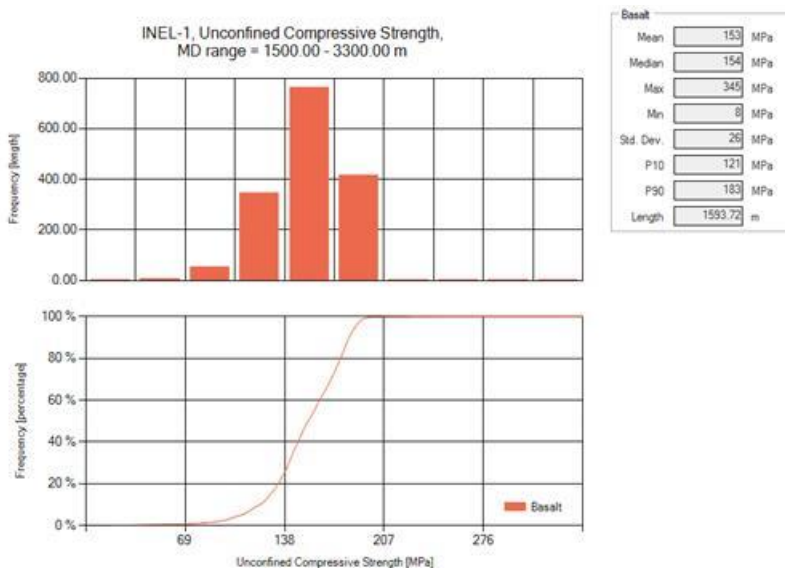
To constrain the stresses within the proposed FORGE site, our team will utilize a broad suite of historical and newly acquired data recorded in wells drilled into SRP to map in detail the magnitudes and orientations of in situ stress across the field. The methodology requires characterization of drilling-induced wellbore failures through analysis and interpretation of available wellbore image data. We will use least principal stress values (S_3) inferred from leak-off tests or mini-fracs, information about vertical stress from density logs, and pore pressure information obtained by direct measurement or inferred from drilling data along with the observed wellbore failures to constrain the full stress tensor in the reservoir.

We use the suite of data recorded in the 3,300-meter-deep INEL-1 borehole in 1990 to demonstrate our proposed approach. Standard logs recorded in the borehole included a density log, neutron porosity, sonic slowness, electrical resistivity, formation temperature, natural gamma ray, and caliper hole size measurements. In addition, analog acoustic televiewer data were recorded over the interval 2,066 to 3120 m and then digitized post-logging (Moos and Barton, 1990).

We will compare values of compressive rock strength obtained in triaxial laboratory measurements against effective in situ rock strength determined through the log-based analysis. Log-based rock mechanical properties are derived through application of empirical relationships to the wireline data to calculate depth profiles of UCS, Young's modulus, Poisson's ratio, and internal friction. The fundamental INL log data and the computed geomechanical parameter profiles are shown in the example below.



Log-derived rock strength must be calibrated against laboratory triaxial rock strength measurements. Newly acquired rock strength measurements (Bakshi et al., 2016) are plotted in this example and show excellent correlation with the log-derived values. A histogram of computed UCS values over the interval 1,500 to 3,000 m yield a P10 of 121 MPa and P90 of 183 MPa. These will values help to constrain the possible magnitudes of the horizontal stresses based on the presence or absence of wellbore breakouts in the well.



In the vicinity of the proposed FORGE site, the vertical stress, S_v , at 3,500 m is 82 MPa based on integrated density logs recorded in the INEL-1 borehole. The water table measured in INEL-1 is at 91 m, indicating pore pressure in sub-hydrostatic at a value of 34 MPa at this depth. Wireline data and drilling experience from the INEL-1 borehole provide an estimate for the least horizontal principal stress, S_{hmin} of $58 \text{ MPa} \pm 2 \text{ MPa}$ at this depth. The lack of leak-off or mini-frac tests in any of the site boreholes currently limits our ability to accurately validate the least principal stress gradient.

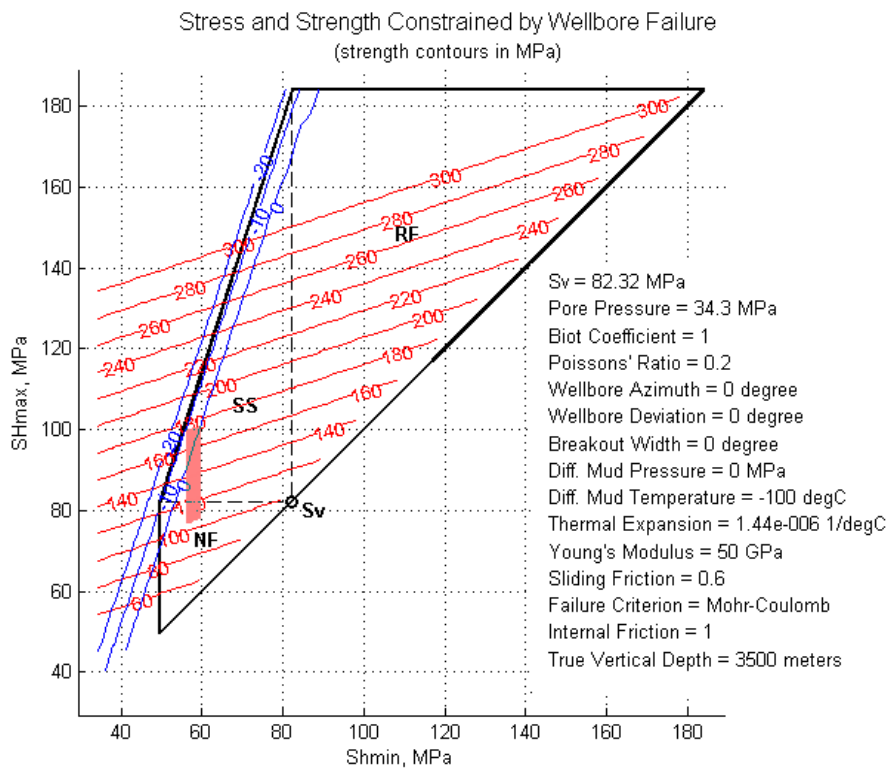
To constrain the magnitude of $S_{H\max}$, our approach will utilize the Baker Hughes GMI•SFIB™ modeling software along with the results of wellbore failure analyses to derive a stress state consistent with the occurrence or absence of drilling induced tensile fractures and wellbore breakouts in the reservoir zones. The modeling requires well-calibrated values for S_v , $S_{h\min}$, P_p , and UCS.

We provide an example of this approach, again based on preliminary modeling of data recorded circa 1990 in the INEL-1 borehole. The figure plots $S_{H\max}$ versus $S_{h\min}$ for a fixed value of S_v (at a depth of 3,500 m) to graphically illustrate all possible stress states as constrained by Coulomb frictional faulting theory (Moos and Zoback, 1990; see figure below). The perimeter of the figure polygon indicates the limiting values of $S_{h\min}$ and $S_{H\max}$ for which the state of stress is in equilibrium with the frictional strength of preexisting faults, a condition often observed in the earth (e.g., Zoback and Healy, 1992). For any point around the perimeter of the polygon, construction of a Mohr diagram would show that the circle would be exactly touching the Coulomb frictional failure line for an optimally oriented fault. We utilize a coefficient of friction of 0.6, consistent with the results from laboratory tests (Byerlee, 1978) conducted for many rock types encountered in the earth's crust, including geothermal reservoirs. The only allowable stress states are those that are either along the perimeter of the polygon or within its interior. This ensures that the in situ stresses never exceed a ratio of shear to effective normal stress that would initiate earthquakes on well-oriented faults.

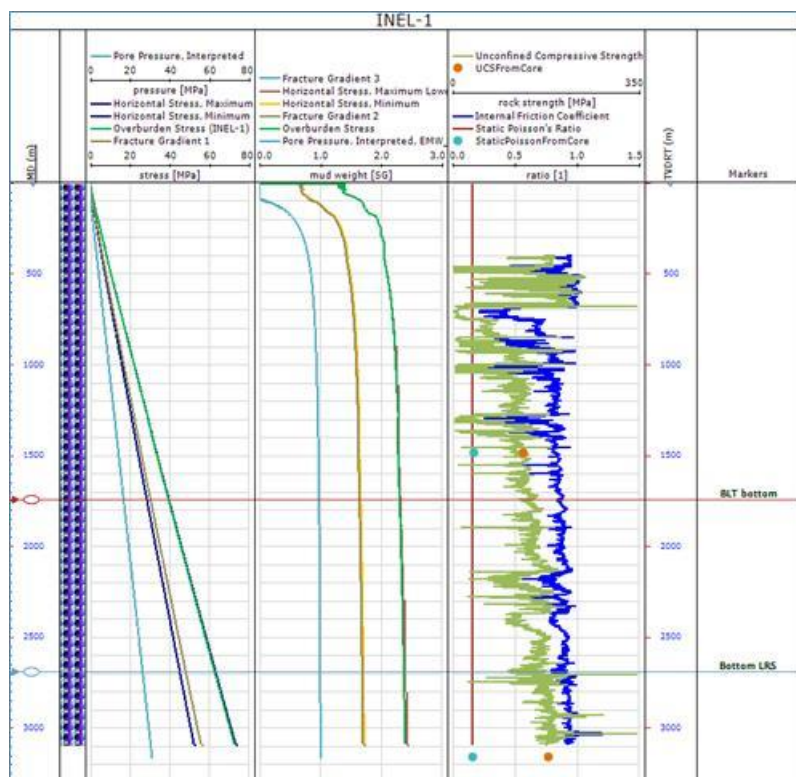
In order to apply more rigorous constraints on stress magnitudes using observations of wellbore failure, the plot also displays lines on the frictional constraint polygon that indicate the combination of values of $S_{h\min}$ and $S_{H\max}$ (for the given vertical stress, S_v) that are consistent with wellbore failures observed in image logs. Red lines represent the stresses consistent with observed breakouts (contoured for different rock strengths) and the blue line represents the minimum values of $S_{H\max}$ for the given $S_{h\min}$ that would be required to generate drilling-induced tensile wall fractures.

From the data currently available for this site, the maximum horizontal stress magnitude can only be constrained as transitional between normal faulting and strike slip faulting $S_v \geq S_{H\max} > S_{h\min}$ (red shaded area in the diagram below) with $S_{H\max}$ of $89 \text{ MPa} \pm 11 \text{ MPa}$ at 3,500 m. Once we have acquired contemporary wellbore image data, we will use this workflow to analyze data recorded in the newly drilled and existing wells to more precisely constrain stress magnitudes.

For the INEL-1 example, in situ stress orientation indicators such as wellbore breakouts and drilling-induced thermal fractures were not observed in the original 1990 image logging program precluding measurement of in situ stress orientation from these data. Although drilling-induced thermal fractures would be expected to occur at depth in the deeper INEL-1 borehole, it is likely that the relatively low-resolution circa 1990 acoustic televiewer tool could not resolve these fine-scale features. Our proposed science plan requires that more contemporary, higher-resolution wellbore image logging be undertaken at the FORGE site as part of the next logging program to help constrain both in situ stress orientation and magnitude.



INEL-1 stress state at 3,500 m constrained by P10–P90 range of rock strength values.

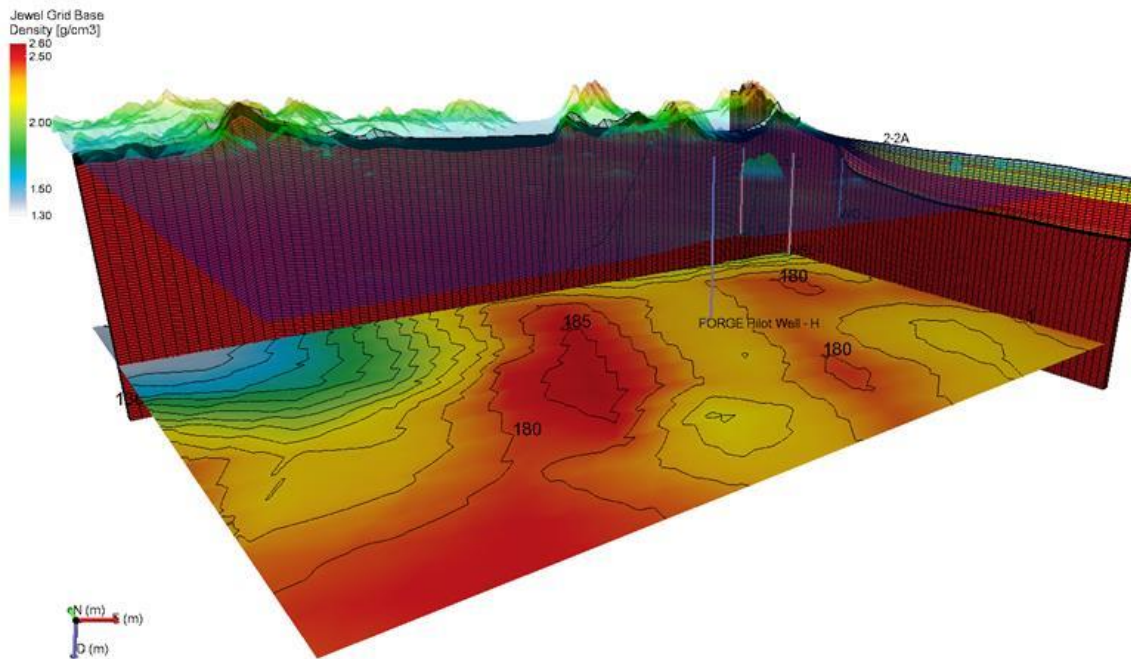


Preliminary geomechanical model for INEL-1 borehole based on limited geomechanical data.

Constructing the Three-Dimensional Geomechanical Model

The FORGE 3D geomechanical model will use a number of these 1D models and the geologic structural model (i.e., lithologies, horizons, and faults) to create a reservoir-scale geomechanical model as described in Holland et al. (2010). With moderate structural complexity and relatively homogenous stress fields within the reservoir, reservoir compartment, and overburden, the full workflow can be carried out within the 3D static model. For this methodology, a 3D grid is used and populated with the properties of the 1D geomechanical using geostatistical methods. The pore pressure and horizontal stresses are calculated using similar techniques used in the 1D models; only in this case, the calculations are not done along a well, but along the vertical, orthogonal pillars of the grid. The population of the grid with the primary properties is analogous to building a reservoir grid, although using a much higher resolution over the entire vertical column.

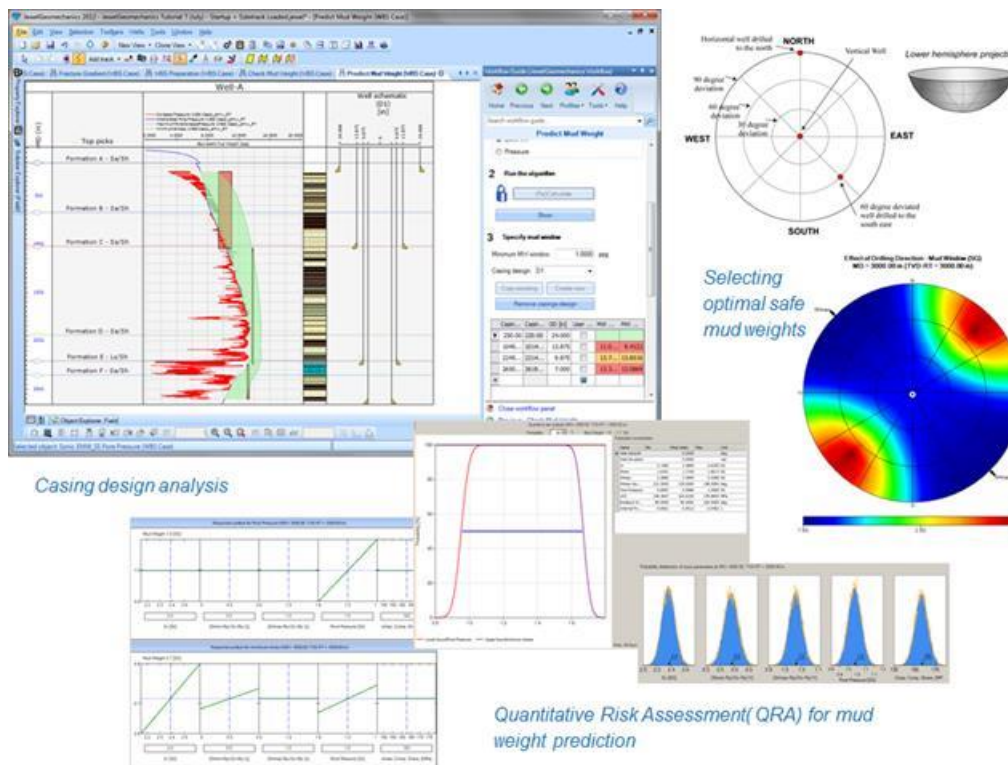
These reservoir-scale models make use of static equations to calculate the stress. 3D static modeling will incorporate density, static Young's modulus, and Poisson's ratio values derived from the 1D geomechanical modeling. Once upscaled, the 1D properties are mapped onto the structural grid. High-resolution 3D geomechanical models based on structural grids have a clear advantage over a 1D depth-stretched model by honoring structural and stratigraphic constraints. Layer thickness variations, erosional contacts, and lateral changes are accounted for. The image below shows density mapped to the preliminary structural grid generated for the proposed FORGE site. The contoured horizon is reservoirs temperature at 3,500-meter depth.



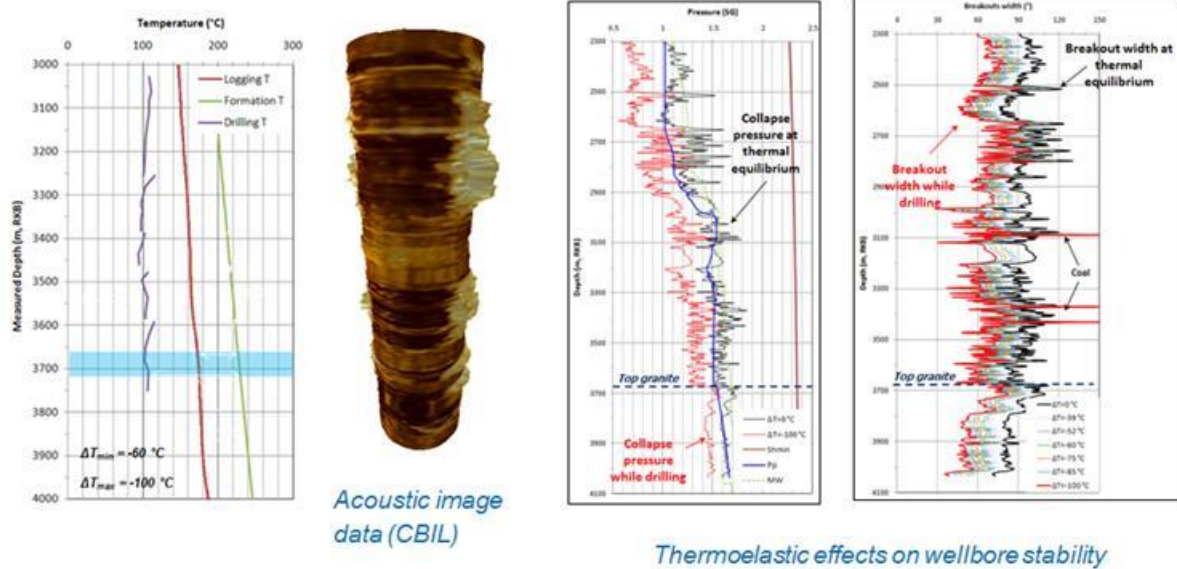
Under the assumption that one of the principal stress directions is vertical, the minimum and maximum horizontal stresses are calculated based on effective stress ratios derived from the 1D modeling. These ratios relate the effective horizontal stresses to the effective overburden and are related to the rock property and the stress field conditions. Populating these ratios allows estimating the horizontal stresses in respect to the local pore pressure, local overburden, and the local rock type. As with the stresses, the pore pressure cannot simply be extrapolated along the material layers. Different methods are possible depending on the pore pressure model and the available data (Ward et al., 1992; Bowers, 1994). With the stress model and the primary rock properties in place, other secondary properties like the fracture gradient are then—similar to the stresses—calculated from the grid properties at every cell location.

Application of the Geomechanical Model – Wellbore Stability and Hydraulic Fracture Design

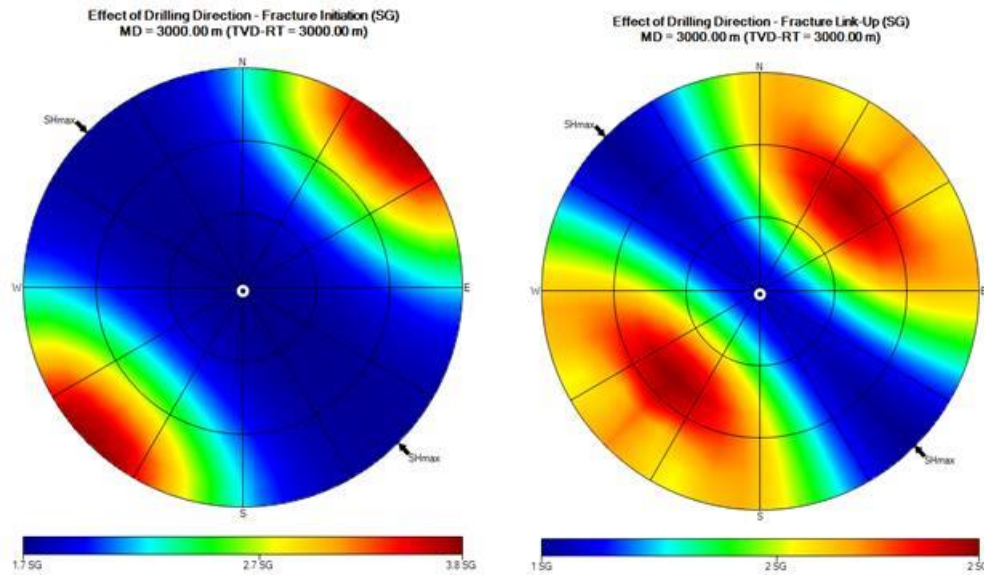
Knowledge of the in situ stresses allows optimization of drilling mud weights, the design of stable wellbore trajectories, assessment of the stability of uncased wells, and the evaluation of casing schemes. For example, based on the geomechanical model, it is straightforward to calculate the safe mud weight window for drilling wells for any well trajectory. We will use quantitative risk assessment to examine the influence of the uncertainties of the geomechanical model on the predicted required mud weight window, either at a certain depth or for a particular wellbore section. Quantitative risk assessment provides the probability distribution for drilling success where achievement of success is defined by engineering design. This information is extremely useful when prioritizing data collection or when determining what new data are required to increase the confidence in the wellbore stability analysis results.



In geothermal environments, it is critical to assess implications of thermoelastic stress changes while drilling. Cooling increases the tensile stresses (and decreases the compressive stresses) at the wellbore wall, affecting the development of wellbore breakout decreasing the collapse pressure required for compressional failure at the wellbore wall. As the hole warms up after drilling, the compressional stresses increase and so does the collapse pressure. Over time, the hole falls into thermal equilibrium and the collapse pressure increase requires higher mud weight to control excessive breakout development. The figure below shows the effects of this time-dependent stress evolution for the EGS Habanero field (data courtesy of Geodynamics, LTD).



Of equal importance to drilling is the application of the geomechanical model to well completion design, specifically the ability to hydraulically fracture the rock at the desired depth in the reservoir. With the geomechanical model, the optimal trajectory to initiate hydraulic fractures and for these fractures to link up and grow away from the wellbore can be determined.



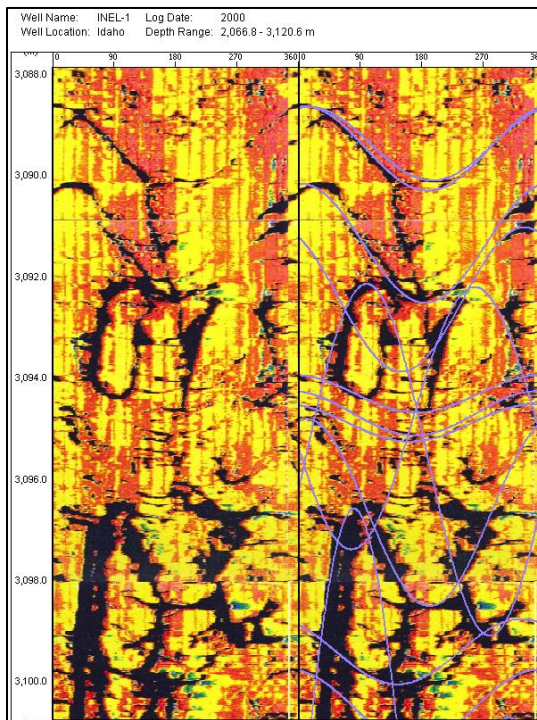
Optimal trajectories to initiate (left) and link-up (right) hydraulic fractures as a function of wellbore trajectory.

Natural Fracture Characterization and DFN Development

3D natural fracture characterization uses a variety of data to spatially map fracture occurrence, orientation, spacing, and intensity. The primary deterministic data for 3D fracture characterization are wellbore image data, microseismic data, well test or injectivity data, advanced acoustic logging data, and 3D seismic data. Wellbore imaging tools have dramatically improved in resolution and accuracy over the past 25 years; our proposed investigation of the ESRP will certainly benefit from these improvements. In

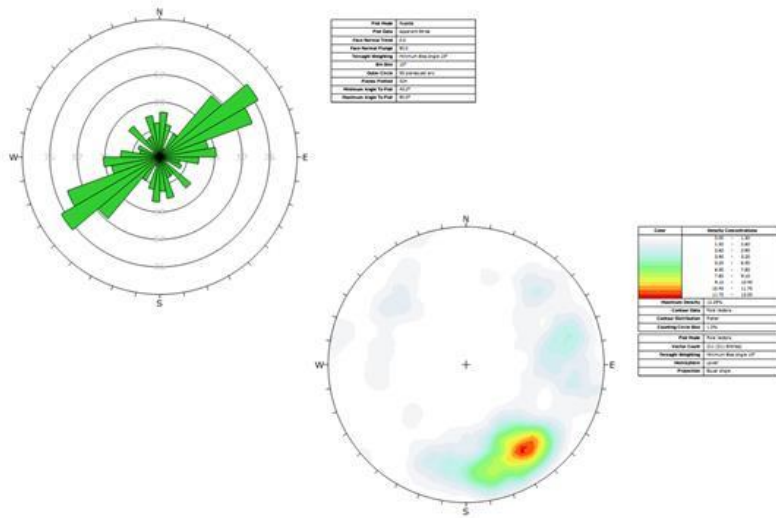
addition, there now exist wireline tools such as the deep shear wave imager that can image fractures and faults up to 30 m away from the wellbore, significantly enhancing knowledge of spatial fracture distribution. Further, high-resolution mineralogical logging (FLEX) can be used to discriminate sealed from permeable fractures in geothermal reservoirs. Contemporary 3D seismic data analysis methods include determination of fracture attributes based on seismic coherency which again would augment wellbore data with spatial fracture distribution.

In review of the limited data available for natural fracture analysis in this area, the Moos and Zoback (1990) study analyzed the depth distribution and orientation of fractures intersecting the three shallow wells and the deeper INEL-1 borehole. The image data provided a preliminary view of flow stratigraphy within the basalts, revealing a characteristic lithostratigraphy within each flow unit. At the base of each flow is a narrow zone of rubbly material, which grades into a massive interior cut by near-vertical fractures, possibly columnar joints. Near the top is a narrow zone a few meters thick of shallow-dipping fractures. This pattern of fractures detected in the basalts penetrated by the shallow wells is most likely due to thermal stresses generated during cooling. Individual flows identified on the bases of this characteristic pattern have thicknesses on the order of 26 m.

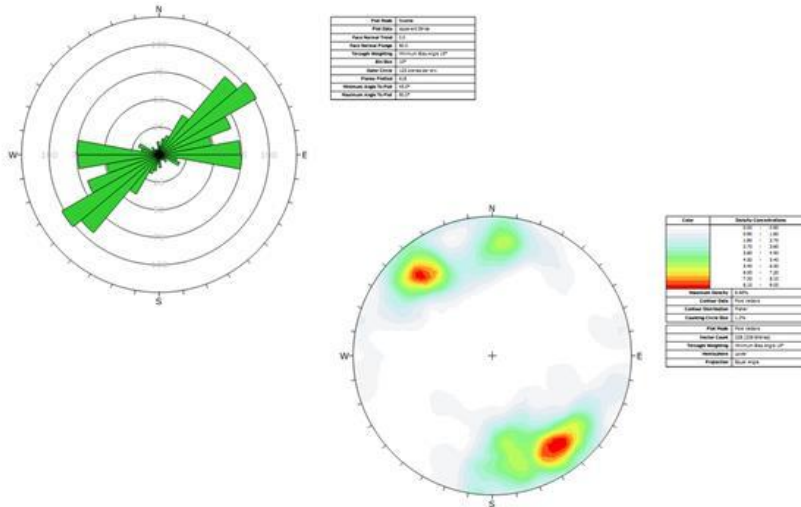


Typical circa 1990 wellbore image data recorded in Borehole INEL-1.

A limited sampling of the depth, orientations, apparent apertures, and lithologic setting of macroscopic fractures intersecting the INEL-1 borehole within the interval 2,067 to 3,121 m were available from the 1990 wellbore image analysis. In the welded tuffs, there are two main fracture populations, one striking northeast-southwest dipping steeply to the northwest and the other orientated roughly north-south dipping steeply to the west. In the lower rhyodacites, there are three dominant fracture populations (1) a northeast-southwest set steeply dipping both northwest and southeast; (2) an east-northeast set dipping to the south, and (3) a south-southeast set dipping to the north. The variability of fracture trends revealed by the image data analysis indicates there is a well-developed network of fractures that can provide a base reservoir volume for stimulation.



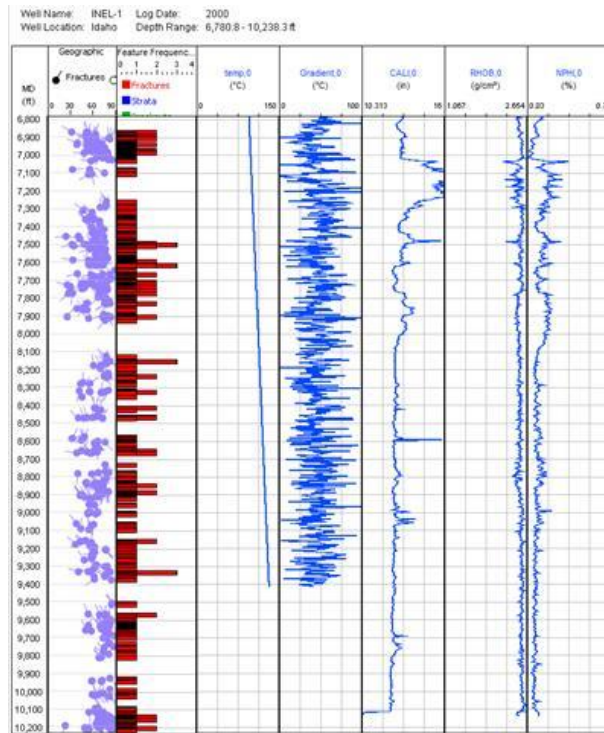
Fracture distribution derived from rhyolite interval, Borehole INEL-1.



Fracture distribution derived from rhyodacite interval, Borehole INEL-1.

Steeply dipping fractures are interpreted as relict structures related to caldera collapse, and thus were not formed in the present-day stress field. In addition to these fractures, numerous more shallow-dipping fractures were found. Fracture frequency does not systematically decrease with depth in the study interval. Although mechanisms acting to close fractures would be expected to reduce the number of open fractures with increasing depth, the data do not show this trend. Shallow-dipping fractures tend to cluster within specific depth intervals. This pattern is similar to that found in the extrusive basalts. The fracture distribution tends to be clustered with intermittent high fracture densities.

There appears to be a cyclic repetition of high-density fracturing followed by moderate to low fracture density throughout the logged interval of the INEL-1 borehole. These apparent cycles may be associated with repeated deposition of the volcanics and with the associated compositional changes indicating that the cyclic repetition of high density fracturing with intervening zones of moderate to low fracture density may be a consequence of processes occurring during deposition and cooling of the silicic volcanics. This detailed analysis of the fracture distribution will help to inform the stochastic DFN model.



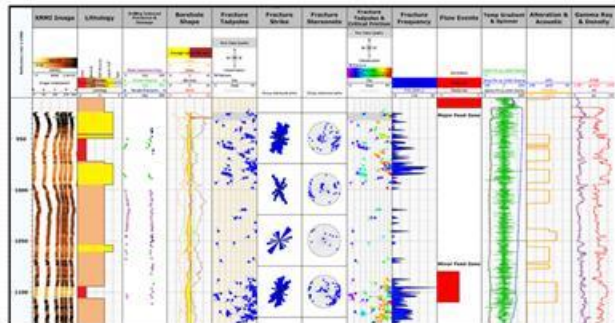
Fracture distribution (tadpole plot), fracture frequency per foot and associated well logs over the interval 6,780 to 10,200 m in Borehole INEL-1.

Three-Dimensional Fracture Characterization – Discrete Fracture Network Modeling

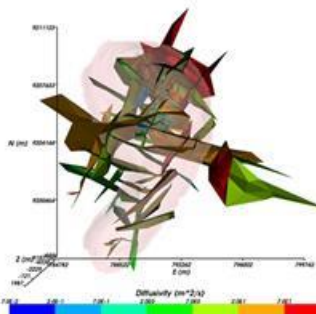
3D fracture characterization is focused on developing a conceptual model for natural fractures, interpreting a hydro-structural model for the site, and developing a 3D static DFN model. By static DFN, we mean a description of where fractures are expected to occur in 3D, their intensity (measured strictly as fracture area per unit volume), their statistical distributions of size (i.e., extent) and orientations. The DFN is built using the 3D geomechanics study, geological model, and various other well logs, microseismic and operational data, drilling logs, and interpretations. Then the model is calibrated on dynamic information based on monitoring data in response to injection, i.e., performing simulations of hydraulic stimulations of specific wells. These low-flow-rate injection tests are used to characterize the hydraulic properties of the fractures, their width, stiffness, and strength—properties that are often difficult to quantify, leading to the typically large uncertainties in predicted response to stimulation of fractured reservoirs. Model iterations include adjusting DFN parameters such as intensity, size, and aperture. Post-stimulation tracer tests of dipole injection between two wells can also be used to confirm the resulting DFN model parameterization and to screen stochastic realizations showing solute transport characteristics most similar to those observed.

An example of our DFN workflow applied to the Wayang Windu Geothermal Field in Indonesia is shown below (data courtesy of STAR Energy). Deterministic data are from wellbore data, image logs, production logs, lithology, and microseismic data recorded under stimulation provide fracture intensity, distribution, and hydraulic aperture. Stochastic DFN models are generated to find the optimal fit to the deterministic data. Integrating the results from our 3D geomechanical grid with the DFN fracture distribution, we can determine, using Coulomb failure analysis, the proximity to frictional failure of each fractures in the DFN. Mapping these fracture intersections to the reservoir volume provides a means to

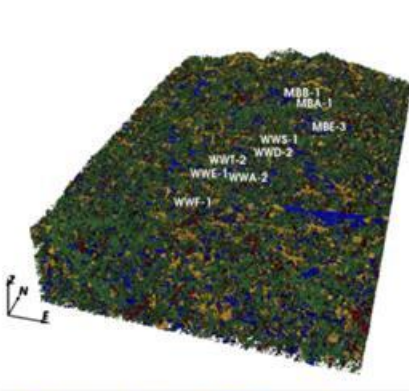
identify “geomechanical sweet spots,” zones with the highest density of stress sensitive fractures (Barton et al., 2013) for stimulation design.



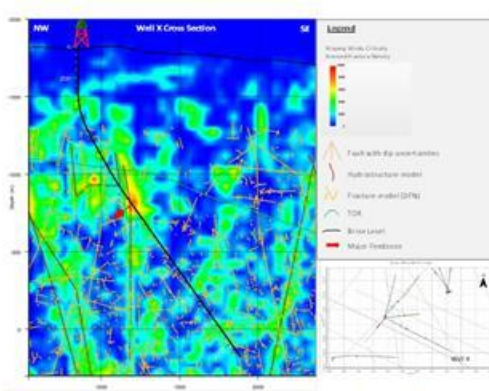
Fracture characterization from wellbore data



Hydro-structure characterization from MEQ and pumping data



Fracture trends of a DFN model

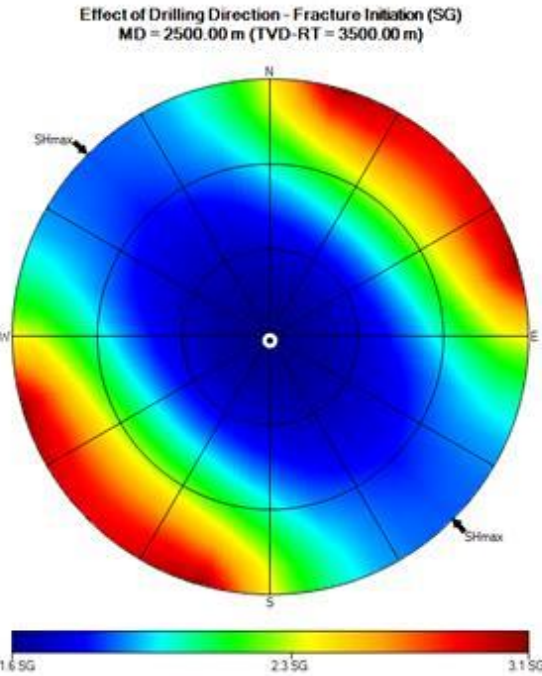


Density of stress sensitive fracture intersections

Implications of the in situ stress state and fracture network for stimulation of the SRP geothermal reservoir.

Effective production from EGS reservoirs requires stimulation of preexisting natural fractures, but it is also accompanied by hydraulic fracturing, which creates high-conductivity pathways back to the producing well. These are often held open after stimulation using proppants injected with the stimulation fluid. Because injection pressures exceed the least stress, the stimulated volume creation is likely here to be through a combination of shear stimulation and growth of new hydraulic fractures, enabling more efficient connections within the preexisting natural fracture system.

For the very limited 1D geomechanical data available for the INEL-1 borehole, we can evaluate the mud pressure at which a tensile fracture starts to form on the wellbore wall for a given tensile strength. The plot below represents this pressure as a function of wellbore trajectory; vertical wells are plotted in the center, and horizontal wells plot along the outside edge. The grid in the plot is aligned with the stress symmetry. Geographical north is at top of the plot and the two arrows pointing into the plot indicate the azimuth of the maximum horizontal stress based on out limited data. The plot shows wells highly deviated in the direction of $S_{h\min}$ require higher stimulation pressures than those drilled in the direction of $S_{H\max}$.

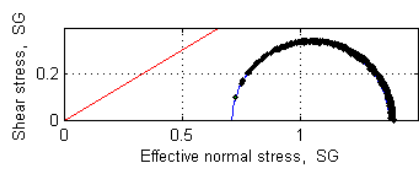
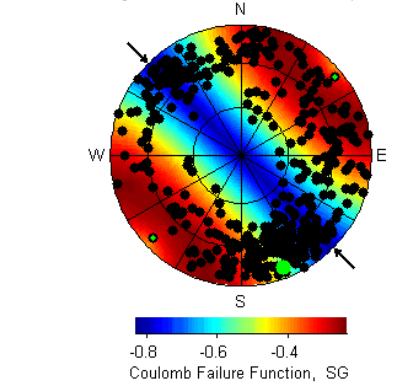


Similarly, we can use the INEL-1 1D geomechanical model to estimate the optimal trajectory to stimulate the preexisting natural fracture system. The approach we use for modeling the connected stimulated network is the observation, validated by numerous studies (e.g., N. Barton, 2007), that fracture conductivity is enhanced when fractures have slipped under a critical state in which the shear stress is sufficient to cause the fracture to fail in shear. Explicitly, we define this condition using a Coulomb failure criterion in which slip occurs when $\tau > \mu\sigma_n - S_0$ (τ is the shear stress acting on the fracture, μ is the coefficient of sliding friction, σ_n is the effective normal stress, and S_0 is the cohesion).

Under natural conditions (left plot), most fractures are nearly completely closed, as σ_n is always greater than zero in situ. Raising the reservoir pressure, as occurs during stimulation, decreases effective normal stress thereby causing an increase in the number of fractures that are critically stressed and thus can slip (right plot). Because fracture walls are rough, slip requires an increase in the crack width which enhances conductivity. As stimulation pressure continues to increase to values above the fracture gradient, Mode I (tensile) cracks will open, and, with continued pressure increases, the pre-stimulated shear fractures will also open. When the pressure drops after stimulation is complete, shear fractures remain open (they self-prop), but Mode I cracks will re-close unless proppant or other means are used to maintain their newly created aperture.

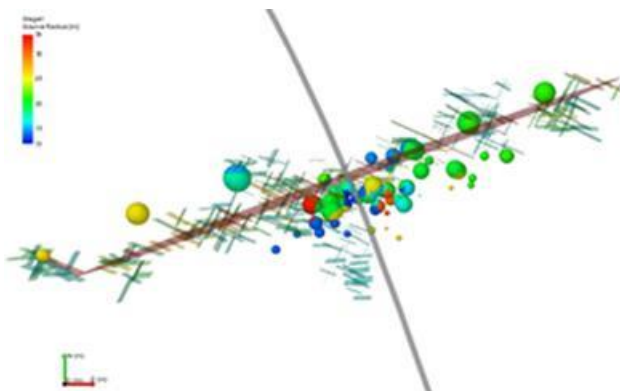
The stereoplots below show the measured fractures in Borehole INEL-1 before and after stimulation at 1 SG where white indicates critically stressed natural fractures. The lower Mohr circles show the pre- and post-stimulation effective stresses.

Effect of Fracture Orientation (poles on lower hemisphere) and Mohr Diagram at TVD = 2604 +/- 552 m (MD = 2604 m)



S _v = 2.37 SG	Coefficient of friction = 0.6
S _{Hmax} = 2.39 SG	Cohesion = 0 psi
S _{Hmin} = 1.70 SG	Depletion/Injection = 0
S _{Hmax} azimuth = 135 deg	Stress path parameter = 0
Pore pressure = 0.99 SG	S ₃ -normal frac limit = 10 deg
Biot's coefficient = 1.00	Best Well = 81/159 deg

The ARGOS software can predict pressure and flow at any point along the wellbore or within the developing fracture network and incorporates models for fracture aperture and slip. Under stimulation the hydrofrac provides the initial connection to the wellbore and natural fractures connect once slip occurs and nucleate microseismic activity. The ARGOS software can fully capture the exchange of frac fluids into the formation and preexisting fractures as a result of stimulation. Comparison to microseismic data provides validation, as shown below.



Natural fractures connected to a wellbore at an injection pressure of 25 MPa.

References

- Anders, M.H., Geissman, J.W., Piety, L.A., and Sullivan, J.T., 1989, Parabolic distribution of circumeastern Snake River Plain seismicity and latest Quaternary faulting: Migratory pattern and association with the Yellowstone hotspot: *Journal of Geophysical Research*, v. 94, no. B2, p. 1589–1621, doi: 10.1029/JB094iB02p01589.
- Bakshi, R., Halvaei, M. E., and Ghassemi, A., 2016, Geomechanical characterization of core from the proposed FORGE laboratory on the Eastern Snake River Plain, Idaho: *in Proceedings, 41st Workshop on Geothermal Reservoir Engineering* Stanford University, Stanford, California, SGP-TR-209.
- Barton, C. A., Moos, D., Hartley, D., Baxter, S., Foulquier, L., Holl, H., Hogarth, R., 2013, Geomechanically coupled simulation of flow in fractured reservoirs: *in Proceedings, 38th Workshop on Geothermal Reservoir Engineering* Stanford University, Stanford, California, SGP-TR-198.
- Bowers, G. L., 1995, Pore Pressure Estimation from Velocity Data: Accounting for Overpressure Mechanisms Besides Undercompaction: *SPE Drilling & Completion*.
- Byerlee, J. D., 1978, Friction of Rocks, *Pure and Applied Geophysics*, v. 116, p. 615–626, doi: 10.1007/BF00876528.
- Furlong, K., 1979, An analytic stress model applied to the Snake River Plain (northern Basin and Range Province, U.S.A.): *Tectonophysics*, v. 58, p. 11–15.
- Holland, M., Brudy, M., Van Der Zee, W., Perumalla, W., and Finkbeiner, T., 2010, Value of 3D Geomechanical Modeling in Field Development – A New Approach Using Geostatistics: *SPE/DGS Saudi Arabia Section Technical Symposium and Exhibition*, April 4–7, Al-Khobar, Saudi Arabia.
- Jaeger, J. C., and Cook, N.G.W., 1979, *Fundamentals of Rock Mechanics*, 3rd edition: London, Chapman and Hall, ISBN 0 412 22010.
- Kuntz, M.A., Spiker, E.C., Rubin, M., Champion, D.E., and Lefebvre, R.H., 1986, Radiocarbon studies of latest Pleistocene and Holocene lava flows of the Snake River Plain, Idaho: Data, Lessons, Interpretations: *Quaternary Research*, 25, 163-176.

- Moos, D., and Barton, C., 1990, In-Situ Stress and Natural Fracturing at the INEL Site, Idaho: DOE Report EGG-NPR-10631.
- Moos, D. and Zoback, M.D., 1990, Utilization of observations of well bore failure to constrain the orientation and magnitude of crustal stresses: Application to continental, Deep Sea Drilling Project, and Ocean Drilling Program Boreholes: *Journal of Geophysical Research*, v. 95, 9305–9325, doi: 10.1029/JB095iB06p09305.
- Morgan, W.J., 1972, Deep mantle convection plumes and plate motions: *American Association of Petroleum Geologists Bulletin*, v. 56, p. 203–213.
- Prestwich, S., and Bowman, J.A., 1980, Completion and Testing Report: INEL Geothermal Exploratory Well One (INEL-1): Department of Energy, Idaho Operations Office, IDO-10096, 53 p.
- Sparlin, M.A., and Braile, L.W., 1982, Crustal structure of the Eastern Snake River Plain determined from ray trace modeling of seismic refraction data: *Journal of Geophysical Research*, v. 87, no. B4, p. 2619–2633.
- Ward, C.D., Coghill, K., and Broussard, M.D., 1994, The Application of Petrophysical Data to Improved Pore and Fracture Pressure Determination in North Sea Graben HPHT Wells, SPE Annual Technical Conference and Exhibition, Society of Petroleum Engineers, September 25–28, New Orleans, Louisiana, SPE-28297-MS.
- Zoback, M.D., 2007, *Reservoir Geomechanics*: University Press, Cambridge.
- Zoback, M. D. and Healy, J. H., 1992, In Situ Stress Measurements to 3.5 km Depth in the Cajon Pass Scientific Research Borehole: Implications for the Mechanics of Crustal Faulting: *Journal of Geophysical Research*, v. 97, doi:10.1029/91JB02175.

Appendix H

Characterization

Appendix H Characterization

An extensive list of wireline petrophysical and wellbore image logs are planned for characterization of the Frontier Observatory for Research in Geothermal Energy site (Table H-1).

The Snake River Geothermal Consortium will record critical production logs, temperatures, flowmeter readings, and pressures to aid in mapping fluid inflow/outflow zones along the wellbore. Repeat temperature logs also reveal the systematic recovery to ambient temperatures of the cooled temperature profile that results from active circulation of cold surface fluid during drilling. Early production logs will be obtained prior to setting casing but prior to recovery of the well; later logs will be acquired after drilling fluid loss zones (perhaps coinciding to the primary flow zone) are behind casing.

Crossed-dipole acoustic logs can detect stress-induced anisotropy, and they help to identify and orient compliant and, therefore possibly conductive, fractures in the volcanic rocks. Acoustic logs are also invaluable for determining rock mechanical properties as a function of depth (i.e., rock strength, Poisson's ratio, Young's modulus, and friction angle) that can be calibrated with laboratory-derived values. We will also deploy the new deep shear wave-imaging tool capable of imaging near-well fractures that may or may not intersect the borehole as far as 18 m (60 ft) away from the well (Figure H-1). The lower image in Figure H-1 shows deep shear wave-imaging data looking out 15 m (50 ft) away from the borehole where reflectors are seen bounded by clear lithology structures. Primary strike direction of the reflector is N55E imaged from horizontal shear waves polarized in the same direction. These data provide extremely important natural fracture and fault information for wellbore completion design in geothermal reservoirs.

Table H-1. Summary of proposed well bore geophysical logging methods.

Logging Method	Method Name	Information Supplied	Comment	Priority
Density 350°F and 500°F	CDL/ZDL		Required to compute overburden stress by integration.	H
		Bulk density computed from electron density	Important for porosity.	
		Estimate of content of Fe, Ca, and Mg relative to Si, from PEF	Important constraint on gravity modeling.	
			PEF can help differentiate limestone, dolomite, and mafic-rich rocks (i.e., volcanics) from those with high quartz content, and help with clay mineralogy.	
Spectral natural gamma 350°F and 500°F	DSL		Total volume of clay and K-rich minerals.	H
		Separately measures the contributions of K, Th, and U to the total GR	U is mobile; high values could indicate paleo-flow zones.	
			Th and K help with clay mineralogy.	
			Recommended over standard GR.	
Neutron porosity 350°F and 500°F	CN		Important for porosity.	L
		Porosity from hydrogen content	Useful for clay volume if non-clay minerals are radioactive.	
		Volume of clays or hydrated alteration products	Not sensitive to porosity variation for porosities below a few percent.	
Resistivity 350°F and 500°F	HDIL	A measure of the volume of electrically conductive fluids (i.e., porosity)	Important constraint on magnetotelluric modeling.	M
		In low porosity rock, a measure of the volume of conductive minerals	Low resistivity indicates higher porosity, or the presence of electrically conductive minerals e.g., clays, oxides, or pyrite.	
			May provide estimate of total dissolved solids of fluids.	
Acoustic 350°F and 500°F	DAL	Compressional and shear elastic-wave velocities	Calibration for seismic or vertical seismic profile.	H
		With density, dynamic elastic moduli	Measure of degree of consolidation (stiffness).	
		Stoneley-wave reflections and attenuation	Can be used to compute rock strength to help constrain stress from observations of wellbore failure. Detecting compliant / conductive fractures Estimate of matrix permeability by Stoneley-wave inversion.	

Logging Method	Method Name	Information Supplied	Comment	Priority
Crossed dipole acoustic 350°F and 500°F	XMAC-F1		Useful for better seismic ties using transversely anisotropic velocities.	H
		Azimuthal shear-wave anisotropy	Sensitive to stress to determine orientations of maximum and minimum horizontal stresses.	
		Combined with Stoneley modeling, TI elastic moduli	Sensitive to intrinsic anisotropy (steep open fractures; dipping bedding).	
		Hole ellipticity and its orientation, from centralizer calipers	Independent information is required to differentiate stress-induced from intrinsic anisotropy.	
			Can substitute for 4-arm dipmeter to detect breakouts.	
			Processing is carried out offsite.	
Deep Shear Wave Image 350°F and 500°F	DSWI	All crossed dipole acoustic information	Detection of fracture and fault size and geometry between wells.	H
		Imaging structure (fractures and faults) in the volume surrounding the wellbore	Processing is carried out offsite.	
Electrical images 350°F	STAR		Important for structural analysis.	M
			Can be so sensitive to fine scale features it obscures useful information.	
		Centimeter-scale image of wall rock resistivity	Identifying drilling-induced tensile fractures for stress.	
		Fine-scale fractures, electrically resistive vs. conductive, NOT “open” vs. “closed”	In contrast to an acoustic image, does not provide complete wellbore coverage.	
		Subtle stratigraphy	Cannot be used alone to detect “permeable” fractures.	
			Pads can be damaged by high temperature.	
Acoustic images 350°F and 500°F	UXPL/GTI	Several cm-scale image of wellbore wall reflectivity	Excellent to identify mechanically “weak” fractures.	H
		Several cm-scale image of wellbore radius	Less resolution than electrical image logs.	
			Provides 100% wellbore coverage.	
			Excellent for breakout and tensile fracture analyses.	

Logging Method	Method Name	Information Supplied	Comment	Priority
Azimuthal resistivity 350°F	3DEX	Dip of electrically-anisotropic materials	Additional structural constraint.	L
		Resistivity perpendicular and parallel to bedding	May help separate structural from stress-induced elastic anisotropy.	
		Structural information available post-acquisition.		
Nuclear magnetic resonance 350°F	MREX	Porosity	Pad-type tools are sensitive to wellbore roughness.	L
		Estimate of permeability	Permeability estimate requires calibration.	
			May have temperature limitations- rated to standard 350°F.	
Wireline straddle packers 350°F	RCX-SP	Pore pressure	The stress and pore pressure data can be very important to supplement or replace an extended leak-off test.	H
		Least Principal stress from micro-fracturing tests	May not be available from all service providers Have severe temperature constraints and pressure limitations Only SLB and BHI offer - 120k (for one set of packers), 35k for element changes, 20% surcharge for high strength mandrel.	
Pulsed neutron 350°F and 500°F	Rockview	Mass fraction of individual elements	Detailed mineralogy.	L
			Carbon content.	
			Precise depth delineation of lithologic contacts.	
Caliper 350°F, 2 axis at 500°F	WGI	Hole size, using one or more independently articulated arms	Detects weak fractures and faults that cause wellbore enlargements.	H
			Single-arm caliper provides information to correct other logs for hole size.	
			Multi-arm caliper (6-arm) allows determination of hole shape; if oriented can be used to detect and orient wellbore breakouts for stress determination.	
High Temperature 350°F, 2 axis at 500F	HTHP	High-Temperature Logging over 350F	Tools that qualify need additional preparation.	H
			RCX - SP HT surcharge applies above 300°F.	
			Maintenance costs are escalated after 350°F	
			Availability of these special tools results in higher transport costs.	

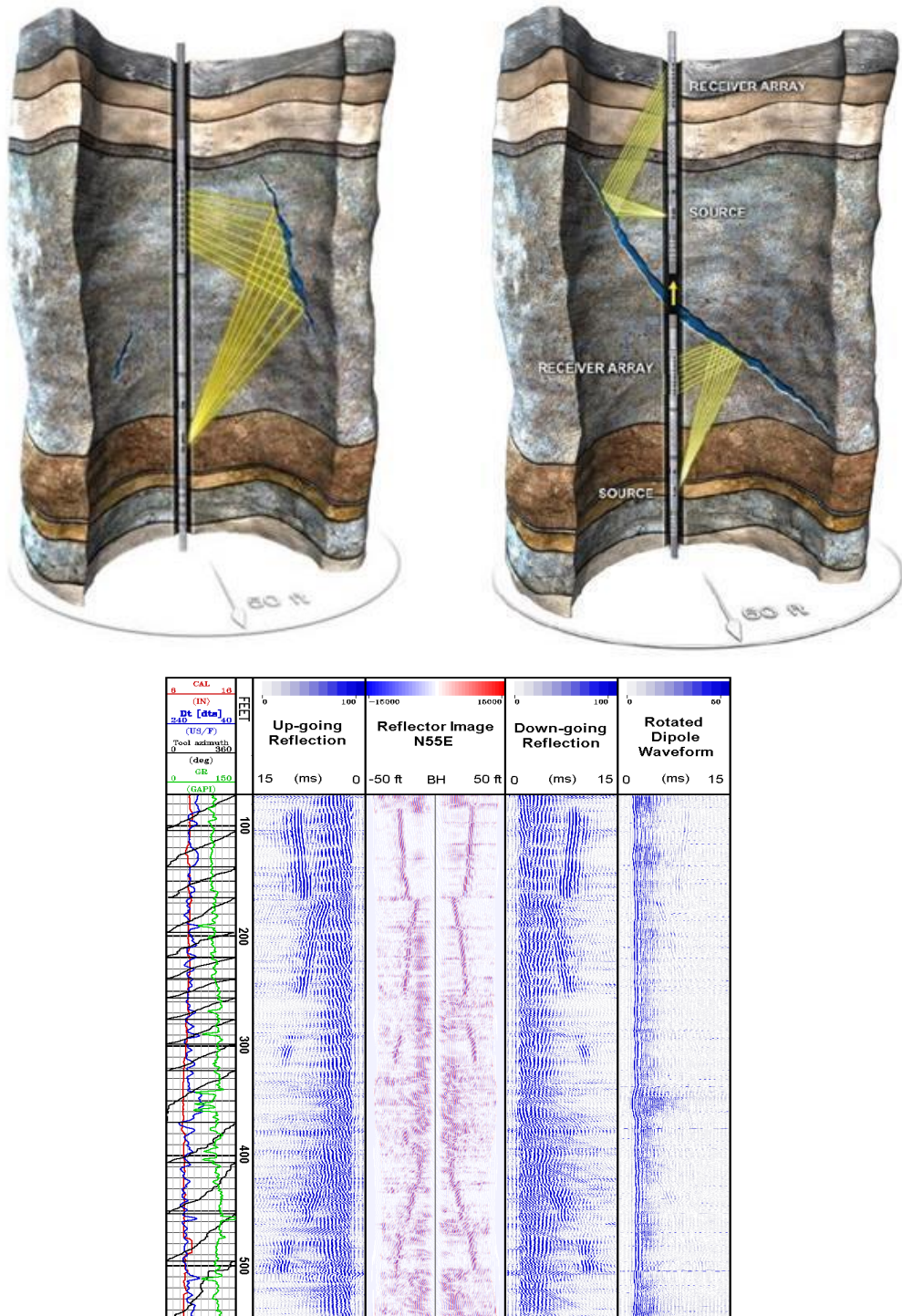


Figure H-1. Near-well fractures that may or may not intersect the borehole as far as 18 m (60 ft) away from the wellbore (upper images) and deep shear wave imaging data looking out 15 m (50 ft) away from the borehole where s are seen bounded by clear lithology structures (lower image).

